Optimal perturbations in swept leading edge boundary layers.

Alan Guegan

École polytechnique
Laboratoire d'hydrodynamique (LadHyX)

Thèse présentée pour obtenir le grade de

DOCTEUR DE L'ÉCOLE POLYTECHNIQUE

spécialité : mécanique

par

Alan Guégan

Optimal perturbations in swept leading-edge boundary layers*

---

*Perturbations optimales dans la couche limite de bord d'attaque d'une aile en flèche

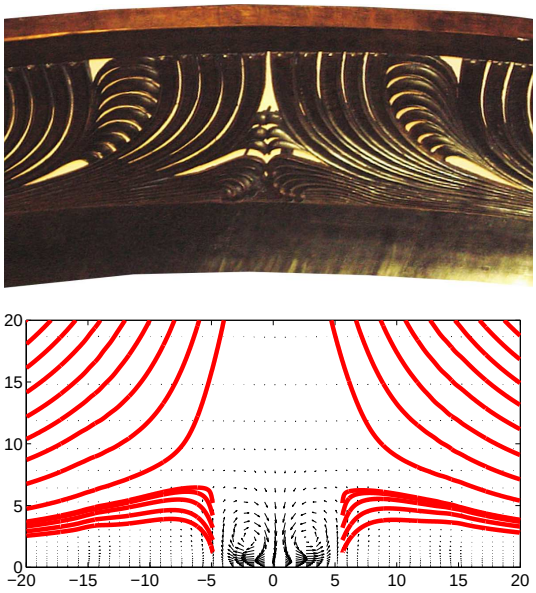

soutenue le 4 octobre 2007 devant le jury composé de :

Patricia Cathalifaud	examinatrice
Uwe Ehrenstein	rapporteur
Dan Henningson	rapporteur
Patrick Huerre	directeur de thèse
Grégoire Casalis	président
Peter Schmid	directeur de thèse
Denis Sipp	examinateur

Thèse de doctorat

présentée par

Alan Guégan

Optimal perturbations in swept leading-edge boundary layers*

---

*Perturbations optimales dans la couche limite de bord d'attaque d'une aile en flèche

Illustrations on the front page:

Top : cupola of the Théâtre des Champs-Elysées (detail), Perret brothers, 1913

Bottom : in red, streamlines of the total flow (basic swept Hiemenz flow plus perturbation) in a two-dimensional $x, y-$plane at $z = z_{max}$ for an optimal spatial perturbation when $z_{max} = 200$, $Re = 550$, $\omega = 0$ and $L = 3$. The streamlines have been computed from the same simulation as in Figure 4.9 and Figure 4.10. Arrows represent the two-dimensional perturbation $u, v-$velocity field.

Remerciements

Un peu par hasard, j'ai découvert la randonnée à la même époque que la recherche académique. Sur les chemins de montagne, j'ai appris à marcher de longues heures, au besoin en forçant chaque pas, et presque toujours sans voir le but final, le refuge caché derrière un col ou la tache d'ombre où bivouaquer. C'est finalement assez facile, la randonnée.

Il existerait un proverbe peul selon lequel, *"si tu veux aller vite, vas-y seul, mais si tu veux aller loin, vas-y accompagné"*. Une thèse n'étant pas un exercice de vitesse, je voudrais remercier toutes celles et ceux qui m'ont accompagné sur ce chemin : mes directeurs de thèse, à qui je dois d'avoir soutenu une thèse qualifiée de "remarquable" par le jury; ce même jury constitué de Grégoire Casalis, Patricia Cathalifaud, Uwe Ehrenstein, Dan Henningson et Denis Sipp ; les collègues qui m'ont soutenu, et je pense en particulier à Emmanuel, Sabine, Pascal, Jean-Marc, Carlo, Paul, Paul, François. J'ai trouvé du soutien également auprès de Thérèse et Daniel, et auprès des doctorants et stagiaires qui m'ont précédé et qui me suivent, Ramiro, Maher, Axel, Christoph, Maria-Luisa, Grégory, Benoist, Angel, la Québec Connexion avec Maxime, Mathieu, Fédérick, ainsi que Emilie et Jo qui nous ont rejoints en post doc. Je décerne une mention spéciale à ceux qui ont eu la chance de partager mon bureau et mes états d'me, Charlotte, Cécile, Cédric, Rémi.

Parmi les personnes que j'ai rencontrées au cours de cette thèse, quelques-unes sont devenus des amis. J'envoie une pensée à Rafael, qui navigue entre Seattle en Vancouver, ainsi qu'à Charles qui doit assister en ce moment à des soutenances de stage palpitantes quelque part sur le campus de l'X.

Eloignons-nous encore un peu du labo, et nous trouverons un panorama un peu plus varié : Baptiste, Marielle et Benjamin, Arnaud, Bartek, Soizic, Maria et le grand Fred. Quelques-uns ont cru bon de faire une thèse eux aussi : je félicite les docteurs Cyrille, Matthieu, Elli et les futur diplômés Emilie et Philippe. Loïc ne s'embarrasse pas d'équations, et préfère mettre son énergie dans la rando. A chacun son chemin !

La famille a compté énormément ces dernières années. N'y puis-je pas citer Sylvain, Céline et les petits Manon et Paol ? Je remercie Hetty et Anna qui ont pu assister à la soutenance, Erwann et Murielle à qui je souhaite plein de bonheur. Maman, Papa, mes deux soeurs Marie et Jeanne m'ont beaucoup aidé dans les moments de doute et de remise en cause. Je les remercie de tout coeur !

Ingrid, tu m'as été d'un soutien sans faille et d'un optimisme éclatant. Avec toi à mes côtés je n'ai jamais douté de l'issue de ma thèse !

Ma dernière mention très honorable, avec félicitations, va à Jérôme et Lutz, deux amis que j'admire et qui me sont très chers. Vivement que l'on puisse fêter ça ensemble, à Paris ou à l'autre bout du monde !

Alan,

le 17 octobre 2007

Cette thèse a été financée principalement par une bourse DGA de trois ans; la dernière année a été financée grâce à un contrat de recherche signé avec Airbus.

Contents

Chapter 1

Introduction

1.1 A general introduction to viscous flow and boundary-layer instabilities

1.1.1 Flying in a viscous fluid

Rockets and zeppelins set aside (Figure 1.1), flying is achieved in the vast majority of cases by making air flow at considerable speed around a carefully designed solid obstacle - a wing or a propeller for instance. A vertical force strong enough to overcome gravity is generated owing to a property of air that in many other circumstances is negligible: viscosity.

However negligibly small viscous forces may be in the outer flow, they cause the fluid to adhere to the surface of a solid obstacle. On an airplane, for instance, air molecules actually stick to the wing surface, although the aircraft may move with respect to the ambient air at an average of a thousand kilometers per hour in cruising flight.

Ludwig Prandtl (1875-1953) was the first to propose a satisfactory theoretical approach to investigate viscous flow around solid obstacles. Prandtl assumed that the surface is coated with a thin layer of fluid called the *boundary layer* (Figure 1.2). In the immediate vicinity of an obstacle, within the boundary layer thickness δ, viscous effects force the flow velocity to zero at the solid boundary. Further away, where fluid velocity is high, the flow is governed by inertial effects and viscosity is negligible.

The boundary layer thickness δ typically depends on the outer flow velocity U_∞, the kinematic viscosity ν, and the geometry of the obstacle. For instance, in the

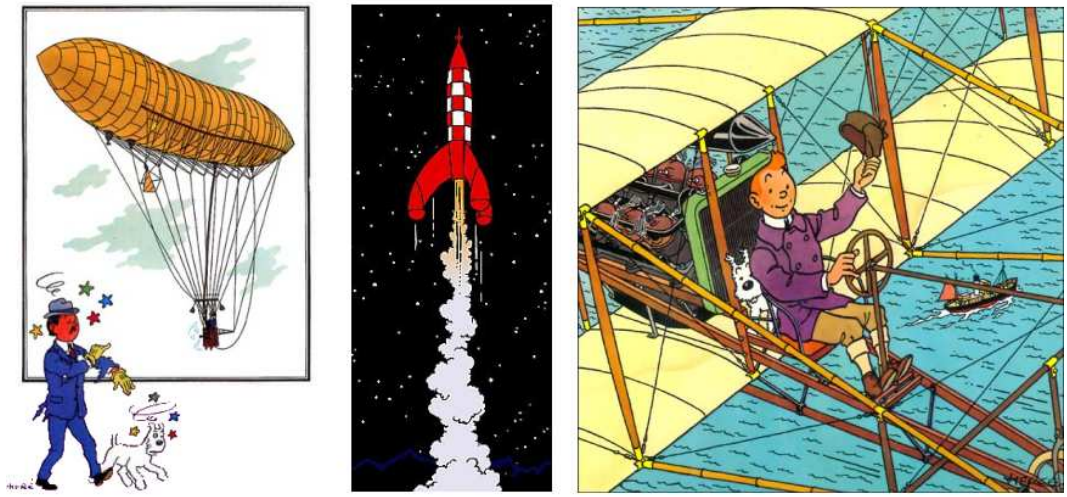

Figure 1.1: Three man-made flying machines. Zeppelins are less dense than air; they float according to Archimedes' principle. Rockets throw massive quantities of matter downward at high speed; Newton's action-reaction law helps them escape gravity. Planes take advantage of air viscosity to fly.

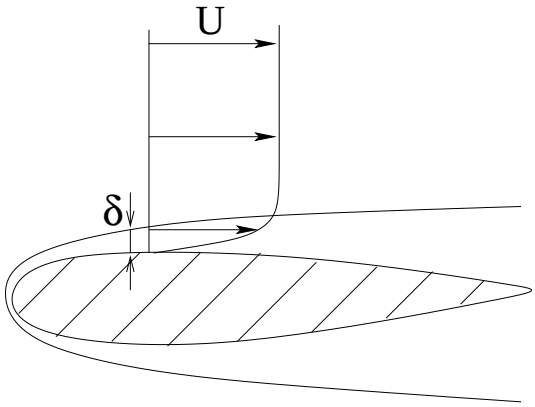

Figure 1.2: Sketch of the boundary layer around a wing. The boundary-layer thickness δ decreases as the outer velocity U increases.

case of a flat plate (Blasius (1908)), δ develops with distance L from the leading edge as the inverse of the square root of the Reynolds number:

$$\delta \sim Re_L^{-1/2} \ , \tag{1.1}$$

with the Reynolds number being

$$Re_L = \frac{U_\infty L}{\nu} \ . \tag{1.2}$$

One meter downstream of the leading edge of a flat plate, the boundary layer formed by an air stream at $U = 1\ ms^{-1}$ is less than one millimeter thick; within this distance from the plate, the flow velocity drops from $U = 1\ ms^{-1}$ in the outer stream to zero at the surface. The wall-normal velocity gradient $\frac{\partial \mathbf{U}}{\partial \mathbf{n}}$ is large and shear forces are intense in the vicinity of solid surfaces.

The velocity gradient within the boundary layer also induces cross-stream vorticity $\mathbf{\Omega} = \mathbf{curl}\ U$. Airfoils are specifically designed so that the integrated vorticity around their profile is non-zero. The lift generated by an airfoil may be related to its net vorticity production through arguments from potential flow theory.

A "perfect", i.e. non-viscous fluid would not adhere to solid surfaces, but rather would slip on them without forming a boundary layer. Unlike the viscous setting, vorticity is conserved in a perfect fluid. As a consequence, regardless of the obstacle shape, a perfect fluid cannot generate lift – as puzzling as it may seem, planes only fly because air is viscous.

1.1.2 On the stability of shear flows

Maximum efficiency, in the sense of a maximum lift-to-drag ratio, is achieved when the flow around the wing is laminar. As the flow becomes turbulent, more kinetic energy is dissipated and drag increases.

Shear flows such as boundary layer flows are notoriously unstable to disturbances (see, e.g. Schmid and Henningson (2001)). This means that infinitesimal perturbations originating from outside or inside the boundary layer may be amplified by the ambient shear. Large perturbations may disrupt laminar flows and lead to turbulent states. Figure 1.3 shows transition to turbulence on a flat plate.

Transition to turbulence has still not met a satisfactory, generally-accepted explanation. One hypothesis is that small disturbances are linearly amplified up to energy levels at which non-linear effects set in and drive the flow to turbulence.

Figure 1.3: Boundary-layer transition on the surface of a flat plate, seen from the top. Flow is from left to right and dye visalization shows the transition from laminar (on the left) to turbulent flow (on the right). (Photograph courtesy of ONERA)

Linear energy amplification occurs either because the perturbations take the shape of linearly unstable modes or because of non-normal effects (see, e.g. Schmid and Henningson (2001)). In the latter case, non-normal eigenmodes interact in such a way that energy is transiently amplified, even if the flow is linearly stable; transition to turbulence is then qualified as *by-pass transition*.

The energy amplification of a given disturbance may be readily evaluated by means of numerical simulations: once its temporal evolution has been computed, initial and final measures of the kinetic energy are compared. Optimization theory provides strategies to identify the optimal perutrbation of maximum energy growth. These linear disturbances the energy of which is the most amplified over finite times or distances are called *optimal perturbations*; they are suspected to play a major role in the transition process.

1.1.3 Controlling shear flows

In recent years considerable effort has been spent in controlling the growth of boundary-layer disturbances. Significant progress in this field has recently been achieved by the group of Dan Henningson at KTH, Stockholm in 2006. Fransson et al. (2006) excited optimally-growing streaks in a flat-plate experiment by placing small cylinders spaced at the optimal spanwise wavelength inside the boundary-layer. Optimal streaks quickly reach a non-linearly saturated state; Fransson et al. (2006) showed theoretically that, contrary to the unperturbed boundary layer, amplitude-saturated streaks are stable to linear disturbances. In agreement with theoretical predictions, the streaky boundary layer in the experiment remained laminar across the entire plate, whereas in the absence of streak generators, turbulence set in at a

short distance behind the leading edge.

A number of other strategies to prevent turbulent transition on a wing surface have been proposed. Novel numerical techniques and increased computing performance have made it possible to investigate wall-normal blowing and suction control strategies. In such configurations, blowing and suction devices as well as flow sensors are assumed to be distributed over the wing surface. Suitable synchronization of the blowing/suction pattern with the measured flow structures has been numerically demonstrated to relaminarize a turbulent channel flow (Bewley et al. (2001)).

Numerical experiments allow much more precise flow control than real-life laboratory experiments. A number of issues still have to be resolved before closed-loop real-time wall blowing and suction strategies may be implemented in an experiment. These strategies have theoretically been proven to be efficient, but despite rapid innovation in the design of experimental devices, their direct application to flows of industrial interest is still out of reach. For a numerical investigation of active control, wall-normal blowing and suction remains a convenient model.

1.2 Disturbances and control of the attachment-line boundary layer

1.2.1 Flow configuration at the leading-edge of swept wings

To facilitate visualization of the flow configuration, a swept wing has been sketched in Figure 1.4. The three directions of reference are the spanwise $z-$direction parallel to the attachment-line, the chordwise $x-$, and the wall-normal $y-$direction. The attachment-line boundary layer is characterized by a single flow parameter, the Reynolds number

$$Re = \frac{W_\infty \delta}{\nu} \ . \tag{1.3}$$

The free stream sweep velocity W_∞ is proportional to the angle of attack; the length scale δ is based on the strain rate of the irrotational outer flow $S = (dU/dx)_{y\to\infty}$ and the kinematic viscosity ν according to:

$$\delta = (\nu/S)^{\frac{1}{2}} \ . \tag{1.4}$$

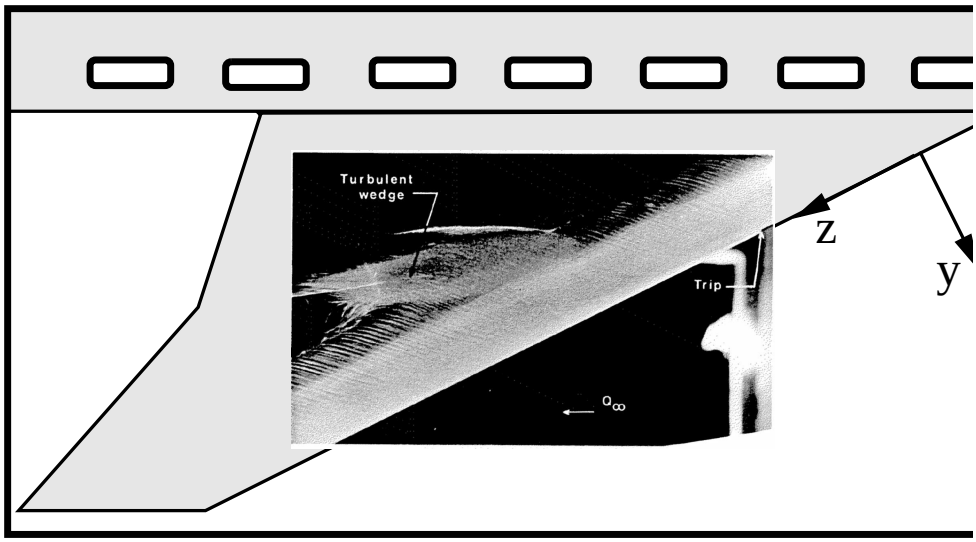

Figure 1.4: Sketch of a swept wing with the spanwise $z-$, the wall-normal $y-$ and the chordwise $x-$direction. Crossflow vortices appear as black lines on the inserted photograph (see Poll (1978)). Turbulent contamination of the upper wing surface is triggered by disturbing the attachment-line boundary layer with a trip wire.

1.2.2 Previous experimental and theoretical results

Most of the investigations of transient growth and boundary-layer control have focused on the upper surface or airfoils (Andersson et al. (1999), Corbett and Bottaro (2001b), Pralits et al. (2002), etc.). By contrast, the knowledge of transient phenomena in the *leading-edge* boundary layer is quite sparse. The inherently three-dimensional nature of the flow makes it difficult to approach theoretically, and even numerically, while a comprehensive experimental database is lacking.

Some thirty years ago, Poll's assessment of leading-edge boundary layer research was not very different from where we stand today (see Poll (1978)). Interest in the swept attachment line was first prompted when Gray observed that two-dimensional criteria failed to predict transition very close to the leading edge of swept wings (see Gray (1952a), Gray (1952b)). Theoretical and experimental investigations suggested that cross-flow instability was responsible for early transition on swept wings.

In 1963 Handley Page Ltd and Northrop Norair attempted to design fully laminar swept wings. Although suction devices had been placed close to the leading edge in order to prevent crossflow-induced transition, laminar flow could not be maintained. Turbulence originating at the wing-body junction was swept along the leading edge

and produced a turbulent attachment-line boundary layer that contaminated the upper wing surface. Attachment-line contamination artificially triggered by placing a trip wire onto the leading edge of a swept wing can be seen in the photograph in Figure 1.4. Pfenninger and Bacon (1969) as well as Gaster (1967) investigated this phenomenon, but, as Poll (1978) remarks with a touch of bitterness, *"despite the fact that the contamination mechanism was of obvious practical significance the work ceased when the respective laminar flow projects were cancelled and the physics of the transition process was never completely investigated."*

Today, contamination of the attachment-line boundary layer is still not fully understood; still, significant theoretical progress has been made since 1978. The most important stability result is due to Hall et al. (1984), who found the incompressible leading-edge boundary layer to be linearly unstable above a critical sweep angle, corresponding to a Reynolds number $Re = 583.1$. The least stable eigenmode takes the shape of two-dimensional Görtler-Hämmerlin perturbations, which has been found to hold true also in compressible attachment-line boundary layers (see Robitaillié-Montané (2005)). Furthermore, Obrist and Schmid (2003b) have shown, in the context of Hermite polynomial decompositions, that the leading-edge boundary layer exhibits transient growth phenomena.

Pfenninger and Bacon (1969) demonstrated experimentally that attachment-line boundary layers support spanwise-travelling, two-dimensional disturbances when the leading edge is smooth. When a sufficiently thick trip wire is placed perpendicular to the attachment-line, Poll (1979) found the boundary-layer to become turbulent. In the presence of strong free-stream turbulence, spanwise-travelling disturbances are not observed; instead, stationary cross-flow vortices develop across the upper wing surface, at a moderate distance from the attachment-line.

Indeed, the community today seems to be in a situation similar to the one faced by Poll in 1978, where the knowledge of (transient) stability properties of the flow on the wing surface is significantly more advanced than the knowledge of (transient) stability properties of the attachment-line boundary layer. The goal of the present PhD thesis is to complement the knowledge of the flow along swept leading edges by characterizing transient growth phenomena in this configuration.

1.2.3 Control strategies

The turbulent boundary-layer at the surface of the fuselage may enter the attachment-line boundary-layer at the junction with the wing. To prevent turbulence from spreading along the entire leading edge it is necessary to isolate the attachment-line boundary layer from the fuselage's own boundary layer. Gaster (1965) suggested to

place a protuberance along the leading edge in the vicinity of the wing-body junction. When this "Gaster bump" is suitably designed, a stagnation point appears on the protuberance, and a new, turbulence-free attachment-line boundary layer forms downstream of the bump. Reneaux (2004) reports that experiments carried out at ONERA showed that such devices delayed contamination up to $Re = 400$ instead of $Re = 250$ for the smooth leading-edge.

Open-loop control of the attachment-line boundary layer has also been tested by applying suction at the leading-edge. Flight tests were carried out in 1998 on the vertical fin of an A-320 equipped with laser-drilled panels, connected to suction chambers. The gain in total aircraft drag reduction was on the order of 1% as reported by Joslin (1998) and Reneaux (2004).

More complex time-varying blowing and suction strategies have never been tested on the attachment-line boundary layer. Although maintenance costs are still prohibitive for active devices to be implemented on commercial airplanes, assessing active control in numerical experiments could provide an interesting starting point for the future development of swept leading-edge flow control.

1.3 Outline

In chapter 2 the concepts of optimal energy growth and optimal control are applied in the context of Görtler-Hämmerlin perturbations. A gradient-based optimization algorithm is derived directly from the reduced set of equations for the chordwise $u-$ and the wall-normal $v-$velocity components. The derivation of the adjoint problem is described in detail and an exhaustive investigation of the control parameters that appear in the objective functional, made possible in the context of this one-dimensional problem, is provided. The present study is based on and complements previously published work: Corbett and Bottaro (2001a) derived adjoint equations from the reduced Orr-Sommerfeld system of equations in a similar fashion, but without stating the objective functional gradients. Corbett and Bottaro (2001b), Bewley and Liu (1998) among others, studied the influence of the objective functional control parameters on the control efficiency, but an exhaustive parameter study was lacking to unambiguously determine the optimal set of parameters.

The optimal initial disturbances and the optimal wall-normal blowing and suction strategy are computed under the Görtler-Hämmerlin assumption. A new physical mechanism is described that is responsible for large energy growth at low spanwise wavenumbers. Optimal control is shown to efficiently damp temporal Görtler-Hämmerlin disturbances. Chapter 2 has been published in the Journal of Fluid Mechanics (see Guégan et al. (2006)).

In chapter 3 the restrictive Görtler-Hämmerlin hypothesis is relaxed in order to find optimal temporal perturbations of arbitrary shape. A direct numerical simulation algorithm similar to that of Obrist (2000) is described. A fringe region technique has been introduced in order to allow spectral discretization of non-periodic domains, and caveats of this boundary treatment in the context of adjoint-based optimization are discussed. The optimization algorithm that was used in chapter 2 is now adapted to compute the optimal temporal growth of arbitrary spanwise-periodic perturbations. Results are compared with the study of Hoepffner et al. (2005), who computed optimal temporal perturbations in the context of a streaky boundary layer. Discrepancies and similarities between Görtler-Hämmerlin perturbations and temporal disturbances of arbitrary shape are discussed in light of Guégan et al. (2006). Chapter 4 has been published in the Journal of Fluid Mechanics (see Guégan et al. (2007)).

Chapter 4 focuses on optimal spatial disturbances, as opposed to the temporal analyses of the previous chapters. The spatial framework provides a more accurate description of the spanwise amplification of disturbances originating from the junction of the wing with the fuselage, as compared to the temporal framework investigated in chapter 2 and chapter 3. A model problem based on the Ginzburg-Landau equation is devised in order to validate the parabolization assumption in the context of the search for optimal disturbances. Then, parabolized spatial perturbation equations for swept Hiemenz flow are derived and the adjoint problem is formulated. Numerical techniques are validated by reproducing the results of Andersson et al. (1999), Luchini (2000) and Tumin and Reshotko (2001). Optimal spatial disturbances are analyzed in section 4.5 and results are compared with the papers of Andersson et al. (1999) and Luchini (2000).

Chapter 5 summarizes the key findings and conclusions to be drawn from this study and provides perspectives for future work.

Chapter 2

Optimal perturbations and optimal control in the Görtler-Hämmerlin framework

Preamble - The main purpose of this chapter is to introduce the reader to gradient optimization techniques. The derivation of the adjoint problem and the computation of gradients are described in detail. The optimization algorithm is applied to the search of optimal disturbances and optimal control in the simplified framework of Görtler-Hämmerlin disturbances.

The Görtler-Hämmerlin assumption can be viewed as the analogue in swept Hiemenz flow of two-dimensional perturbation assumptions in classical two-dimensional boundary layers. The wall-normal v and spanwise w perturbation velocity components are assumed to be homogeneous in the chordwise $x-$direction; mass conservation requires that the chordwise $u-$component increases linearly away from the attachment-line.

In two-dimensional shear flows the two-dimensional assumption may be justified by Squire's theorem according to which the first unstable mode is itself two-dimensional. In a developing Blasius boundary layer, for instance, the first unstable mode takes the shape of two-dimensional Tollmien-Schlichting waves. Although Squire's theorem does not apply to swept Hiemenz flow, which is three-dimensional, the most unstable mode takes the shape of a Görtler-Hämmerlin mode. Experiments by Pfenninger and Bacon (1969) showed that disturbances along the swept leading edge of a blunt body were essentially two-dimensional when the ambient turbulence level was low. Thus, in addition to providing a simplified framework within which gradient optimization techniques may be introduced, the 'two-dimensional' Görtler-Hämmerlin assumption is expected to render a trueful picture of early instabilities

in swept Hiemenz flow.

Optimal energy growth and optimal control in swept Hiemenz flow

Alan Guégan[1], Peter J. Schmid[12] and Patrick Huerre[1]

[1]Laboratoire d'Hydrodynamique (LadHyX), CNRS – École Polytechnique, F-91128 Palaiseau, France
[2]Department of Applied Mathematics, University of Washington, Seattle, WA 98195–2420, USA

Published in the Journal of Fluid Mechanics, vol. 566, pp. 11–45.

Abstract

The objective of the study is first to examine the optimal transient growth of Görtler-Hämmerlin perturbations in swept Hiemenz flow. This configuration constitutes a model of the flow in the attachment-line boundary layer at the leading-edge of swept wings. The optimal blowing and suction at the wall which minimizes the energy of the optimal perturbations is then determined. An adjoint-based optimization procedure applicable to both problems is devised, which relies on the maximization or minimization of a suitable objective functional. The variational analysis is carried out in the framework of the set of linear partial differential equations governing the chordwise and wall-normal velocity fluctuations. Energy amplifications of up to three orders of magnitude are achieved at low spanwise wavenumbers ($k \sim 0.1$) and large sweep Reynolds number ($Re \sim 2000$). Optimal perturbations consist of spanwise travelling chordwise vortices, with a vorticity distribution which is inclined against the sweep. Transient growth arises from the tilting of the vorticity distribution by the spanwise shear via a two-dimensional Orr mechanism acting in the basic flow dividing plane. Two distinct régimes have been identified: for $k \lesssim 0.25$, vortex dipoles are formed which induce large spanwise perturbation velocities; for $k \gtrsim 0.25$, dipoles are not observed and only the Orr mechanism remains active. The optimal wall blowing control yields for instance an 80% decrease of the maximum perturbation kinetic energy reached by optimal disturbances at $Re = 550$ and $k = 0.25$. The optimal wall blowing pattern consists of spanwise travelling waves which follow the naturally occurring vortices and qualitatively act in the same manner as a more simple constant gain feedback control strategy.

2.1 Introduction

Fundamental studies of hydrodynamic instabilities in boundary layers have been motivated by the need to suppress or delay transition to turbulence over aircraft lift-generating devices. Most classical investigations have been concerned with the boundary layers on the upper and lower surfaces when the flow may be regarded as weakly non parallel and disturbances governed by the Orr-Sommerfeld equation or any of its extensions. Relatively little attention has been given to the highly three-dimensional region at the leading-edge. The main objective of the present study is to determine the optimal energy growth sustainable by disturbances in the swept-attachment line boundary layer otherwise known as swept Hiemenz flow. An optimal control strategy based on blowing and suction at the wall is then devised in order to quench these perturbations.

Early experimental studies of swept wing attachment-line boundary layers (Gregory 1960, Gaster (1967), Cumpsty and Head (1969), Pfenninger and Bacon (1969), Pfenninger (1977)) were motivated by the need to keep the flow in this region laminar, in order to prevent premature transition downstream over the wing surface. Cross-flow instabilities appearing away from the attachment line were then thought to be responsible for early transition. The reader is referred to Koch et al. (2000) for a recent thoretical and numerical study of crossflow vortices in three-dimensional boundary layers and their secondary instability. Poll (1979) emphasized that instabilities at the attachment line, intrinsic to the leading-edge boundary layer, could also play a significant role in this process. The present investigation focuses on the naturally occurring instability originating at the attachment-line and its control.

A satisfactory model of the steady flow near the attachment-line is given by the Hiemenz (1911) stagnation point solution to which is superimposed a spanwise velocity component. The linear instability properties of this highly non-parallel basic flow have been the subject of conflicting statements regarding the assumed behavior of fluctuations outside the boundary layer. The main conclusions may be summarized as follows.

Under the so-called Görtler (1955)-Hämmerlin (1955) separation of variables assumption (2.5) and exponential decay of the perturbations in the wall-normal direction, Hiemenz stagnation flow without sweep was conclusively demonstrated to be linearly stable by Wilson and Gladwell (1978). Lyell and Huerre (1985) showed that the previously suspected centrifugal instability mechanism was indeed present but too weak to counteract the stabilizing effect of viscous diffusion. They further concluded to the possibility of a finite-amplitude instability on the basis of a highly truncated Galerkin model of the nonlinear dynamics. The direct numerical simulations of Spalart (1988) failed to detect any evidence for such a nonlinear instability

in pure Hiemenz flow. The restrictive Görtler-Hämmerlin assumption was first relaxed in the study of Brattkus and Davis (1991) by expanding perturbations in series of Hermite polynomials along the chordwise direction. Algebraically decaying disturbances in the wall-normal direction, which are associated to the continuous spectrum, were shown by Dhanak and Stuart (1995) to arise from fluctuations forced from outside the boundary layer.

The presence of sweep significantly modifies the above results. According to Hall, Malik & Poll (1984), who led a study under the Görtler-Hämmerlin assumption, there exists a critical value $Re_c = 583.1$ of the sweep Reynolds number (defined in section 2.2) above which swept Hiemenz flow becomes linearly unstable. Sufficiently strong steady wall suction makes the flow stable while blowing has a destabilizing effect. Furthermore, a weakly nonlinear analysis (Hall and Malik (1986)) reveals the bifurcation to be subcritical close to Re_c. This result is in qualitative agreement with the direct numerical simulations of Spalart (1988) for swept Hiemenz flow where subcritical turbulent states were observed below Re_c. Lin and Malik (1996), Theofilis et al. (2003) and Obrist and Schmid (2003a) have extended the linear analysis to more general chordwise polynomial expansions in the same spirit as Brattkus and Davis (1991). The Görtler-Hämmerlin modes are then found to be the least stable. According to the direct numerical simulations of Joslin (1995), the nonlinear spatial evolution of two-dimensional and three-dimensional disturbances is in line with the temporal instability results of Hall *et al.* (1986). Swept Hiemenz flow indeed becomes linearly unstable at sufficiently large Reynolds numbers and wall suction strongly stabilizes the flow. However, no definite evidence for the subcritical instability was found. Theofilis (1998) carried out a comprehensive comparison between simulations of the full nonlinear equations and the linear instability analysis both under the Görtler-Hämmerlin separation of variable assumption. Excellent agreement was obtained in the supercritical range. Again, no finite amplitude subcritical instability was clearly exhibited, which was ascribed to the restrictive nature of the Görtler-Hämmerlin assumption.

It is now well established that classical linear instability analyses need to be complemented with a study of the transient growth properties of non-modal perturbations (Gustavsson (1991), Butler and Farrell (1992), Trefethen et al. (1993)). For a general account of the underlying theoretical framework, the reader is referred to the book of Schmid and Henningson (2001). In the specific context of swept Hiemenz flow, Obrist and Schmid (2003b) demonstrated that, within the limitations of a finite eigenfunction basis, Görtler-Hämmerlin perturbations could support an energy amplification of the order of 100 in the linearly stable régime, both at low and high spanwise wavenumbers, provided that the Reynolds number is large enough. The investigation was carried out by resorting to a standard Singular Value Decomposition method applied to the gain matrix over a finite time interval. In the present

study, the issue of transient temporal growth is examined anew by implementing an adjoint-based optimization formulation (see, for instance, Gunzburger 1997) in order to determine the perturbation of maximum growth. A similar methodology has been used in Andersson et al. (1999) and Luchini (2000) to examine optimal streamwise amplification in the Blasius boundary layer. The analysis developed in section 2.3 is inspired by the procedure proposed by Corbett and Bottaro (2001b) to identify optimal disturbances in swept boundary layers in a temporal setting.

For an assessment of the current status of laminar flow control technology in an aeronautical context, the reader is referred to the comprehensive review of Joslin (1998) and the book of Gad-el Hak (2000). At a more fundamental level, applications of control theory (Abergel and Témam (1990)) to the delay of boundary layer transition have recently led to very encouraging results. For general accounts and reviews of the applications of control theory to transitional or turbulent flows, the reader is referred to Gunzburger (1997), Lumley and Blossey (1998) and Bewley (2001) among others. We restrict here the discussion to studies that are directly relevant to this investigation, namely optimal control methodologies involving adjoint formulations in a continuous setting and applied to boundary layer transition. More specifically, the optimal control problem for perturbations within the flow is viewed as the minimization of an objective functional involving a measure of the perturbation energy, under the constraint that disturbances satisfy for instance the linear Navier-Stokes equations (Gunzburger 1997, Joslin et al. (1997)). For that purpose, an iterative method based on the calculation of the gradient of the objective functional with respect to the control variables, e.g. wall blowing/suction, is implemented in order to reach a local minimum in function space. The gradient vector of the objective functional may conveniently be expressed in terms of an adjoint state which is solution of an adjoint system of equations and boundary conditions. Such a formulation is carried out in the context of continuous linear instability partial differential equations. Discretization is only performed *a posteriori* in order to effectively solve numerically the direct and adjoint systems. Other formulations, which are not considered here, involve instead an *a priori* discretization before resorting to an optimization scheme. Such approaches are appropriate when the evaluation of the gradient of th objective functional in terms of the adjoint is numerically delicate.

Another issue concerns the so-called off-line versus on-line formulation of control problems. In the present investigation the optimization is performed off-line, i.e. the optimal control is determined once and for all for a given initial state. By contrast, on-line formulations rely on the determination of feedback laws. The procedure then often involves solving a Riccati equation, thereby leading to a gain matrix directly relating the control to the state of the system, as extensively reviewed in Bewley (2001). Such approaches lead to efficient feedback control laws in plane channel

flow, as demonstrated for a single Fourier mode in two dimensions by Joshi et al. (1997) and in three dimensions by Bewley and Liu (1998). Högberg et al. (2003) successfully generalized the procedure to arbitrary initial disturbances in physical space. A similar framework has been adopted by Högberg and Henningson (2002) to control various unstable perturbations in spatially-evolving three dimensional boundary layers.

In the continuous framework and following the general adjoint-based optimization methodology put forward by Joslin *et al.* (1997), Cathalifaud and Luchini (2000) determined the optimal streamwise distribution of wall blowing and suction which minimizes the perturbation energy of the incoming disturbance of maximum growth in two-dimensional boundary layers on a flat or curved plate. Walther et al. (2001) implemented a similar formulation to compute the optimal wall transpiration capable of quenching the streamwise development of two-dimensional Tollmien-Schlichting waves in a spatially developing boundary layer. The evolution of instability waves was assumed to be governed by the linear parabolic stability equations. Several orders of magnitude reductions in perturbation energy were achieved. A similar methodology has been applied by Pralits et al. (2002) to control the growth of various classes of disturbances in three-dimensional boundary layers. A sophisticated generalization of this type of approach has been proposed by Bewley et al. (2001) in order to control turbulence in direct numerical simulations of plane channel flow at Reynolds numbers of 1712 and 3247. A so-called 'receding-horizon' predictive control strategy was devised, in which the optimal blowing/suction control sequence is calculated on a given short time horizon, the flow being frozen. This short-time optimal control is then applied to advance the flow during a fraction of this time horizon. This process is repeated until the flow is fully relaminarized. The optimal control framework has also been applied in a linear setting by Corbett and Bottaro (2001a) to attenuate via unsteady suction and blowing the optimal temporally evolving perturbation in swept boundary layers calculated by Corbett and Bottaro (2001b). The perturbation kinetic energy amplification was shown to be reduced by an order of magnitude in accelerated boundary layers.

The present investigation differs from previous optimal control analyses in the following aspects. The optimization scheme, used for the determination of both the optimal disturbance and the optimal suction/blowing control sequence is developed for a highly non-parallel basic flow, instead of the strictly parallel plane Poiseuille flow or weakly non-parallel boundary layers. Disturbances are assumed to satisfy the Görtler-Hämmerlin separation of variable assumption (2.5). As in previous studies discussed above, the optimization procedure is carried out in a continuous setting on a reduced set of linear partial differential equations governing the evolution of the chordwise (u) and wall-normal (v) velocity perturbations, in the same spirit as for instance Corbett & Bottaro (2001a,b). However, it is argued that the reduc-

tion to a $u-v$ formulation requires a non-trivial adaptation of existing approaches, namely, the introduction of a suitable set of scalar products. As a result, the different components of the gradient of the objective functional are directly accessible in a reduced $u-v$ setting. Gradient algorithms are then readily available to home in on a local optimum of the objective function. Finally, a new physical mechanism responsible for the growth of non-modal perturbations is identified which also provides a qualitative explanation for the efficiency of the control.

The paper is organized as follows. The basic flow and the Görtler-Hämmerlin linear perturbation model are introduced and defined in section 2.2. The optimization approach common to the optimal perturbation and optimal control analyses is detailed in section 2.3. Application to swept Hiemenz flow and numerical issues are addressed in section 2.4. Section 2.5 provides the underlying physical mechanisms at low and high spanwise wavenumbers respectively. Optimal control is examined in section 2.6 and compared with a constant gain feedback control law reminiscent of opposition control. A summary of the main findings is given in section 2.7 and additional remarks are made regarding the particular features of the growth mechanism, as compared to its classical boundary layer counterpart.

2.2 Linear perturbation model

As a uniform flow impinges on the swept leading edge of an airfoil (Figure 2.1), or any blunt body, an attachment-line boundary layer forms in the vicinity of the stagnation line. In the neighborhood of the stagnation line, the leading edge can be modeled locally by a flat wall perpendicular to the main stream. Cartesian coordinates (x, y, z) are then introduced where the normal coordinate direction y is perpendicular to the wall and points upstream, z and x denote the spanwise and chordwise direction, respectively (Figure 2.1), and the base flow divides symmetrically over each side of the (y, z) dividing plane. This model, known as swept Hiemenz flow, provides a widely accepted description of the steady flow near the stagnation region.

The Reynolds number of the flow is based on the free stream sweep velocity W_∞, the kinematic viscosity ν and the length scale $\delta = (\nu/S)^{\frac{1}{2}}$, with $S = (dU/dx)_{y\to\infty}$ denoting the strain rate of the irrotational outer flow and U the chordwise velocity of the base flow. The Reynolds number thus defined

$$Re = \frac{W_\infty \delta}{\nu} \tag{2.1}$$

represents a measure of the sweep angle where $Re = 0$ corresponds to unswept

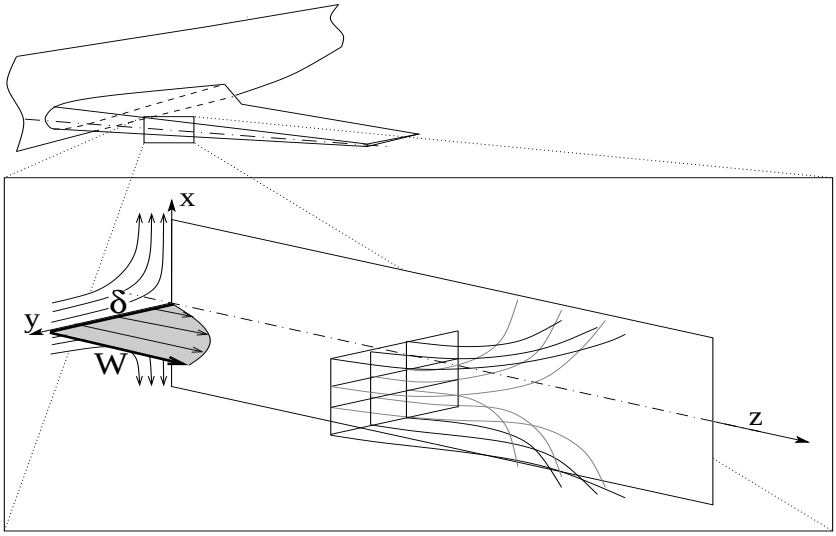

Figure 2.1: Sketch of the leading-edge boundary layer forming near the stagnation region of a swept wing. The inset further simplifies the flow geometry by neglecting curvature effects of the leading edge. Both the basic profile and streamlines are displayed.

Hiemenz flow.

The base flow (U, V, W) is assumed to be steady and independent of the spanwise z coordinate. Following Hiemenz (1911), the chordwise velocity U is taken to be linearly dependent on x, while the normal velocity V depends on y only, as does the spanwise velocity W. Under these assumptions, the base flow takes the form

$$\begin{aligned} U &= xRe^{-1}F'(y) \ , && \text{(2.2a)} \\ V &= -Re^{-1}F(y) \ , && \text{(2.2b)} \\ W &= W(y) \ , && \text{(2.2c)} \end{aligned}$$

where the prime denotes differentiation with respect to y, and $F(y)$ and $W(y)$ satisfy the ordinary differential equations

$$\begin{aligned} F''' - (F')^2 + FF'' + 1 &= 0 \ , && \text{(2.3a)} \\ FW' + W'' &= 0 \ , && \text{(2.3b)} \end{aligned}$$

with the boundary conditions

$$F(0) = F'(0) = W(0) = 0, \tag{2.4a}$$
$$F'(\infty) = 1, \qquad W(\infty) = 1. \tag{2.4b}$$

Swept Hiemenz flow constitutes an exact solution of the steady incompressible Navier-Stokes equations; its general shape and streamlines are sketched in Figure 2.1. For further reference, the thickness of the boundary layer based on the spanwise velocity profile is 3.05 in non-dimensional units. This model is valid only close to the attachment line since the chordwise velocity component becomes unbounded for increasing x. Despite these limitations, the above model is in good agreement with experiments (Gaster (1967), Poll 1979).

In the following analysis we further assume the perturbations $(\hat{u},\ \hat{v},\ \hat{w},\ \hat{p})$ of the basic flow to display the same chordwise structure, i.e. $\hat{u}$ scales linearly in the chordwise x direction and $\hat{v}$ and $\hat{w}$ are independent of x. This assumption is commonly referred to as the Görtler (1955)-Hämmerlin (1955) assumption. The total velocity and pressure fields therefore read

$$\begin{pmatrix} u \\ v \\ w \\ p \end{pmatrix} = \begin{pmatrix} xRe^{-1}F'(y) \\ -Re^{-1}F(y) \\ W(y) \\ P(x,y) \end{pmatrix} + \begin{pmatrix} x\hat{u}(y,z,t) \\ \hat{v}(y,z,t) \\ \hat{w}(y,z,t) \\ \hat{p}(x,y,z,t) \end{pmatrix}. \tag{2.5}$$

Translational invariance in the spanwise $z-$direction allows to expand perturbations into Fourier series in z. The Fourier coefficients $(\check{u}, \check{v}, \check{w}, \check{p})$ corresponding to a given spanwise wavenumber k satisfy the linear system of perturbation equations

$$\left(\frac{\partial}{\partial t} - F\frac{\partial}{\partial y} - \Delta + ikReW + 2F'\right)\check{u} + F''\check{v} = 0, \tag{2.6a}$$
$$\left(\frac{\partial}{\partial t} - F\frac{\partial}{\partial y} - \Delta + ikReW - F'\right)\check{v} + \frac{\partial \check{p}}{\partial y} = 0, \tag{2.6b}$$
$$\left(\frac{\partial}{\partial t} - F\frac{\partial}{\partial y} - \Delta + ikReW\right)\check{w} + ReW'\check{v} + ik\check{p} = 0, \tag{2.6c}$$
$$\check{u} + \frac{\partial \check{v}}{\partial y} + ik\check{w} = 0, \tag{2.6d}$$

with $\Delta = \partial^2/\partial y^2 - k^2$.

The above equations (2.6) are referred to as the direct system. The no-slip condition at the wall and the requirement that perturbations vanish for large y imply the following direct boundary conditions:

$$\check{u} = \check{w} = 0 \qquad \text{at} \qquad y = 0 \ , \tag{2.7a}$$

$$\check{v} = \check{v}_w(t) \qquad \text{at} \qquad y = 0 \ , \tag{2.7b}$$

$$\check{u} = \check{v} = \check{w} = 0 \qquad \text{at} \qquad y = \infty \ , \tag{2.7c}$$

where $\check{v}_w(t)$ stands for the imposed wall-normal blowing/suction velocity in the flow control context. When the optimal perturbation problem is considered, it is understood that $\hat{v}_w(t) = 0$.

Upon eliminating the pressure and spanwise velocity perturbations, the system (2.6) reduces to

$$\mathcal{A}\frac{\partial}{\partial t}\begin{bmatrix}\check{v}\\ \check{u}\end{bmatrix} + \mathcal{B}\begin{bmatrix}\check{v}\\ \check{u}\end{bmatrix} = 0, \tag{2.8}$$

where the $y-$differential operators $\mathcal{A}$ and $\mathcal{B}$ stand for

$$\mathcal{A} = \begin{bmatrix}\Delta & 0\\ 0 & 1\end{bmatrix}, \tag{2.9a}$$

$$\mathcal{B} = \begin{bmatrix} (-F' - F\frac{\partial}{\partial y} - \Delta + ikReW)\Delta & -2F'' - 2F'\frac{\partial}{\partial y} \\ \quad - F''' - F''\frac{\partial}{\partial y} - ikReW'' & \\ F'' & -F\frac{\partial}{\partial y} - \Delta + ikReW + 2F' \end{bmatrix} \tag{2.9b}$$

with the boundary conditions

$$\check{u} = \frac{\partial \check{v}}{\partial y} = 0 \qquad \text{at} \qquad y = 0, \tag{2.10a}$$

$$\check{v} = \check{v}_w(t) \qquad \text{at} \qquad y = 0, \tag{2.10b}$$

$$\check{u} = \check{v} = \frac{\partial \check{v}}{\partial y} = 0 \qquad \text{at} \qquad y = \infty. \tag{2.10c}$$

The linear stability properties of (2.8)-(2.10) have previously been studied by Hall *et al.* (1984). The possibility of non-modal transient energy growth has been demonstrated in Obrist and Schmid (2003b).

Quantity	Symbol	Meaning
	$E(t)$	kinetic energy of the perturbations at time t integrated over a box centered about the attachment-line, $E(t) = \frac{\sqrt{3}}{2}\int_{-\sqrt{3}}^{\sqrt{3}}\int_0^\infty\int_0^{1/k}(x^2u^*u + v^*v + w^*w)\,dxdydz$, i.e. $E(t) = \int_0^\infty(u^*u + v^*v + w^*w)\,dy$
Energy	E_{max}	maximum kinetic energy reached by the overall optimal perturbation
	G_{max}	maximum kinetic energy growth sustainable by a combination of eigenfunctions as computed by Obrist and Schmid (2003b)
	T_p	optimization time used to compute finite-time optimal perturbations
Time	T_c	optimization time used to compute the optimal control
	T	optimization time, T_p or T_c, depending on the context
	T_{max}	time when the energy maximum E_{max} is reached

Table 2.1: Nomenclature for energy and time quantities.

In what follows the $\check{}$ sign is omitted. The state vector and the applied wall blowing/suction are denoted $q = (v, u)^T$ and $q_w = (v_w, u_w = 0)^T$ respectively.

2.3 Elements of optimization theory

Two general goals are pursued in this study: first, the initial perturbation that results in a maximum energy growth over a specified time interval $[0, T_p]$ is determined; second, the optimal wall blowing and suction sequence applied over a given time interval $[0, T_c]$ is sought so that the energy growth of this initial perturbation is minimized. In general, the time interval T_p may differ from T_c. We use the convention that T, with no subscript, can equally represent T_p or T_c. For the sake of clarity, Table 2.1 summarizes the principal notations.

The general approach is fairly straightforward (Gunzburger 1997, Bewley 2001 among others): given the governing linear equations (2.8)-(2.10) and a quantified objective, standard optimization techniques are employed to find the optimal perturbation, or the optimal control wall-normal blowing to suppress the growth of perturbations. Optimization variables – such as, in our case, the initial condition $q(y, 0)$ or the blowing/suction time series $q_w(t)$ – are iteratively improved until the stated objective – such as maximum or minimum energy growth over a finite time

span – is achieved. Gradient-based optimization techniques (Press et al. (1992)) have been widely used for this purpose, as they are very efficient and applicable to large-scale systems. In general, gradient-based optimization algorithms require the following three essential components: (i) an objective functional $\mathcal{I}$ that provides a performance measure with respect to the adjustable optimization variables; (ii) an algorithm to compute the gradient of the objective functional with respect to the optimization variables; (iii) a technique to improve the previous set of optimization variables based on the objective functional gradient.

An iterative algorithm based on these three steps leads, when carefully designed, to a locally optimal set of optimization variables. The present section provides the foundations underlying the design of the optimization procedure. Andersson *et al.* (1999) and Corbett and Bottaro (2001b) provided a very convenient framework which is used as a starting point for the analysis. However, significant extensions and improvements proved to be necessary in order to arrive at a workable formulation, as outlined below.

2.3.1 Objective functional and scalar products

The objective functional represents a measure of how well the objectives of the optimization procedure have been attained. In our case the functional

$$\mathcal{I} = \frac{E(T)}{E(0)} + \frac{\alpha^2}{2}\frac{1}{T}\int_0^T E(t)dt + \frac{l^2}{2} \ll q_w, q_w \gg \tag{2.11}$$

is used. The scalar product $\ll ., . \gg$ appearing in (2.11) is defined as

$$\ll q_1, q_2 \gg = \frac{1}{T}\int_0^T q_1^* M_\diamondsuit q_2 \; dt + c.c., \tag{2.12}$$

where the symbol *c.c.* denotes the complex conjugate. The scalar product $\ll q_w, q_w \gg$ is then a suitably weighted measure of the wall-blowing energy, as further discussed below. Similarly, the scalar product

$$[\![q_1, q_2]\!] = \int_0^\infty q_1^* M_\square q_2 \; dy + c.c. \tag{2.13}$$

is introduced so that the perturbation kinetic energy at time t defined in Table 2.1 may be expressed as $E(t) = [\![q(y,t), q(y,t)]\!]$, i.e. solely in terms of the velocity components u and v.

The linear differential operators $M_\square$ and $M_\diamondsuit$ appearing in the definitions of the perturbation energy and the wall blowing energy via the scalar products (2.12) and (2.13) arise from the following considerations: by taking advantage of the continuity equation and the boundary conditions (2.10), one finds through successive integrations by parts applied to $E(t)$ defined in Table 2.1 that

$$M_\square = -\frac{1}{k^2}\begin{bmatrix} \Delta & \frac{\partial}{\partial y} \\ -\frac{\partial}{\partial y} & -1-k^2 \end{bmatrix} . \tag{2.14}$$

The operator $M_\diamondsuit$ appearing in (2.12) is chosen to be

$$M_\diamondsuit = \begin{bmatrix} s_\diamondsuit(t) & 0 \\ 0 & 0 \end{bmatrix} , \tag{2.15}$$

where the switch function $s_\diamondsuit(t)$ is a suitably chosen scalar function. If $s_\diamondsuit$ were set to unity between $t = 0$ and $t = T_c$, the control energy appearing in (2.11) would simply be the kinetic energy $\ll q_w, q_w \gg = \frac{1}{T_c}\int_0^{T_c} v_w^* v_w \, dt$ of the wall-normal velocity v_w. However, strong blowing at $t = 0$ or $t = T_c$ results in numerical difficulties. By setting $s_\diamondsuit(t)$ to take very high values at both ends of the control time interval (Corbett & Bottaro 2001b), strong blowing or suction at $t = 0$ or T_c is automatically discarded by the optimization algorithm since their weighted blowing energy $\ll q_w, q_w \gg$ is too high. In the present computations, a function of the form $s_\diamondsuit(t) = 1/(1 - exp[-t^2] - exp[-(T_c - t)^2])$ has been chosen, which is nearly unity for most of the control time interval $[0, T_c]$, but tends to infinity at both end points.

As outlined in section 2.3.2, the optimization procedure requires the introduction of Lagrange multipliers, or so-called adjoint variables $\tilde{q}(y,t)$, $\tilde{q}_0(y)$ and $\tilde{q}_w(t)$, and three additional scalar products

$$(\tilde{q}_1, \tilde{q}_2) = \int_0^T \int_0^\infty \tilde{q}_1^* . \tilde{q}_2 \; dydt + c.c. \; , \tag{2.16a}$$

$$[\tilde{q}_1, \tilde{q}_2] = \int_0^\infty \tilde{q}_1^* . \tilde{q}_2 \; dy + c.c. \; , \tag{2.16b}$$

$$< \tilde{q}_1, \tilde{q}_2 > = \int_0^T \tilde{q}_1^* . \tilde{q}_2 \; dt + c.c. \; . \tag{2.16c}$$

A single vector space $\Omega = q \times q_0 \times q_w \times \tilde{q} \times \tilde{q}_0 \times \tilde{q}_w$ including all the direct and adjoint variables may naturally be introduced. A scalar product combining all the previous ones

$$\{Q^1, Q^2\} = (q^1, q^2) + [\![q_0^1, q_0^2]\!] + \ll q_w^1, q_w^2 \gg + (\tilde{q}^1, \tilde{q}^2) + [\tilde{q}_0^1, \tilde{q}_0^2] + < \tilde{q}_w^1, \tilde{q}_w^2 > \quad (2.17)$$

is then conveniently defined for arbitrary elements $Q^i = (q^i, q_0^i, q_w^i, \tilde{q}^i, \tilde{q}_0^i, \tilde{q}_w^i)$ of Ω. In section 2.3.2 it is demonstrated that the six scalar products (2.12), (2.13), (2.16a), (2.16b), (2.16c) and (2.17) are indeed necessary to correctly formulate the optimization procedure in the reduced $u - v$ setting.

The form of the objective functional (2.11) has been suggested by Corbett & Bottaro (2001b), among others. The first term $E(T)/E(0)$ stands for the energy amplification between $t = 0$ and T. In searching for optimal initial perturbations, one tries to maximize this term; by contrast, in searching for optimal control strategies, the objective is to minimize it. One should notice that, as the optimal perturbation is the initial disturbance, the energy of which increases the most between $t = 0$ and T_p, the control parameters α and l are set to zero when computing the optimal perturbation. The objective functional then reduces to the energy amplification term.

The control problem may similarly be regarded as the minimization of the energy ratio $E(T)/E(0)$ for a given initial condition. This procedure does not necessarily yield acceptable results since it does not take into consideration the energy evolution over the full time interval. Substantial energy levels may still be reached between $t = 0$ and $t = T_c$ (Corbett & Bottaro 2001b) unless one also includes the term $\frac{\alpha^2}{2}\frac{1}{T}\int_0^T E(t)dt$ which acts as a penalty for excessive transient energy growth within the optimization interval. In the sequel the quantity $\frac{1}{T}\int_0^T E(t)dt$ is referred to as the mean energy.

It is also important to include the third term $\frac{l^2}{2} \ll q_w, q_w \gg$ in (2.11), which is a measure of the control cost, in order to avoid excessively strong blowing. The penalty parameter l allows us to set the 'price' of any control effort by weighing the control energy $\ll q_w, q_w \gg$ within the objective functional.

The two penalty parameters α and l thus aid in refining and tuning the objective functional by suitably weighing each of its terms.

2.3.2 Lagrangian formulation

To compute the gradient of $\mathcal{I}$ both with respect to the initial condition q_0 and the wall-normal blowing sequence q_w, a Lagrangian-based approach (Gunzburger

1997) is used. This method has the advantage to not only provide the optimality conditions (Corbett & Bottaro 2001a), but also an expression for the gradient of the objective functional $\mathcal{I}$.

Following Andersson *et al.* (1999), Corbett & Bottaro (2001a,b) and Pralits *et al.* (2002) it is convenient to rewrite the linear system (2.8)-(2.10) governing the reduced state vector $q = (v, u)^T$ in the form

$$\begin{aligned}
\text{reduced system of equations} \qquad & F(q) = \frac{\partial}{\partial t}(A_i \frac{\partial^i q}{\partial y^i}) + B_j \frac{\partial^j q}{\partial y^j} = 0, && \text{(2.18a)} \\
\text{initial conditions} \qquad & G(q, q_0) = q(y, 0) - q_0(y) = 0, && \text{(2.18b)} \\
\text{boundary conditions} \qquad & H(q, q_w) = q(0, t) - q_w(t) = 0, && \text{(2.18c)}
\end{aligned}$$

where the Einstein summation convention has been introduced to yield a compact as well as general form for the partial differential equations. The y-dependent matrices A_i and B_j give the respective weights on each of the derivatives $\partial^i./\partial y^i$ and $\partial^j./\partial y^j$ applied to the variables u, v. In the direct problem (2.8)-(2.10) the sub- and superscripts i and j range from zero to two and from zero to four, respectively. In addition, it is further assumed that the boundary conditions at infinity, as well as the remaining boundary conditions at the wall are satisfied.

The linear system (2.18), can be viewed as a set of equality constraints associated with the optimization problem for the objective functional $\mathcal{I}$. For sufficiently smooth functions F, G, H, the constrained problem can be transformed into an unconstrained one by introducing the Lagrangian

$$\mathcal{L}(q, q_0, q_w, \tilde{q}, \tilde{q}_0, \tilde{q}_w) = \mathcal{I} - (\tilde{q}, F(q)) - [\tilde{q}_0, G(q, q_0)] - < \tilde{q}_w, H(q, q_w) > \ . \qquad (2.19)$$

The Lagrange multipliers $\tilde{q} = (\tilde{v}, \tilde{u})^T, \tilde{q}_0 = (\tilde{v}_0, \tilde{u}_0)^T, \tilde{q}_w = (\tilde{v}_w, \tilde{u}_w)^T$ are referred to as the adjoint variables. The Lagrangian (2.19) is defined even when the constraints are not enforced. For this reason, the variables $q,\ q_0,\ q_w,\ \tilde{q},\ \tilde{q}_0,\ \tilde{q}_w$ can be considered as mutually independent.

The Lagrangian $\mathcal{L}$ is assumed to be differentiable on the vector space Ω introduced in section 2.3.1 and may then have stationary points where all its derivatives are equal to zero. We will see next that at these stationary points the system of equations (2.18) is satisfied, and the objective functional $\mathcal{I}$ is stationary. In other words, the solutions of the optimization problem lie at the stationary points of the Lagrangian. At such points the components of the vector $Q = \{q, q_0, q_w, \tilde{q}, \tilde{q}_0, \tilde{q}_w\}$ satisfy equations that are referred to as the optimality conditions.

The advantage of the Lagrangian-based formulation is that $\mathcal{L}$ is defined on the entire vector space Ω whereas $\mathcal{I}$ is only defined on the subdomain Ω_c of Ω, where the system (2.18) is satisfied. An analytic expression for the gradient of the Lagrangian is available at every point in Ω, from which an analytic expression of the gradient of $\mathcal{I}$ on Ω_c can be derived. This gradient information is then used to implement the main step in the gradient-based optimization algorithm.

2.3.3 Gradient of the objective functional

The Gateau differential $d\mathcal{L}$ of the Lagrangian evaluated at point Q is defined as

$$d\mathcal{L}|_Q(\delta Q) = \lim_{\varepsilon \to 0} \frac{\mathcal{L}(Q + \varepsilon \delta Q) - \mathcal{L}(Q)}{\varepsilon} \ . \tag{2.20}$$

Assuming that $\mathcal{L}$ is Fréchet-differentiable the gradient of the Lagrangian at point Q, denoted $\nabla\mathcal{L}(Q)$, is such that for any vector δQ the following expression holds :

$$\{\nabla\mathcal{L}(Q), \delta Q\} = d\mathcal{L}|_Q(\delta Q) \ , \tag{2.21}$$

with the scalar product introduced in (2.17). The projections of $\nabla\mathcal{L}(Q)$ onto the subspaces $\mathtt{span}\{q, 0, 0, 0, 0, 0\}$, $\mathtt{span}\{0, q_0, 0, 0, 0, 0\}$, etc. are denoted by the more convenient symbols $\nabla_q\mathcal{L}$, $\nabla_{q_0}\mathcal{L}, \ldots$ and referred to as either " the q, q_0, etc. component of the gradient" or "the gradient with respect to q, q_0, etc."

The common procedure in flow control (Gunzburger 1997, Andersson *et al.* 1999, Corbett & Bottaro 2001a,b and Pralits *et al.* 2002) is to compute, first, the gradients of the Lagrangian with respect to the adjoint variables $\tilde{q}$, $\tilde{q}_0$, $\tilde{q}_w$, and, second, the gradient with respect to the flow field q. From these calculations, one can recover the direct and adjoint systems, as well as the direct and adjoint boundary conditions. The gradients of the Lagrangian with respect to the control variables q_0 and q_w, i.e., the initial perturbation and the wall blowing/suction velocity, are computed last and yield analytic expressions for the gradients of the objective functional with respect to q_0 and q_w.

Differentiating (2.19) with respect to the adjoint variables yields

$$\begin{aligned}
(\nabla_{\tilde{q}}\mathcal{L}(Q), \delta\tilde{q}) &= -(\delta\tilde{q}, F(q)), && \text{(2.22a)}\\
[\nabla_{\tilde{q}_0}\mathcal{L}(Q), \delta\tilde{q}_0] &= -[\delta\tilde{q}_0, G(q, q_0)], && \text{(2.22b)}\\
< \nabla_{\tilde{q}_w}\mathcal{L}(Q), \delta\tilde{q}_w > &= - < \delta\tilde{q}_w, H(q, q_w) > . && \text{(2.22c)}
\end{aligned}$$

At the stationary points of the Lagrangian $\mathcal{L}$ all three gradients are by definition equal to zero. As the variational terms $\delta\tilde{q},\ \delta\tilde{q}_0,\ \delta\tilde{q}_w$ may be chosen arbitrarily, F, G, and H necessarily have to vanish thus satisfying the direct system of equations (2.18).

Differentiating (2.19) with respect to the control q_w yields

$$\ll \nabla_{q_w}\mathcal{L}(Q), \delta q_w \gg = l^2 \ll q_w, \delta q_w \gg + < \tilde{q}_w, \delta q_w > . \tag{2.23}$$

Bearing in mind the definitions (2.12) and (2.16c) of the scalar products $\ll ., . \gg$ and $< ., . >$, we may write

$$< \tilde{q}_w, \delta q_w > = \ll \tilde{q}_w, M_\Diamond^{-1}\delta q_w \gg = \ll M_\Diamond^{-1}\tilde{q}_w, \delta q_w \gg, \tag{2.24}$$

where $M_\Diamond^{-1}$ denotes the matrix $\begin{bmatrix}(1/s_\Diamond) & 0\\ 0 & 0\end{bmatrix}$. Equation (2.23) may then be rewritten as

$$\ll \nabla_{q_w}\mathcal{L}(Q), \delta q_w \gg = l^2 \ll q_w, \delta q_w \gg + \ll M_\Diamond^{-1}\tilde{q}_w, \delta q_w \gg . \tag{2.25}$$

This expression has to hold true for any δq_w which entails

$$\nabla_{q_w}\mathcal{L}(Q) = l^2 q_w + M_\Diamond^{-1}\tilde{q}_w. \tag{2.26}$$

At the stationary points of $\mathcal{L}$, the gradient $\nabla_{q_w}\mathcal{L}$ vanishes, thereby yielding the first optimality condition

$$l^2 q_w + M_\Diamond^{-1}\tilde{q}_w = 0. \tag{2.27}$$

Differentiation of (2.19) with respect to the initial perturbation q_0 leads to

$$[\![\nabla_{q_0}\mathcal{L}(Q), \delta q_0]\!] = -2\frac{E(T)}{E(0)^2}[\![q_0, \delta q_0]\!] + [\tilde{q}_0, \delta q_0], \tag{2.28}$$

which, according to definitions (2.13) and (2.16b), is equivalent to

$$[\![\nabla_{q_0}\mathcal{L}(Q), \delta q_0]\!] = -2\frac{E(T)}{E(0)^2}[\![q_0, \delta q_0]\!] + [\![M_\square^{-1}\tilde{q}_0, \delta q_0]\!], \tag{2.29}$$

where $M_\square^{-1}$ is the inverse of the matrix differential operator $M_\square$. The gradient of the Lagrangian with respect to the initial perturbation is then

$$\nabla_{q_0}\mathcal{L}(Q) = -2\frac{E(T)}{E(0)^2}q_0 + M_\square^{-1}\tilde{q}_0, \tag{2.30}$$

and the second optimality condition readily follows:

$$-2\frac{E(T)}{E(0)^2}q_0 + M_\square^{-1}\tilde{q}_0 = 0. \tag{2.31}$$

There remains to calculate the derivative of $\mathcal{L}$ with respect to the direct state variable q. The procedure is straightforward but algebraically involved. Only the final result is given here. At the stationary points of the Lagrangian $\mathcal{L}$, the gradient $\nabla_q\mathcal{L}$ vanishes and the adjoint variables are found, through successive integrations by parts, to satisfy

$$(-1)^{i+1}\frac{\partial^{i+1}(A_i^*\tilde{q})}{\partial y^i \partial t} + (-1)^j\frac{\partial^j(B_j^*\tilde{q})}{\partial y^j} - \alpha^2 M_\square^{-1}q = 0, \tag{2.32}$$

with the adjoint boundary conditions

$$\tilde{v} = \tilde{u} = \frac{\partial\tilde{v}}{\partial y} = 0 \qquad \text{at} \quad y = 0, \infty, \tag{2.33}$$

and the adjoint terminal condition

$$(-1)^i\frac{\partial^i(A_i^*\tilde{q})}{\partial y^i}(T) = \frac{2}{E(0)}M_\square q(T). \tag{2.34}$$

The * superscript applied to a matrix stands for its conjugate transpose. The adjoint system (2.32), (2.33) is similar to the direct system but it is only well-posed if it is integrated backward in time. For a nonzero parameter α, a forcing term involving the direct state vector q appears in equation (2.32).

The above integrations by parts further yield the following expressions for $\tilde{q}_w$ and $\tilde{q}_0$ in terms of the adjoint variable $\tilde{q}$ evaluated at $y = 0$ and $t = 0$:

$$\tilde{q}_w = (-1)^{j-1}\frac{\partial^{j-1}(B_j^*\tilde{q})}{\partial y^{j-1}}(y=0) + (-1)^i\frac{\partial^i(A_i^*\tilde{q})}{\partial y^{i-1}\partial t}(y=0), \tag{2.35a}$$

$$\tilde{q}_0 = (-1)^i\frac{\partial^i(A_i^*\tilde{q})}{\partial y^i}(t=0). \tag{2.35b}$$

Substitution of (2.35a) and (2.35b) into (2.26) and (2.30) leads to the final equations for the gradients with respect to the control variable q_w and the initial perturbation q_0 in terms of the adjoint field $\tilde{q}$:

$$\nabla_{q_w}\mathcal{L}(Q) = l^2 q_w + M_\diamondsuit^{-1}\left((-1)^{j-1}\frac{\partial^{j-1}(B_j^*\tilde{q})}{\partial y^{j-1}}(y=0) + (-1)^i\frac{\partial^i(A_i^*\tilde{q})}{\partial y^{i-1}\partial t}(y=0)\right), \tag{2.36a}$$

$$\nabla_{q_0}\mathcal{L}(Q) = (-1)^i {M_\square}^{-1}\frac{\partial^i(A_i^*\tilde{q})}{\partial y^i}(t=0) - 2\frac{E(T)}{E(0)^2}q_0. \tag{2.36b}$$

The gradients of the Lagrangian with respect to the initial disturbance and with respect to the wall-normal blowing/suction sequence are therefore given as explicit functions of the direct variables q, q_0, q_w and the adjoint field $\tilde{q}$ at $t = 0$. In the constrained subspace Ω_c where equations (2.18b,c) are satisfied, the gradient of the Lagrangian simply reduces to

$$\nabla_{q_0}\mathcal{L}(Q) = \nabla_{q_0}\mathcal{I}(Q), \tag{2.37a}$$

$$\nabla_{q_w}\mathcal{L}(Q) = \nabla_{q_w}\mathcal{I}(Q). \tag{2.37b}$$

The local shape of the objective functional $\mathcal{I}$ is thus the same as the shape of the Lagrangian $\mathcal{L}$ in the constrained space Ω_c. In particular, at the points of Ω_c where the objective functional is maximal or minimal, the gradient $\nabla\mathcal{L}$ of the Lagrangian and the gradient $\nabla\mathcal{I}$ of the objective functional are identically zero. The solutions of the optimization problem thus lie at the stationary points of the Lagrangian.

Knowledge of the gradient of the objective functional for any given value of q_0 and q_w forms the basis of the numerical optimization algorithm. The local direction of steepest ascent/descent of the objective functional with respect to q_0 or q_w is used to iteratively improve upon a guess value q_0^0 or q_w^0: if the optimal perturbation is sought, one has to explore the constrained space 'uphill' along the direction defined by $\nabla_{q_0}\mathcal{I}$; if an optimal control q_w is sought, the minimum of $\mathcal{I}$ is approached by exploring the constrained space 'downhill' along the direction of steepest descent given by $-\nabla_{q_w}\mathcal{I}$.

2.3.4 Optimization procedure

The optimal control procedure is detailed here. The algorithm is based on the gradient information given in the previous section. The control is only applied during the time interval $[0, T_c]$ and the goal is to minimize the objective functional (2.11) with $T = T_c$. The gradient-based optimization algorithm to minimize $\mathcal{I}$ improves iteratively the wall-blowing sequence q_w^k at each iteration k, by modifying it along a well-chosen direction of descent $\nabla_{desc}^k \mathcal{I}$.

The simplest choice is to proceed along the gradient of $\mathcal{I}$, by using $\nabla_{desc}^k \mathcal{I} = -\nabla_{q_w}^k \mathcal{I}$; this direction should lead, at least locally, to the strongest decrease in the objective functional. The drawback of such a steepest descent technique is that the information used is only local, even though, after a few iterations, a more global picture of the objective functional emerges. Conjugate gradient techniques, which take into account the directions of descent evaluated in previous steps (Greenbaum (1997)), typically increase the convergence rate of the algorithm at a very low additional computational cost; in many cases they are necessary to ensure convergence of the procedure. The optimization algorithm is summarized in Table 2.2.

2.4 Application to swept Hiemenz flow and numerical implementation

By gathering the results of the previous section, the adjoint system associated to the direct system (2.8)-(2.10) may be written as:

$$\tilde{A}\frac{\partial}{\partial t}\begin{bmatrix}\tilde{v}\\ \tilde{u}\end{bmatrix} + \tilde{B}\begin{bmatrix}\tilde{v}\\ \tilde{u}\end{bmatrix} - \frac{\alpha^2}{2}M_{\square}^{-1}\begin{bmatrix}v\\ u\end{bmatrix} = 0, \tag{2.38}$$

where the adjoint operators $\tilde{A}$ and $\tilde{B}$ are

$$\tilde{A} = \begin{bmatrix}\Delta & 0\\ 0 & 1\end{bmatrix}, \tag{2.39a}$$

$$\tilde{B} = \begin{bmatrix} (-F\frac{\partial}{\partial y} + \Delta + ikReW)\Delta \\ \quad - 2F'\frac{\partial^2}{\partial y^2} + 2(ikReW' - F'')\frac{\partial}{\partial y} & -F'' \\ -2F'\frac{\partial}{\partial y} & (-F\frac{\partial}{\partial y} + \Delta + ikReW - 3F') \end{bmatrix}, \tag{2.39b}$$

- **1. Start from a guess value $q_w^0(t)$ for the temporal evolution of the blowing/suction velocity**
  'No blowing' is an acceptable guess value for the control since it is compatible with the wall-normal velocity boundary condition for the initial perturbation.

- **2. Solve the direct problem (2.8)-(2.10)**
  Using standard numerical techniques the direct problem is solved forward in time from $t = 0$ to $t = T_c$ with initial condition $q_0(y)$ and wall boundary condition $q_w^k(t)$ for the $(k+1)^{th}$ optimization step.

- **3. Compute the terminal condition $\tilde{q}^k(T_c)$ for the adjoint field using equation (2.34)**
  Solving (2.34) requires the integration of an ordinary differential equation subject to the adjoint boundary conditions (2.33).

- **4. Solve the adjoint problem (2.32)-(2.33)**
  The adjoint problem has to be solved backward in time from $t = T_c$ to $t = 0$ starting with the terminal value $\tilde{q}^k(T_c)$ from step **3**.

- **5. Compute the gradient of the objective functional with respect to the control variable q_w using equation (2.34a)**
  Solving equation (2.34a) is simplified by our choice of the operator $M_{\Diamond}^{-1}$.

- **6. Compute the direction of descent**
  The direction of descent $\nabla_{desc}^k \mathcal{I}$ is based on the gradient of the objective functional computed in step **5**. A conjugate gradient method is used to determine the direction of descent.

- **7. Change $q_w^k(t)$ into $q_w^{k+1}(t) = q_w^k(t) + s^k \nabla_{desc}^k \mathcal{I}$**
  The previous estimate $q_w^k(t)$ is improved by stepping in the direction of descent computed in step **6**. The amount of correction, given by s^k, is determined by a line search algorithm (Press *et al.* 1992) which computes $s^k > 0$ so that $\mathcal{I}(q_w^k(t) + s^k \nabla_{desc}^k \mathcal{I})$ reaches a minimum with respect to s^k.

- **8. Return to step 2 and iterate until converged.**

Table 2.2: Structure of the optimization algorithm for the optimal control problem.

with adjoint boundary conditions (2.33). According to (2.34), the terminal condition of the adjoint system is related to the terminal value of the direct state vector via

$$\tilde{q}(y,T) = \frac{-1}{E(0)} A^{-1} M_{\square} q(T). \tag{2.40}$$

The operators A and $M_{\square}$ are given in (2.9a) and (2.14), respectively. The boundary conditions (2.33) are needed to invert the second-order operator A, in order to compute $\tilde{q}(y,T)$ from (2.40).

The gradients of the objective functional with respect to the control variable, $\nabla_{q_w}\mathcal{I}$, and with respect to the initial perturbations, $\nabla_{q_0}\mathcal{I}$, defined in (2.37) and given by (2.36) become

$$\nabla_{q_w}\mathcal{I} = l^2 q_w + M_{\diamondsuit}^{-1}\left(\frac{\partial^3}{\partial y^3} - F\frac{\partial^2}{\partial y^2}\right)\tilde{q}(y=0,t), \tag{2.41a}$$

$$\nabla_{q_0}\mathcal{I} = {M_{\square}}^{-1} A\ \tilde{q}(y,t=0) - \frac{E(T)}{E(0)^2} q_0, \tag{2.41b}$$

where the operator $M_{\diamondsuit}$ is given in (2.15). The 'numerical difficulties' alluded to in section 2.3.1 which resulted in the introduction of the switch function $s_{\diamondsuit}$ now become clear. The initial disturbance $q(t=0)$ on which control is applied is computed under the assumption of zero wall-normal velocity at the wall. Since no boundary condition at the wall is imposed on the higher derivatives of the adjoint field $\tilde{q}$, the gradient $\nabla^k_{q_w}\mathcal{I}$ may not vanish at $t=0$. Thus the wall-blowing sequence q_w^k computed at optimization step k, augmented by a fraction of the gradient $s^k\nabla^k_{q_w}\mathcal{I}$, may not satisfy the homogeneous wall condition at $t=0$. Similarly, at $t=T_c$ the adjoint terminal condition is computed from the direct terminal condition and its spatial derivatives up to second order. If the wall-normal velocity v_w or its derivatives do not vanish at the end of the temporal control interval, the terminal condition for the adjoint problem may not satisfy the boundary condition $\tilde{v}(y=0,T_c)=0$. The scalar switch function $s_{\diamondsuit}(t)$ introduced in section 2.3.1 allows a smooth introduction and fading of the wall-normal control velocity v_w at both ends of the control time interval. The control effort at $t=0$ and $t=T_c$ is brought to zero and any mismatch in the boundary conditions is avoided.

Spatial derivatives have been computed by using a pseudospectral method based on Chebyshev polynomials with a rational function mapping that allows a flexible placement of collocation points within the boundary layer and in the free stream. The temporal evolution is accomplished by a second-order backward-differentiation scheme, after time has been rescaled by k.

In step **6** of the optimization scheme (Table 2.2), the Polak-Ribière conjugate gradient algorithm is implemented to compute the direction of descent. This is followed in step **7** by a line search algorithm based on Brent's method for the computation of optimal perturbations as well as optimal control. The reader is referred to Press *et al.* (1992) for a detailed description of these computational techniques.

In order to generate grid-independent results, it was sufficient to use 150 collocation points in the wall-normal direction and a time step $\Delta t = 0.1$. In the majority of computations presented here it took less than five iterations of the conjugate gradient algorithm to converge to an optimum for both the optimal control and optimal perturbation problems, with the first step often coming to within 5% of the optimal value of the objective functional.

2.5 Optimal perturbations

In their study of non-modal effects in swept Hiemenz flow, Obrist and Schmid (2003b) present several computations at a Reynolds number $Re = 550$ and a spanwise wavenumber $k = 0.25$. Their approach is based on an eigenfunction expansion of the linear initial value problem. With these parameter settings the flow is found to be asymptotically stable but susceptible to short-term energy growth. Computations have been performed at the same parameter settings, but additional results are also presented at a Reynolds number $Re = 850$ where the flow is linearly unstable. Even higher Reynolds numbers ($Re = 2000$) have also been investigated to probe the physical mechanisms responsible for transient energy amplification, which was found to take place throughout the parameter range under consideration ($100 \leq Re \leq 2500, 0.05 \leq k \leq 0.45$).

2.5.1 Energy amplification

The optimal perturbation is defined as the initial disturbance exhibiting the largest energy amplification over a given time interval. Minor modifications to the algorithm outlined in Table 2.2 — i.e. setting $q_w = 0$ (no blowing/suction), using q_0 as the control variable and $\nabla_{q_0}\mathcal{I}$ as the associated objective functional gradient — yield a fast and efficient algorithm to determine both the maximum energy amplification and the initial condition that produces it.

In Figure 2.2a the temporal energy evolution of such initial perturbations for the case of a linearly stable (solid line) or unstable (dashed line) basic flow is displayed. In the linearly stable case ($Re = 550$, $k = 0.25$), transient energy growth amounts to 123 times the initial energy before perturbations eventually decay. In the unstable

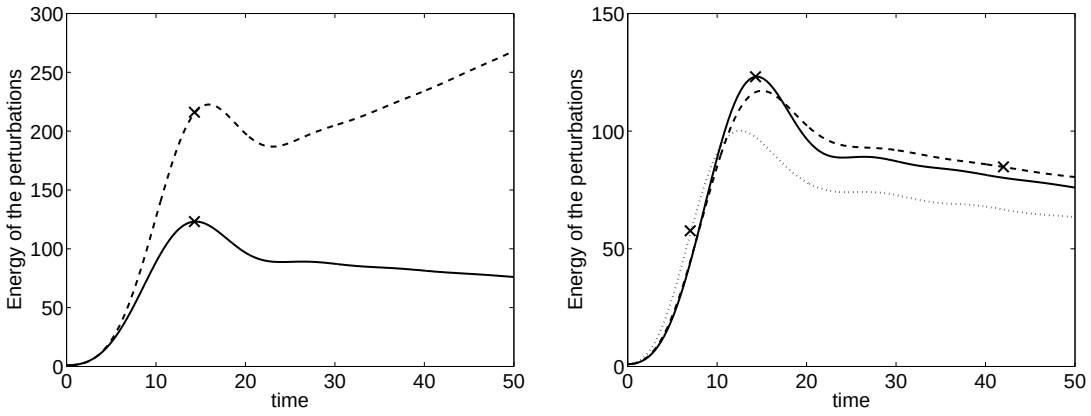

(a) (b)

Figure 2.2: (a) Disturbance energy E versus time for optimal perturbations in the linearly stable parameter régime ($Re = 550$, $k = 0.25$, solid line), and in the linearly unstable parameter régime ($Re = 850$, $k = 0.25$, dashed line). The optimization time has been set to $T_p = 14.3$ (cross). (b) Disturbance energy versus time for the initial perturbations which yield the maximum energy growth at time $T_p = 5$ (dotted line), $T_p = 14.3$ (solid line), and $T_p = 42$ (dashed line). The respective optimization times are indicated by a cross. The parameters have been chosen as $Re = 550$, $k = 0.25$.

case ($Re = 850$, $k = 0.25$), high energy levels may be reached significantly earlier than would be possible by a purely exponential growth of the unstable eigenmode only. The time required to amplify the initial energy by a factor 220 is only 15 time units which should be compared to the 200 time units required to amplify the energy of the most unstable mode by the same amount.

Figure 2.2b illustrates how the optimization time T_p influences the energy evolution of the optimal perturbations. At a Reynolds number $Re = 550$ and spanwise wavenumber $k = 0.25$, the maximum energy amplification can be achieved by setting the optimization time to $T_p = 14.3$ (solid line). The energy at $t = T_p$ is then 123 times the initial energy. Optimal perturbations for shorter optimization times, e.g. $T_p = 5$, are slightly more amplified initially. Their overall amplification, however, is lower than for the case $T_p = 14.3$. Beyond a specific value of the optimization time, the least stable mode (or the most unstable mode in the linearly unstable parameter régime) prevails. Any optimization time larger than $T_p = 25$ results in a very similar optimal initial condition — the one that excites the least stable mode most efficiently during the early stages of the energy amplification.

Surprisingly, large-time optimal perturbations reach nearly the same maximum

amplification, at nearly the same time, as the one found for $T_p = 14.3$. Several computations performed at Reynolds numbers ranging from $Re = 500$ to $Re = 2000$ and spanwise wavenumbers ranging from $k = 0.05$ to $k = 0.4$ have confirmed this property. The initial condition yielding the maximum energy at large times can be identified as the adjoint of the least stable mode (Hill 1995). The overall optimal perturbation thus differs only insignificantly from the adjoint of the least stable mode.

2.5.2 Parameter study

The initial disturbance leading to the maximum energy amplification E_{max}, regardless of the time T_{max} when it is reached, has been computed for several Reynolds numbers and spanwise wavenumbers. In practice this overall optimal perturbation has been obtained by bracketing the time T_{max} when the maximum energy amplification is reached for different T_p. Figure 2.3a displays isocontours of the maximum energy achieved by overall optimal perturbations; the corresponding time T_{max} is shown in Figure 2.3b. In both figures, the thick solid line represents the neutral stability curve for swept Hiemenz flow. At low Reynolds numbers or spanwise wavenumbers the optimal perturbation could not be determined satisfactorily due to numerical difficulties in evaluating the gradient of the objective function. No gain curves could therefore be obtained in the range $kRe \lesssim 100$. The blank area inside the neutral stability curve identifies the parameter régime where the energy of the optimal perturbation grows monotonically and thus does not exhibit a transient maximum.

We observe that the energy amplification increases with Reynolds number but decreases when the spanwise wavenumber is increased. The time at which the maximum amplification is reached increases both with Reynolds number and spanwise wavenumber. Energy amplifications ranging from 50 times (for $Re \approx 300, 0.2 \lesssim k \lesssim 0.4$) up to 1500 times the initial energy (for $Re \approx 2500, k \approx 0.1$) have been obtained. At low Reynolds numbers the energy amplification is nearly independent of the spanwise wavenumber; as the Reynolds number increases, however, low-wavenumber perturbations clearly outperform higher-wavenumber disturbances.

At Reynolds numbers higher than 500, two distinct behaviors of the maximum energy amplification with respect to the spanwise wavenumber may be distinguished, as illustrated in Figure 2.4a. At small spanwise wavenumbers the maximum energy amplification decreases slowly with spanwise wavenumber k while at higher spanwise wavenumbers the maximum energy amplification decreases strongly. The data closely match cubic (at low spanwise wavenumber k) and quadratic (at high k) fit-

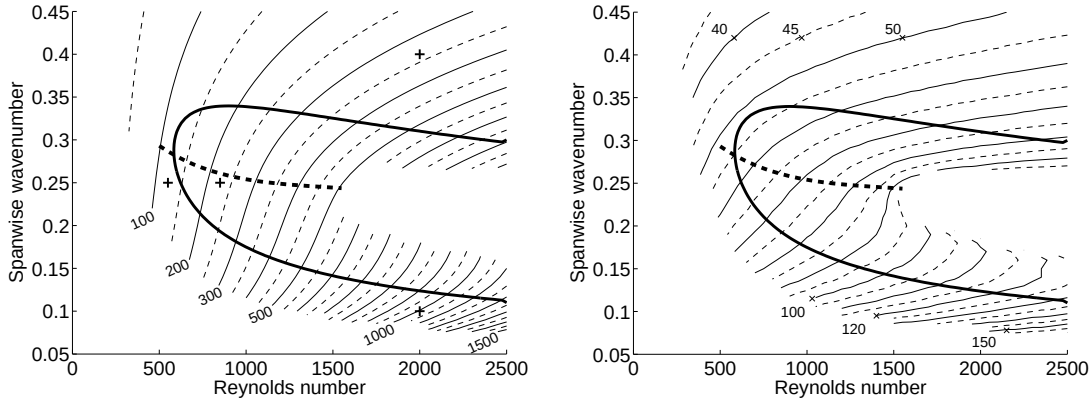

(a) (b)

Figure 2.3: (a) Isocontours of the maximum energy amplification E_{max} achieved by optimal perturbations (thin lines) in the (Re, k)-plane. The '+' signs denote the parameter values $(Re, k) = (550, 0.25)$, $(850, 0.25)$, $(2000, 0.1)$ and $(2000, 0.4)$ where most of the calculations have been performed. (b) Isocontours of the time T_{max}/k when the maximum energy is reached by optimal perturbations (thin lines) in the (Re, k)-plane. In both figures, the thick solid line represents the neutral stability boundary, and the thick dashed curve is the dividing line separating the two amplification mechanisms discussed in section 2.5.

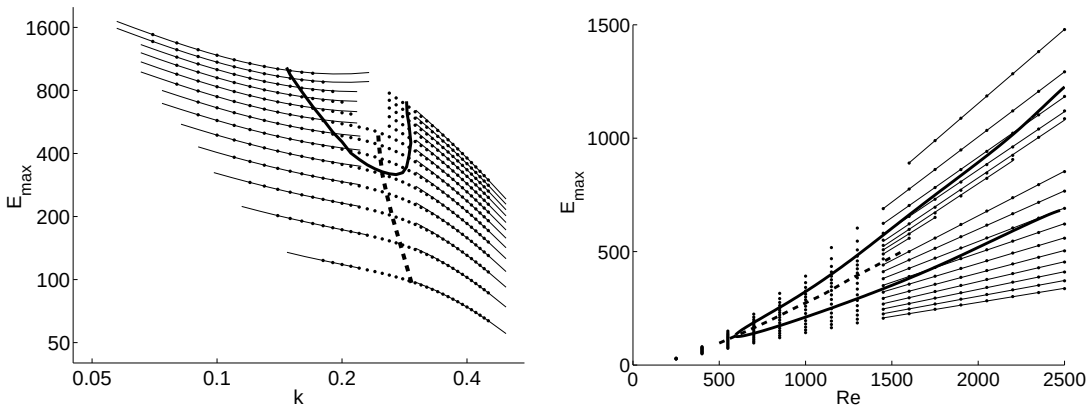

(a) (b)

Figure 2.4: (a) Maximum energy amplification $E_{\max}$ of optimal perturbations versus k for Reynolds numbers ranging from $Re = 500$ (lowest curve) to $Re = 2450$ (highest curve). The scale is logarithmic on both axes. The maximum energy amplification E_{max} decreases slowly with k at small spanwise wavenumbers and strongly with k at high wavenumbers. To guide the eye, least-squares curve fits are displayed by thin solid lines: the data follow a cubic and a quadratic fit at low and high wavenumbers, respectively. The thick dashed line located at $k \sim 0.25$ delineates the two scaling behaviors and the thick solid line represents the neutral stability boundary. (b) Maximum energy amplification $E_{\max}$ of optimal perturbations versus Reynolds number for spanwise wavenumbers ranging from $k = 0.08$ (highest curve) to $k = 0.44$ (lowest curve). The maximum energy amplification $E_{\max}$ increases linearly with the Reynolds number above $Re = 1000$ (thin solid lines). The low and high-k behaviours are delimited by the thick dashed line, and the thick solid line represents the neutral stability boundary.

ting curves indicated by thin solid lines. Along the thick dashed line at $k \sim 0.25$ both fits are equally close to the data, which reveals a change in the flow behavior as one proceeds from low to high wavenumbers. In both cases the maximum energy amplification exhibits a linear dependence with respect to the Reynolds number as shown in Figure 2.4b.

The thick dashed line in Figure 2.4a has been represented in Figure 2.4b and Figure 2.3a,b to delineate the high- and low-k parameter régimes. Two distinct physical mechanisms responsible for the energy amplification are suspected to entail the different scalings with the spanwise wavenumber, as further investigated in section 2.5.4.

Comparison with results from eigenfunction expansions

A similar parameter study based on an eigenfunction expansion analysis has been performed by Obrist and Schmid (2003b) in their Figure 3. The maximum energy growth obtained by linear combinations of eigenfunctions from the discrete spectrum, denoted G_{max} to distinguish it from E_{max}, is then shown to range from 0 to about 100 as the Reynolds number and spanwise wavenumber vary from 0 to 2500 and from 0.05 to 0.45, respectively. The energy growth G_{max} is found to increase strongly with Reynolds number but shows little dependence on the spanwise wavenumber at small Reynolds numbers. At higher Reynolds numbers, G_{max} decreases as k tends to 0 or 0.45 with its maximum located inside the neutral curve.

The parameter study by Obrist and Schmid (2003b) has the disadvantage of neglecting the continuous part of the spectrum which has a strong quantitative effect on transient growth in swept Hiemenz flow. It is thus not surprising that the energy growth G_{max} computed by an expansion in discrete eigenmodes is up to two orders of magnitude lower than the maximum energy E_{max} calculated by using the present adjoint method. There is also disagreement as to the behavior of E_{max} at high Reynolds numbers and low spanwise wavenumbers.

Obrist and Schmid (2003a) show that the discrete part of the spectrum consists of three branches, two of which have eigenmodes with a strong wall-normal velocity component. Eigenmodes from the continuous spectrum show no specific prevalence of any velocity component. The computation of the optimal purely wall-normal velocity perturbation might thus give an insight into the role of the v-dominant branches of the discrete spectrum in the transient growth process. To this end, the $[.,.]$ scalar product has to be redefined as

$$[q_1, q_2] = \int_0^\infty v_1^*.v_2 \; dy + c.c., \tag{2.42}$$

and a purely wall-normal initial guess $q_0^0 = (v_0^0, 0)^T$ has to be used.

The resulting optimal perturbations then display energy amplifications in agreement with Obrist and Schmid (2003b), ranging from less than 1 at low Reynolds numbers to around 10^2 at $Re = 2500$. The spanwise-wavenumber dependence is also recovered, displaying little influence of the wavenumber at low Reynolds numbers; moreover, E_{max} decreases as k tends to 0 or 0.45.

The purely chordwise optimal velocity perturbation has also been computed, but no transient growth could be found. A comparison of these results and the observations of Obrist & Scmid (2003b) suggests that (i) the eigenmodes of the two v-dominant branches of the discrete spectrum are the only modes responsible for transient growth, (ii) the u-dominant continuous modes play a merely catalytic role in transient energy growth with a more pronounced efficiency at high Re and low k.

2.5.3 Energy transfer analysis

It is both instructive and straightforward to analyze the flow of energy between various perturbation components in the transient energy growth process. New insight into the dominant terms may lead to a model of the physical mechanism responsible for the observed perturbation dynamics.

By multiplying each of the disturbance equations (2.6a)-(2.6c) by the appropriate velocity component and subsequently adding the three equations, one obtains a temporal evolution equation for the local kinetic energy density $e = u^2 + v^2 + w^2$ of the perturbation, namely,

$$\begin{aligned} \frac{\partial e}{\partial t} &= Fu\frac{\partial u}{\partial y} + u\Delta u - ReWu\frac{\partial u}{\partial z} - 2F'u^2 - F''uv \\ &\quad + Fv\frac{\partial v}{\partial y} + v\Delta v - ReWv\frac{\partial v}{\partial z} + F'v^2 - v\frac{\partial p}{\partial y} \\ &\quad + Fw\frac{\partial w}{\partial y} + w\Delta w - ReWw\frac{\partial w}{\partial z} - ReW'wv - w\frac{\partial p}{\partial z}. \end{aligned} \tag{2.43}$$

During the transient energy growth phase, terms involving the chordwise velocity component u as well as all pressure gradient terms are found to be negligible compared to the remaining components. The above energy balance may thus be reduced to an equation involving only eight essential terms on the right hand side:

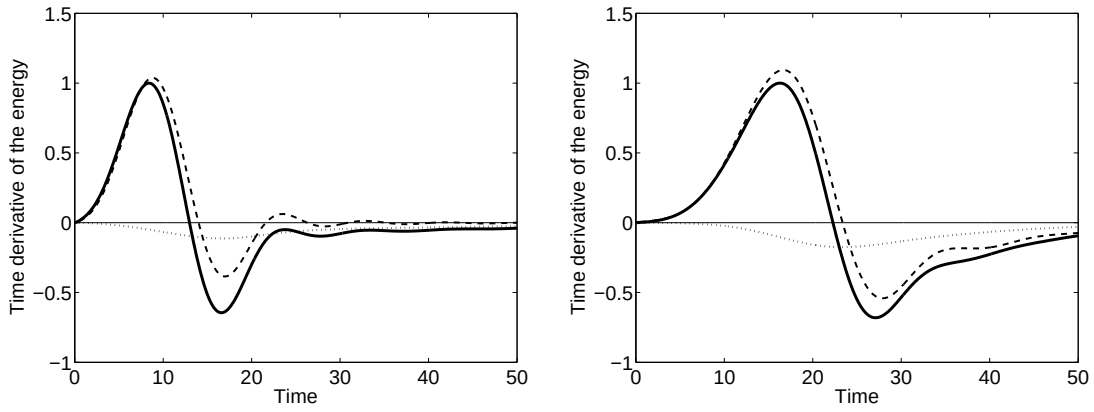

(a) (b)

Figure 2.5: Temporal evolution of the dominant terms in the energy equation (2.44) for optimal perturbations, integrated over the (y, z)-plane and normalized with respect to the maximum time derivative of the energy. The production term $-ReW'wv$ (dashed line) is responsible for most of the energy amplification (solid line). The dissipation term $w\Delta w$ is displayed as a dotted line. Parameter settings are (a) $Re = 2000, k = 0.1, T_p = 12.9$ and (b) $Re = 2000, k = 0.4, T_p = 22.2$.

$$\begin{aligned}\frac{\partial e}{\partial t} \approx\ & Fv\frac{\partial v}{\partial y} + v\Delta v - ReWv\frac{\partial v}{\partial z} + F'v^2 \\ & + Fw\frac{\partial w}{\partial y} + w\Delta w - ReWw\frac{\partial w}{\partial z} - ReW'wv. \end{aligned} \tag{2.44}$$

Integrating each term of equation (2.44) separately over the computational (y, z)-domain reveals that the production term $(-ReW'wv)$ clearly dominates at small times (Figure 2.5). At large times, the linear stability property of the flow determines the dominant term in equation (2.44). For linearly stable configurations, the viscous term $w\Delta w$ dominates, thus damping the perturbations. For linearly unstable configurations, the viscous term $w\Delta w$ remains below the production term $(-ReW'wv)$, and, as a consequence, perturbations grow exponentially. Since the dominant production term during the early stage has been identified as $(-ReW'wv)$, the mechanism responsible for transient growth is suspected to be inviscid and two-dimensional in the $(y - z)$-plane.

The contour plot of $\int_{2\pi/k} \frac{\partial e}{\partial t} dz$ in the (t, y)-plane (Figure 2.6a) indicates that at low wavenumbers (the case $k = 0.1$ is displayed), energy is amplified in an area located at roughly one third of the boundary layer thickness from the wall. The

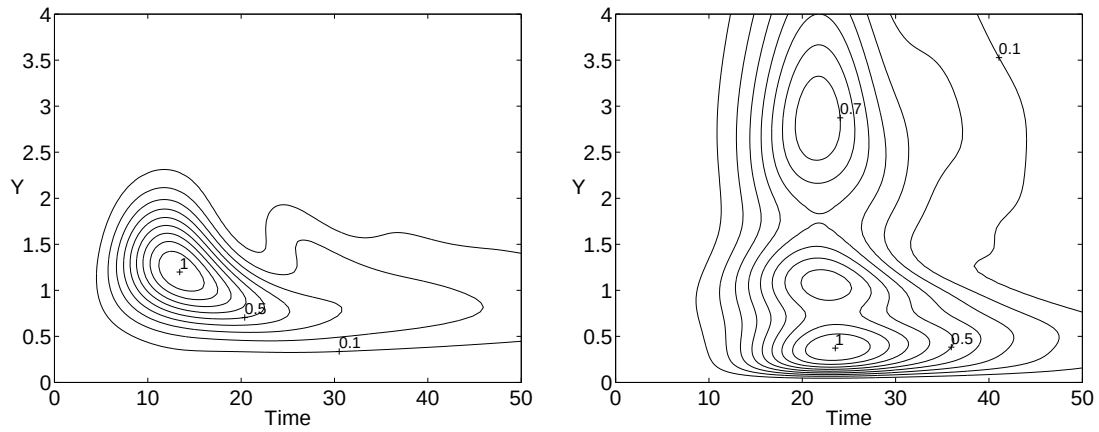

Figure 2.6: Isocontours of $\int_{2\pi/k} \frac{\partial e}{\partial t}\, dz$ (normalized with respect to its maximum) in the (t, y) plane for optimal perturbations. At low wavenumbers (a), energy production is localized and occurs at a distance of about one third of the boundary layer thickness from the wall. At high wavenumbers (b), energy production occurs over a wider area and farther away from the wall. Parameter settings are (a) $Re = 2000, k = 0.1, T_p = 12.9$ and (b) $Re = 2000, k = 0.4, T_p = 22.2$.

strongest energy amplification rate (contour level labelled $'1'$) occurs at $t = 13.9$, that is, shortly after the perturbation has reached its maximum energy growth ($T_{max} = 13.6$ for $Re = 2000$, $k = 0.1$). At high wavenumbers, disturbance energy production is less localized (Figure 2.6b); it is also less intense. Two local maxima appear, one close to the wall ($y \approx 0.5$) and a weaker one located at the outer edge of the boundary layer ($y \approx 3$). Again, the most intense energy amplification rate is found at $t = 25.6$, that is, shortly after the perturbation has reached its maximum energy growth ($T_{max} = 25.5$). In contrast to the low-wavenumber case, where the entire energy amplification mechanism is confined inside the boundary layer, a significant amount of energy is produced in the outer flow.

2.5.4 Physical mechanisms leading to transient energy growth

Both the k-dependence of the maximum energy amplification displayed in figure 2.4 and the location of maximum energy transfer from the basic flow to the perturbation at low or high wavenumbers, imply the existence of two distinct physical mechanisms at work.

Solutions of the linear initial value problem provide further support for this

proposition. Figures 2.7 and 2.8 show the temporal evolution of optimal perturbations at $Re = 2000$ for a representative low ($k = 0.1$) and high ($k = 0.4$) spanwise wavenumber, respectively. Snapshots of the chordwise vorticity and spanwise velocity fields in the ($x = 0$)-plane have been displayed at $t = 0$, $T_{max}/3$, $2T_{max}/3$, T_{max}, $4T_{max}/3$ (from top to bottom). The color scheme and contour scales are the same in both figures and for all snapshots, thus aiding in the quantitative comparison between the low and high spanwise wavenumber régimes. For any Reynolds number and spanwise wavenumber, the optimal perturbation resembles a distribution of elongated chordwise vorticity patches inclined against the sweep z-direction as displayed in Figures 2.7a and 2.8a. The vorticity patches are advected by the sweep velocity W and propagate from left to right between two consecutive snapshots. Under the influence of the basic shear they tilt up in a manner reminiscent of the Orr mechanism (Figures 2.7a,b and 2.8a,b): the vorticity distribution initially inclined against the shear is compressed, thereby inducing transient energy growth (Haynes (1987), Vanneste (1999)).

In the case of low spanwise wavenumber $k = 0.1$ (Figure 2.7), the chordwise vortices are distorted until rectangular vortical cells appear (Figure 2.7c). As the 'heads' of the chordwise vortices of one sign pass above the 'feet' of the vortices of the opposite sign, a two-layered array of counter-rotating vortices forms (Figure 2.7c). This dipole structure is aligned parallel to the wall at a distance of roughly one third of the boundary layer thickness. This region is therefore characterized by strong spanwise velocity excesses and deficits; for example, as the upper-layer vortex of a specific dipole rotates counterclockwise (displayed by solid vorticity contours in Figure 2.7), the center of the dipole produces a region of strong spanwise excess velocity (displayed in red). Interestingly, the dipole structure forms at the time when $\int_{1/k} \frac{\partial e}{\partial t} dz$ reaches a maximum (Figure 2.5a) and it is located at the wall distance where the disturbance energy density is amplified the most according to Figure 2.6a.

Two mechanisms of transient growth are therefore operating at low spanwise wavenumbers: the Orr mechanism via the tilting of the initial vorticity distribution by the basic shear on the one hand and vortex dipole-induced spanwise velocities on the other, the latter being dominant. In the final stage, the rectangular cells split and rearrange — with the 'head' of each vortex merging with the 'foot' of the neighboring upstream vortex of equal orientation. This event, which is incidental to the transient growth process, occurs at approximately $t = \frac{2}{3} T_{\max}$ (Figures 2.7c,d).

The evolution of chordwise vortices at higher spanwise wavenumbers displays a different scenario. Most significantly, even if the vortices are still heavily distorted, rectangular vortical dipoles are no longer prominent (Figure 2.8). The vorticity distribution initially inclined against the shear is still tilted by the spanwise shear and the energy amplification mainly arises from the Orr mechanism, as illustrated by the

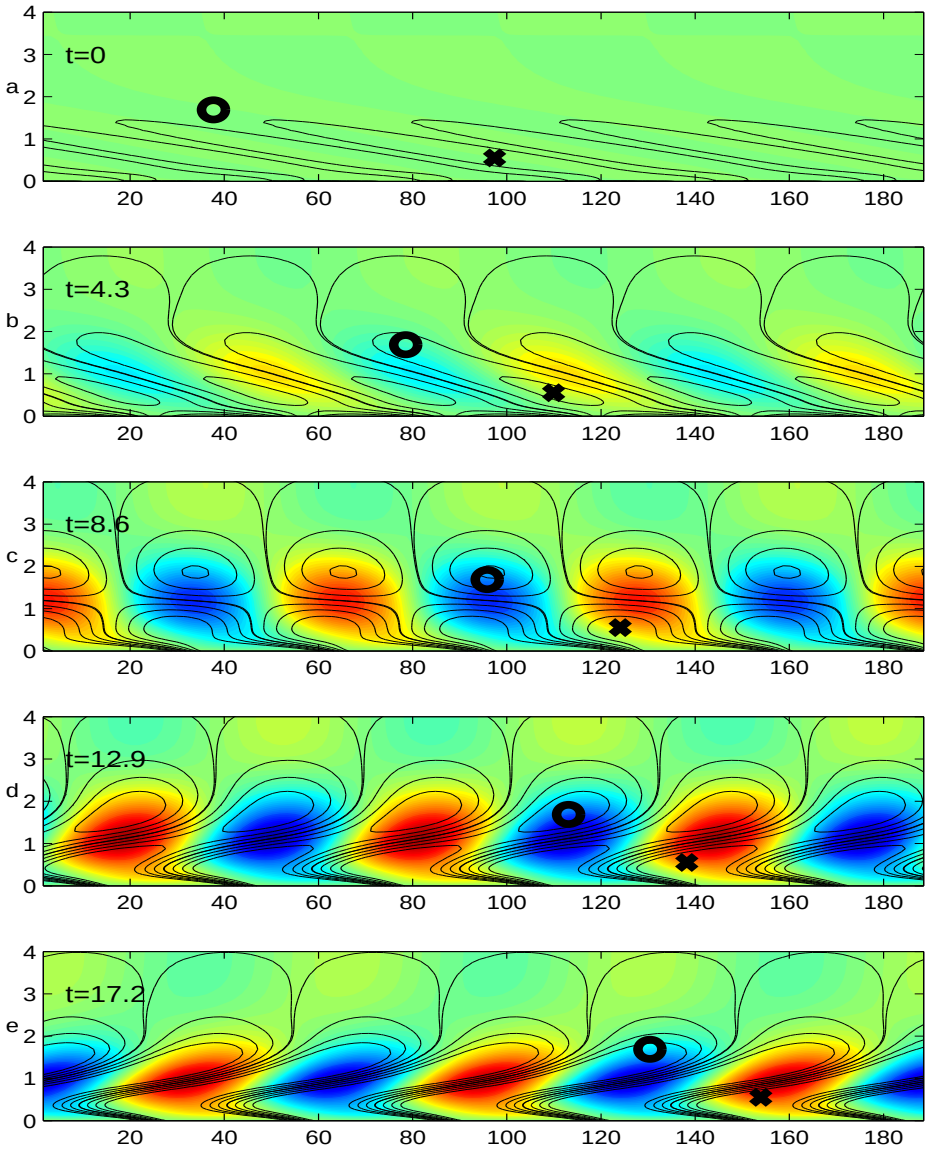

Figure 2.7: Time evolution of the overall optimal perturbation displayed in snapshots of the perturbation field in the (z, y)-plane over three spanwise wavelengths at $t = 0$, $\frac{1}{3}T_{max}$, $\frac{2}{3}T_{max}$, T_{max}, $\frac{4}{3}T_{max}$ (from top to bottom). The sweep W is from left to right. Isocontours of the chordwise vorticity are displayed in solid (positive vorticity) and dashed lines (negative vorticity). The spanwise velocity amplitude w of the disturbance is displayed in color (red: positive, blue: negative). Symbols have been added to aid the reader in tracking the features of the evolving vortices. The time of maximum energy is $T_{max} = 12.9$ and the parameters have been set to $Re = 2000$, $k = 0.1$, $T_p = 12.9$.

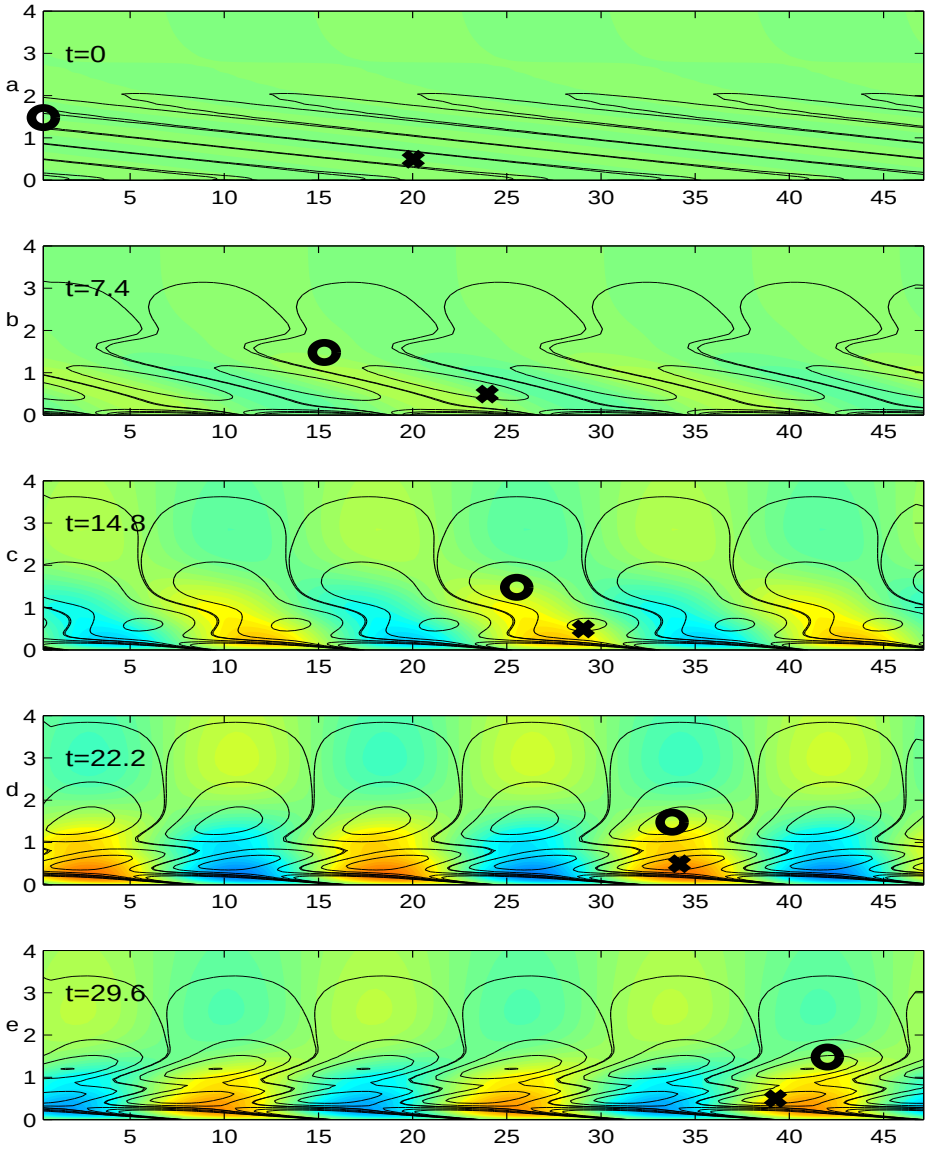

Figure 2.8: Same as in Figure 2.7 for $Re = 2000$, $k = 0.4$ and $T_p = 22.2$; the contour levels and the color map are the same. The time of maximum energy is $T_{max} = 22.2$.

symbols indicating the relative position of the 'head' and 'foot' of the evolving vortex in Figure 2.8. The vortex 'head' overtakes its 'foot', and the disturbance energy reaches a maximum when the vortex is the most compressed, that is, when the 'head' is exactly above the 'foot' (Figure 2.8d). In the later stages, vortex splitting never occurs. To provide additional support for the above scenario, computations were performed at even higher spanwise wavenumbers ($k \geq 0.8$). The Orr-mechanism has been found to be dominant over vortex dipole-induced spanwise velocities in all high wavenumber cases.

Examination of the temporal evolution of disturbances in the linearly unstable region, within the neutral stability boundary of Figure 2.3a, reveals the presence of the same physical mechanisms at low and high spanwise wavenumbers respectively.

2.6 Optimal control

Within the scope of this study control is applied via wall-normal blowing and suction given by the normal velocity $v_w(t)$. The influence of the control time T_c on the energy growth of controlled perturbations is investigated and a parameter study in the (α, l) plane is conducted in order to find the best setting for the control parameters. A physical interpretation of the control mechanisms follows, with particular emphasis on similarities between optimal and constant gain feedback control.

2.6.1 Control of optimal perturbations

In this section the Reynolds number is set to either $Re = 550$ or $Re = 850$ with a fixed spanwise wavenumber $k = 0.25$ in order to address the control of linearly stable or unstable flows. For all computations, the initial state is taken as the optimal perturbation for $T_p = 14.3$, and wall-blowing or -suction is applied between $t = 0$ and $t = T_c$.

To investigate the influence of the control time T_c, the control parameters α and l in the objective functional (2.11) have been set equal to $\alpha = 0.5$, $l = 1$. As will be shown later, such moderate values of α and l lead to satisfactory control strategies.

The control efficiency depends strongly on the control time T_c. The natural choice is to set T_c close to the time at which the uncontrolled optimal perturbation reaches an energy maximum. For a spanwise wavenumber $k = 0.25$ and a Reynolds number $Re = 550$ (Figure 2.9a), it amounts to setting $T_c = 14.3$ (diamond). In this case the optimal wall-normal blowing and suction sequence decreases the energy

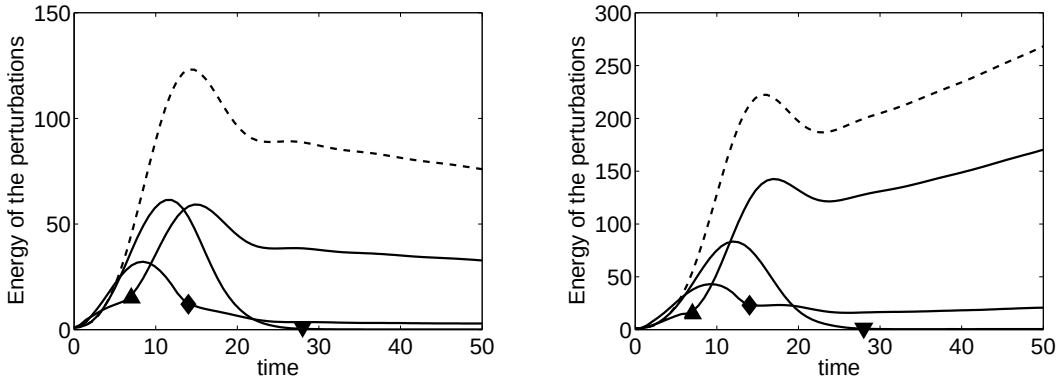

(a) (b)

Figure 2.9: (a) Disturbance energy E as a function of time for linearly stable (a) or unstable (b) flow. The dashed line shows the uncontrolled optimal perturbation computed with $T_p = 14.3$. The solid lines display the energy of the same perturbation when control is applied from $t = 0$ to $T_c = 7$ (upper triangle), $T_c = 14.3$ (diamond), $T_c = 28$ (lower triangle). The remaining parameters have been set to $Re = 550$ (a) and $Re = 850$ (b), $k = 0.25$, $\alpha = 0.5$, $l = 1$.

maximum to 75% of its initial value, while the energy at time T_c is decreased by one order of magnitude from $E(T_c)/E(0) = 123$ to $E(T_c)/E(0) = 12$.

For lower values of T_c the control is less effective in decreasing the energy amplification since the energy transiently increases shortly after the wall-blowing has terminated. For higher values of T_c the energy amplification can be suppressed even further. For example, by choosing $T_c = 28$, i.e., about twice the time at which the energy maximum is reached, the energy decreases to 0.5 times its initial value between $t = 0$ and $t = T_c$. In this case, however, the energy transiently reaches half the level reached by the uncontrolled optimal perturbation between $t = 0$ and T_c.

Similar conclusions hold in the linearly unstable case at $Re = 850, k = 0.25$ shown in Figure 2.9b. Only the case $Re = 550, k = 0.25$ will be discussed in the following study of the influence of the control parameters.

The objective functional (2.11) penalizes both transient energy amplification between $t = 0$ and T_c via the α weighting parameter and excessive wall-blowing via the l weighting parameter. Figure 2.10 reveals the dependence of the objective functional $\mathcal{I}$ (Figure 2.10a), the energy amplification $E(T_c)/E(0)$ (Figure 2.10b), the mean energy $\dfrac{1}{T_c}\int_0^{T_c} E(t)dt$ (Figure 2.10c) and the control energy $\ll q_w, q_w \gg$

(Figure 2.10d) on the weighting parameters α and l. Note that the view angle may be different for different subfigures to ensure the best perspective on the surface plot.

When both α and l are low, the perturbation energy grows by a few orders of magnitude between $t = 0$ and T_c (Figure 2.10c) due to a very strong input of control energy (Figure 2.10d). The lowest energy amplification is indeed achieved at these parameter settings (Figure 2.10b) where wall-blowing can be arbitrarily strong because of the low penalty applied to the control effort, but the very large transient energy peak (Figure 2.10c) precludes such control strategies for practical applications.

By assigning a moderate cost, either to the mean energy amplification (by setting α between 0.3 and 1) or to the control energy (by setting l between 0.1 and 2), the mean energy and the spent control energy are dramatically lowered (Figure 2.10c,d) with only a small increase in the energy amplification (hardly noticeable in Figure 2.10b). Such moderate values for α and l are located near the 'shoulder' of the objective function in Figure 2.10a, where the thick solid line ($\alpha = 0.5$) crosses the thick dashed line ($l = 1$).

As the control cost l increases along the thick solid line, wall-normal blowing or suction becomes too expensive when compared to the resulting gain in the mean energy or in the energy amplification. Beyond the cut-off value $l_{cut} \sim 2$ the control energy drops precipitously (Figure 2.10d). Since very little energy is dedicated to control, the energy amplification (Figure 2.10b) and the mean energy (Figure 2.10c) are nearly the same as for the uncontrolled optimal perturbation.

The mean energy weight α has little influence on the control strategy besides suppressing high transient energy growth between $t = 0$ and T_c. As α increases along the thick dashed line from $\alpha = 0.5$ to $\alpha = 40$ the energy amplification $E(T_c)/E(0)$ remains unchanged (Figure 2.10b). When α is very high ($\alpha \sim 40$) the mean energy $\frac{1}{T_c}\int_0^{T_c} E(t)dt$ decreases only slightly (Figure 2.10c), the dependence on l, however, is much stronger. Since the mean energy is almost constant with respect to α along the thick dashed line, the objective functional (Figure 2.10a) grows nearly quadratically at large α, owing to its dominant term $\frac{\alpha^2}{2}\frac{1}{T_c}\int_0^{T_c} E(t)dt$.

When both α and l are large, the $E(T_c)/E(0)$ term in the objective functional is negligible. In this case, the goal of the optimal control is not so much to damp the energy amplification at $t = T_c$ but rather to decrease the mean perturbation energy between $t = 0$ and T_c while balancing the control energy expenses. Even

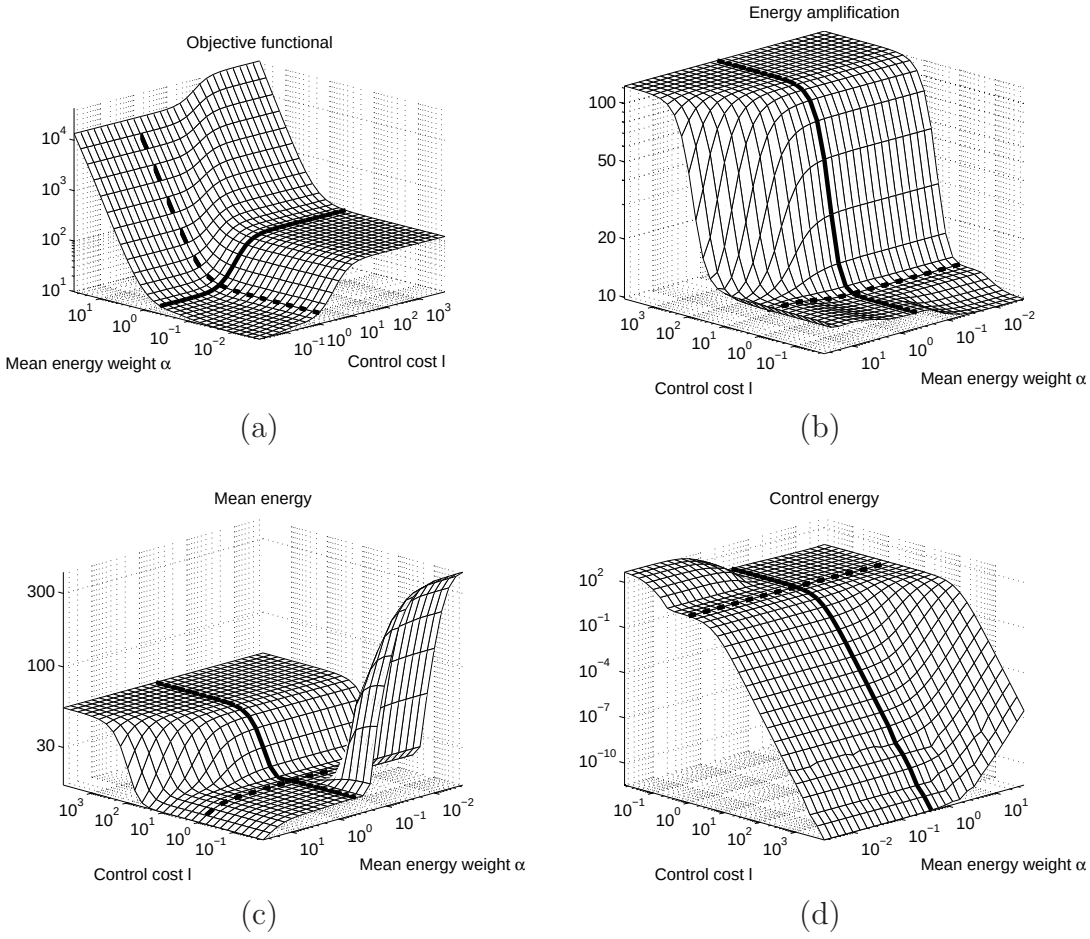

Figure 2.10: Magnitude of the objective functional and its various components as a function of mean energy weight α and control cost l. (a) Objective functional $\mathcal{I}$, (b) Energy amplification $E(T_c)/E(0)$, (c) Mean energy $\dfrac{1}{T_c}\int_0^{T_c} E(t)dt$, (d) Control energy $\ll q_w, q_w \gg$. Along the thick solid line α is equal to 0.5 and along the thick dashed line l is equal to 1. The parameters have been set to $Re = 550$, $k = 0.25$, $T_p = 14.3$, $T_c = 14.3$.

when the control cost parameter l is beyond the cut-off l_{cut}, the cost of transient energy growth between $t = 0$ and T_c may be so high that it is worth blowing at the wall (Figure 2.10d) in order to decrease the mean energy between $t = 0$ and T_c (Figure 2.10c). A decrease in the energy amplification $E(T_c)/E(0)$ (Figure 2.10b) can be observed as a consequence of the overall damping of the energy prior to T_c.

Three régimes are thus delimited by the thick lines in Figure 2.10.

- the case $\alpha \gg 0.5$: the primary goal of our control strategy, which was to damp the energy amplification at a given time $E(T_c)/E(0)$, is overruled by a strong weighting of the mean energy term $\frac{1}{T_c}\int_0^{T_c} E(t)dt$ in the objective functional.
- the case $\alpha \ll 0.5, l \ll 1$: unrealistic amounts of control energy can be spent to damp the energy amplification at time T_c. The resulting energy peaks between $t = 0$ and T_c render such control strategies undesirable.
- the case $\alpha \leq 0.5,\ l \gg 1$: the control is so expensive with respect to the expected gain in the energy amplification that wall-blowing is prohibited. The weak control efforts result in plateaus (Figures 2.10b,c) consistent with the uncontrolled case.

By choosing moderate values of α and l, such as $\alpha = 0.5,\ l = 1$, the energy amplification is efficiently damped with a reasonable amount of wall-normal blowing and suction; these parameter settings may be regarded to deliver both an attractive and realistic control strategy. In what follows, the parameters α and l are set to $\alpha = 0.5$ and $l = 1$, and the manipulation of the underlying physical mechanisms under the corresponding control strategy is investigated.

2.6.2 Physical mechanisms

The effect of optimal control on the dynamics of initial disturbances at $Re = 2000$ is now examined from a physical point of view. Weight parameters have been set equal to $\alpha = 0.5$ and $l = 1$. A parameter study indicates that such values of α and l also yield an efficient control strategy at $Re = 2000$. Snapshots of the evolution of the optimal perturbation, as control is applied, are depicted in Figures 2.11 and 2.12 and should be compared to the corresponding Figures 2.7 and 2.8. A new layer of vortices confined to the wall is detected which travels with the naturally occurring vortices; the latter are observed to tilt more rapidly. In the wavenumber régime where vortex dipoles are not observed naturally (Figure 2.8), vortex dipoles may be introduced by the control (Figure 2.12). For wavenumbers at which vortex dipoles

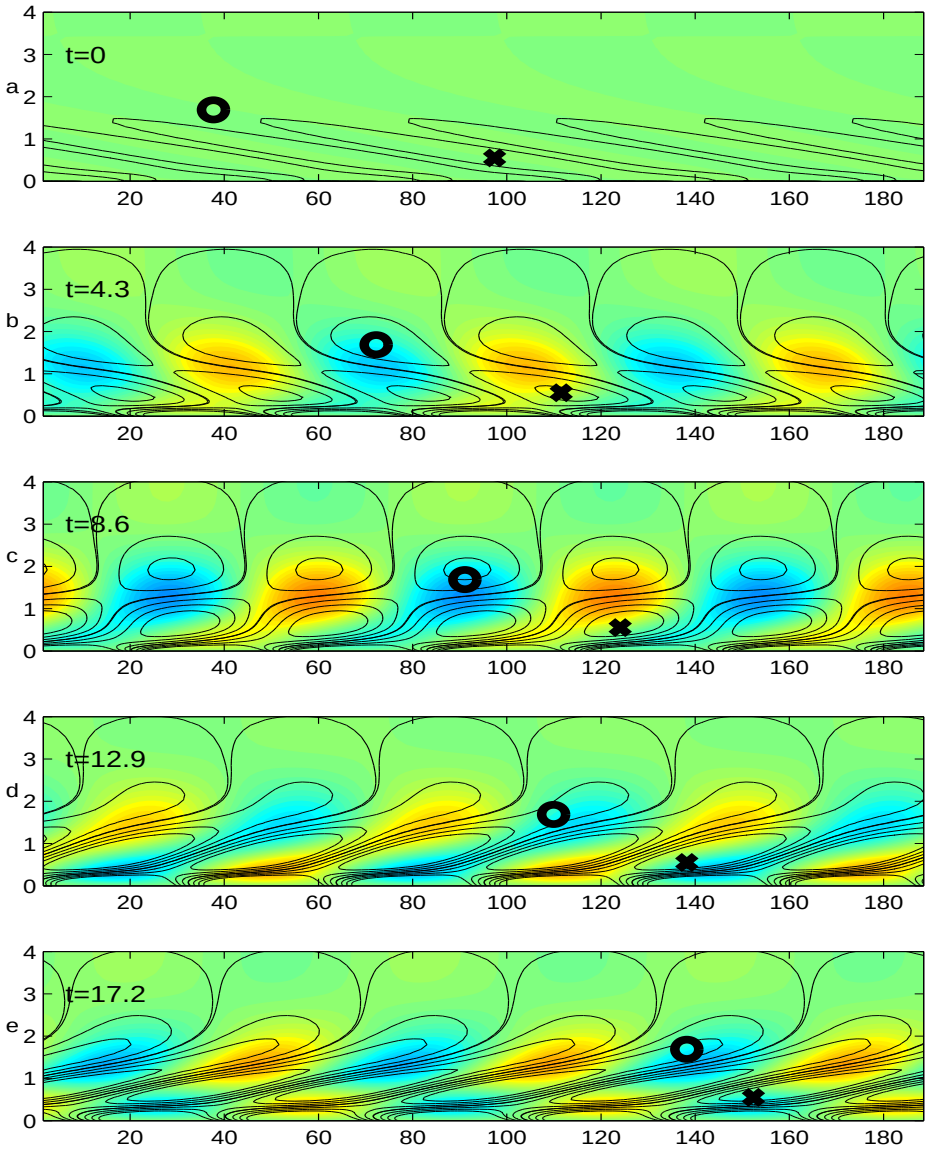

Figure 2.11: Time evolution of the overall optimal perturbation with optimal control applied, displayed in snapshots of the perturbation field in the (z, y)-plane over three spanwise wavelengths, at times $t = 0$, $\frac{1}{3}T_c$, $\frac{2}{3}T_c$, T_c, $\frac{4}{3}T_c$ (from top to bottom). The sweep W is from left to right. The same field variables as in Figure 2.7 are represented and the contour levels and the color map are the same. The optimization time T_c has been set to $T_p = T_{max} = 12.9$ and the other parameters have been set to $Re = 2000$, $k = 0.1$, $\alpha = 0.5$ and $l = 1$. Vortex splitting occurs between b and c, which should be compared to the uncontrolled case in Figure 2.7 when vortices split between c and d.

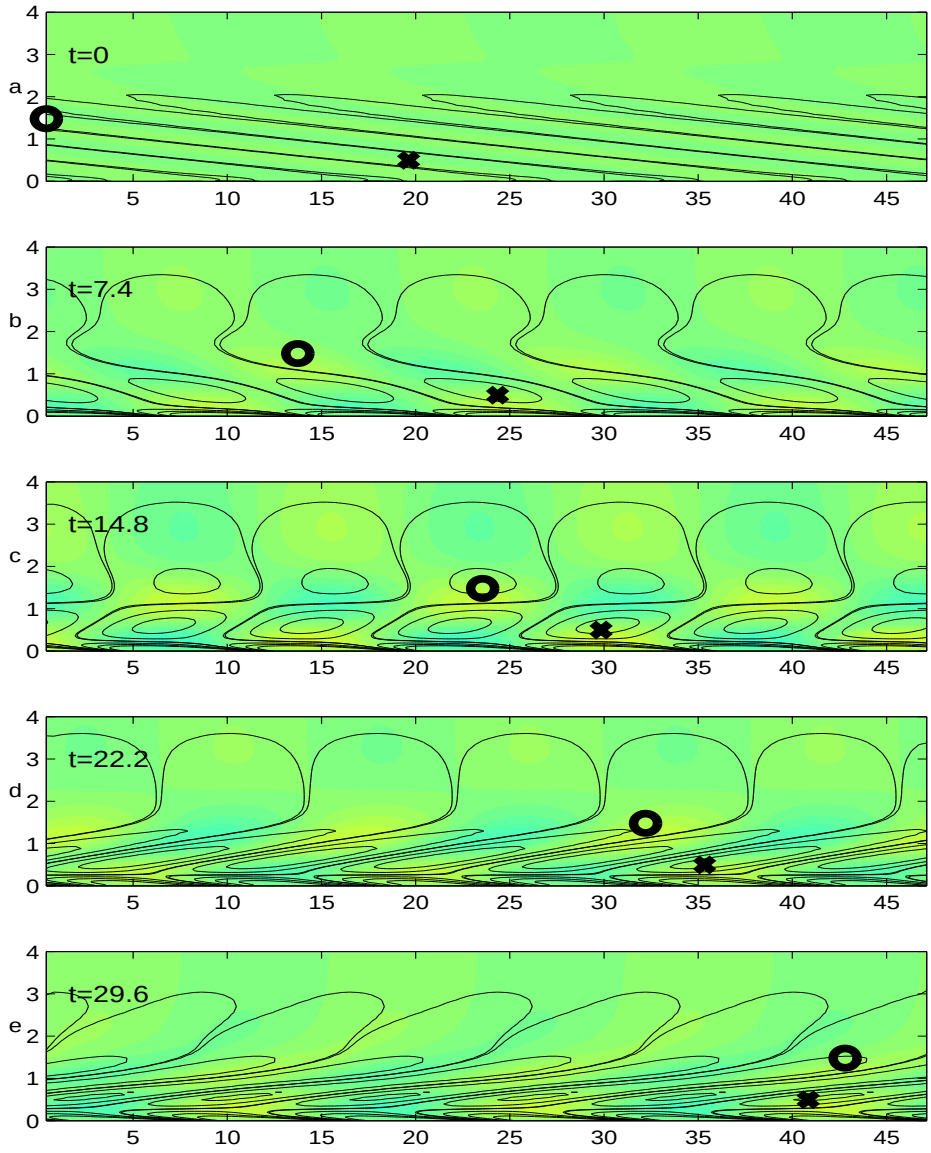

Figure 2.12: Same as Figure 2.11 for $Re = 2000$, $k = 0.4.$, $T_c = T_{max} = 22.2$, $\alpha = 0.5$ and $l = 1$. Vortex splitting is observed between b and c, while in the uncontrolled case in Figure 2.8, the vortices do not split.

occur naturally, blowing and suction at the wall tend to accelerate this process (Figure 2.11).

Transient vortex compression due to the spanwise shear is inevitable since the initial vorticity distribution inclined *against the shear* has to evolve into the least stable eigenmode configuration where the vorticity distribution is inclined *in the direction of the shear*. Moderate wall-normal blowing or suction, obtained with $\alpha = 0.5$ and $l = 1$, is unable to prevent this tilting process. However, the associated transient energy growth may be weakened by accelerating the disturbance evolution into the least stable eigenmode. Using this acceleration strategy, disturbances are given less time to extract energy from the basic flow; hence, not only the energy at $t = T_c$ but also the energy maximum between $t = 0$ and T_c are decreased.

2.6.3 Constant gain feedback control

The optimal control strategy designed above requires to compute the flow evolution from $t = 0$ to T_c several times, which may be computationally prohibitive for implementation in a real experiment. A more realistic, constant gain feedback control strategy can be devised which performs nearly as well as optimal control at a much lower computational cost.

Assuming that a sensor is located at a distance y_m from the wall, one may design a control law of the form

$$v_w(t) = \kappa v(y_m, t) \ , \tag{2.45}$$

where κ is a constant scalar gain and $v(y_m, t)$ is the wall-normal velocity measured at the height y_m from the wall. The gain κ and the height y_m can be tuned so as to minimize the objective functional (2.11). By setting $\kappa = 0.6$ and $y_m = 1.8$, the objective functional is decreased to $\mathcal{I} = 21.8$ in the linearly stable case $Re = 550$, $k = 0.25$, which should be compared to $\mathcal{I} = 18.9$ when optimal control is applied. In the linearly unstable case $Re = 850$, $k = 0.25$, the constant gain control strategy with $\kappa = 0.6$ and $y_m = 1.6$ yields $\mathcal{I} = 35.2$ whereas optimal control decreases the objective functional to $\mathcal{I} = 32.7$.

Figures 2.13a,b display the wall-blowing and suction sequences for constant gain and optimal control. In both the linearly stable and unstable case, the wall-blowing pattern takes the form of travelling waves which follow the vortical structures. The spatio-temporal evolution of the control pattern displays a nearly perfect phase match between both control sequences in time and space which also have amplitudes of the same order. This observation shows that constant gain feedback control provides a good approximation to the optimal control strategy.

The disturbance energy evolution with time is displayed in Figures 2.14a,b. The perturbations are efficiently damped by the constant gain feedback control (2.45) both for linearly stable and linearly unstable flow. The energy peak transiently

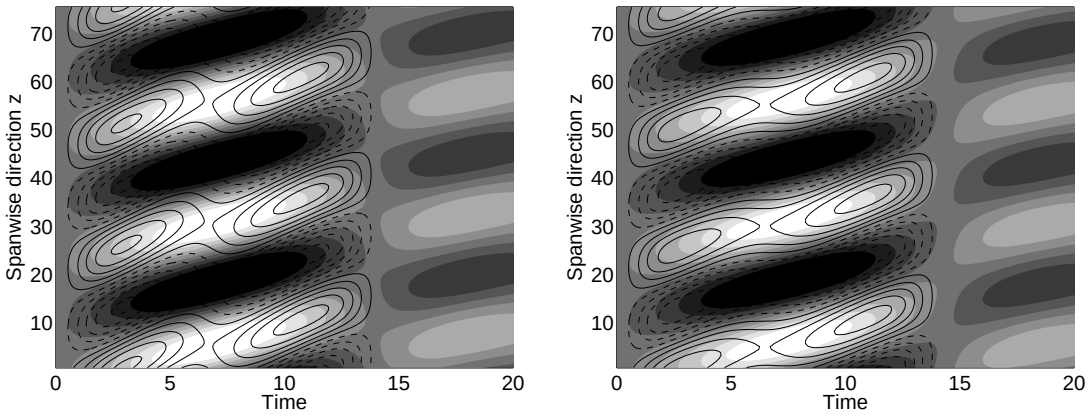

(a) (b)

Figure 2.13: Isocontours of the wall-normal velocity v_w at the wall in the (t, z)-plane for (a) linearly stable ($Re = 550,\ k = 0.25$) and (b) linearly unstable ($Re = 850,\ k = 0.25$) flow. Shaded contours represent constant gain control (light: blowing, dark: suction) whereas line contours represent optimal control (solid lines: blowing, dashed lines: suction). The constant gain and the location of the sensor have been set to (a) $\kappa = 0.6,\ y_m = 1.8$, (b) $\kappa = 0.6,\ y_m = 1.6$ in order to minimize the objective functional $\mathcal{I}$. The remaining parameters have been set equal to $T_p = 14.3$, $T_c = 14.3$, $\alpha = 0.5$, $l = 1$.

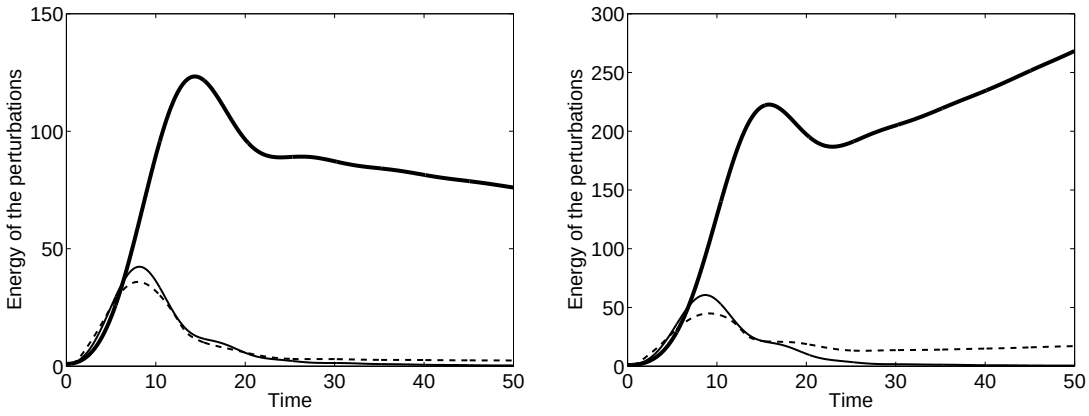

(a) (b)

Figure 2.14: Disturbance energy as a function of time for (a) linearly stable ($Re = 550,\ k = 0.25$) and (b) linearly unstable ($Re = 850,\ k = 0.25$) flow. The thick solid line represents the uncontrolled optimal perturbation. The thin solid line displays the energy of the same perturbation when constant gain control is applied, the dashed line its counterpart when optimal control is applied. The constant gain and the location of the sensor have been set to (a) $\kappa = 0.6$, $y_m = 1.8$, (b) $\kappa = 0.6$, $y_m = 1.6$ in order to minimize the objective functional $\mathcal{I}$. The remaining parameters have been set equal to $T_p = 14.3$, $T_c = 14.3$, $\alpha = 0.5$, $l = 1$.

reached between $t = 0$ and $T_c = 14.3$ is of the same order of magnitude with both control strategies.

Eventhough the gain κ and the sensor location y_m have been tuned to minimize the objective functional $\mathcal{I}$ only on a finite-time interval, simulations show that the linearly unstable flow is stabilized for large times: after a short transient amplification the perturbation energy decreases exponentially as long as control is applied (Figure 2.14b). The decay rate of the disturbance energy in the linearly stable case (Figure 2.14a) is enhanced by constant gain control.

The numerical experiments indicate that constant gain feedback control is able to decrease the objective functional $\mathcal{I}$ very efficiently at a rather low computational cost when suitably tuned, and that it restabilizes linearly unstable perturbations in the long term. By contrast, evaluating the objective functional gradient requires the computation of the direct and adjoint problems from $t = 0$ and T_c, which is computationally expensive; this computation also loses accuracy as T_c becomes large. Thus, the advantage of optimal control over constant gain feedback control may be lost for long-term optimizations. Constant gain feedback control strategies should, therefore, not be hastily discarded, but rather be considered as a viable option for controlling swept attachment-line boundary layers under realistic conditions.

2.7 Concluding remarks

An adjoint-based optimization procedure applicable to both the determination of the optimal perturbation and its optimal control has been developed, which relies on the introduction of a Lagrangian functional in the reduced $u - v$ setting (2.8)-(2.10). Although the formulation bears similarities to the previous investigations of Andersson *et al.* (1999) and Corbett & Bottaro (2001a,b), essential modifications have been introduced as outlined in section 2.3. In addition to the three scalar products (2.16a-c), the double-bracketed scalar product (2.13) needs to be defined in order to express the kinetic energy of the perturbations in terms of the (u, v) components only. Had the analysis been conducted in primitive variables u, v, w, p, the scalar product (2.13) would have been superfluous and the usual Eulerian scalar product would have been sufficient. In the reduced $u - v$ setting, however, its double-bracketed counterpart (2.13), which takes into consideration the continuity equation, has to be used both to calculate the kinetic energy and the gradient of the objective functional. Provided attention is given to these points, the gradients of the objective functional readily follow from the Lagrangian formulation.

Two-dimensional (y, z)-mechanisms in the flow dividing plane have been demon-

strated (section 2.5) to be responsible for most of the energy amplification of Görtler-Hämmerlin perturbations in swept Hiemenz flow. They involve spanwise-travelling vortices aligned in the chordwise direction that undergo a tilting of their vorticity distribution reminiscent of the Orr mechanism (Haynes (1987), Vanneste (1999)): the vorticity distribution, initially inclined against the sweep, is compressed by the shear, which causes the associated energy to transiently increase before it eventually decreases exponentially (for the linearly stable case) or increases exponentially (for the unstable case). The growth of optimal perturbations exhibits two essential features that are specific to the swept attachment-line boundary layer. First, the transient growth does not rely on a lift-up process (Landahl (1980)) as in classical boundary layers but on tilting of the vorticity distribution induced by the spanwise shear. Second, the resulting chordwise vortices are distorted by the basic flow to form dipole structures which, at low spanwise wavenumbers, result in increased levels of spanwise velocity perturbations. These issues are discussed in more detail below.

The lift-up mechanism associated with streamwise momentum transport by vortices aligned with the flow is primarily responsible for the energy amplification in weakly non-parallel shear flows (Schmid & Henningson 2001). In the present study, the Görtler-Hämmerlin assumption does not allow for chordwise modulations of the spanwise velocity w, thus precluding any lift-up associated with the spanwise shear $W'(y)$. The optimal perturbation has been shown to consist of chordwise vortices aligned with the chordwise shear $\partial U/\partial y(x, y)$. However, according to Figure 2.15a, lift-up effects associated with the chordwise shear $\partial U/\partial y(x, y)$ are weak: the maximum kinetic energy of the chordwise velocity perturbation, $\int_0^\infty u^* u \, dy$, accounts for only one thousandth of the total maximum energy amplification $E(T_{max})$ reached by optimal disturbances.

In contrast to weakly non-parallel boundary layers, the chordwise vortices involved in the lift-up mechanism are advected in the spanwise direction by the sweep W (Figure 2.15b); as a result, they do not coherently transport low-momentum fluid from the wall to the edge of the boundary layer and high-momentum fluid from the boundary layer toward the wall. Rather, up- and down-welling regions work in opposition as they are swept along the attachment-line. Figure 2.15a further illustrates the role of the basic sweep velocity in rendering the chordwise lift-up mechanism ineffective: higher Reynolds numbers, i.e. larger sweep velocities, lead to lower chordwise disturbance energy when compared to the total energy achieved by optimal perturbations. The only remaining amplification processes are therefore the Orr mechanism and vortex dipole formation.

The combined action of the spanwise shear $W'(y)$ and the compression by the impinging basic flow results in the tilting of the chordwise vorticity distribution and

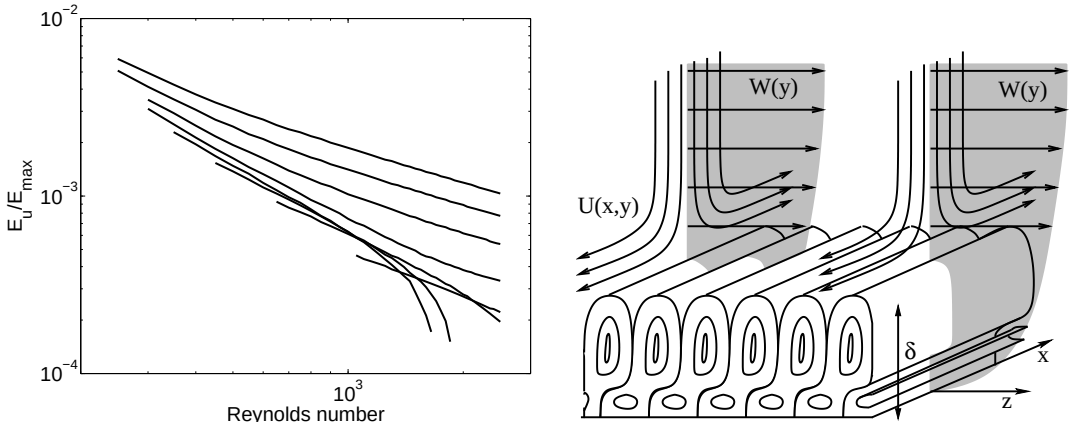

a b

Figure 2.15: (a) Fraction of the chordwise velocity perturbation energy $\int_0^\infty u^* u \, dy$ in the maximum total energy $E(T_{max})$ reached by optimal perturbations versus Reynolds number. Spanwise wavenumbers range from $k = 0.45$ (top curve) to $k = 0.1$ (bottom curve) in 0.05 increments. (b) Sketch illustrating the inefficiency of 'laterally swept' lift-up. The up- and down-welling regions aligned in the chordwise direction x work in opposition as they are swept in the z direction.

in the compression of the chordwise vortices into dipole structures, respectively. This process is the most effective at large spanwise wavelengths (low k) which allow for more elongated initial vorticity distributions. The vortices are confined to the spanwise boundary layer, the thickness of which is constant. When k is decreased below $k \sim 0.25$ vorticity patches can no longer be tilted up by the basic shear and time remain inside the boundary layer without undergoing vortex splitting (Figure 2.7). When k is above 0.25, the process is incomplete: vortices are merely distorted and dipolar structures are not observed (Figure 2.8). The optimal wall blowing/suction sequence which has been shown to resemble constant gain feedback control (section 2.6.3), enhances the above compression process by pushing the vortices against the impinging flow.

The present study was solely aimed at describing Görtler-Hämmerlin disturbances near the attachment-line within the context of the idealized swept Hiemenz flow model. The optimal growth of *arbitrary* disturbances in swept Hiemenz flow remains to be determined: according to the studies of Theofilis *et al.* (2003) and Obrist and Schmid (2003b), higher-order chordwise polynomial expansions may be expected to (a) yield stronger amplifications than Görtler-Hämmerlin perturbations and (b) introduce additional unstable modes. The stronger growth is caused by the superposition of modes with very similar wall-normal shapes (Obrist & Schmid 2003b). The additional unstable modes, although less unstable than Görtler-Hämmerlin modes, may compromise the efficiency of constant gain feedback control schemes which are unable to stabilize multiple modes.

Moreover, the precise relationship between the present spanwise travelling chordwise vortices generated by transiently amplified or genuinely unstable perturbations at the attachment-line and the steady crossflow vortices produced in the three-dimensional boundary layer on the wing surfaces (Arnal et al. (1984), Bertolotti (1999), Koch *et al.* 2000, among others) remains to be determined.

Acknowledgments

The authors gratefully acknowledge many enlightening and productive discussions with Carlo Cossu and François Gallaire. Alan Guégan holds a PhD fellowship from CNRS and the French "Délégation Générale pour l'Armement". Peter Schmid's stay at LadHyX was financially supported by the CNRS.

Chapter 3

Optimal temporal disturbances of arbitrary shape

3.1 Introduction

In the Görtler-Hämmerlin framework the wall-normal and spanwise v, w perturbation velocity components are assumed to be homogeneous in the chordwise $x-$direction, whereas the chordwise u velocity component increases linearly away from the dividing plane $x = 0$. The least stable eigenmode in swept Hiemenz flow takes the peculiar shape of a Görtler-Hämmerlin mode but there is no reason to assume that this will apply to optimal disturbances. In order to find the disturbance whose energy is amplified most over a finite time interval, it is necessary to relax the Görtler-Hämmerlin assumption and to compute directly the three-dimensional perturbation equations by resorting to a Direct Numerical Simulation (DNS) code.

The computational bottleneck of gradient-based optimization algorithms lies in the large number of objective functional evaluations. In the temporal framework, for each evaluation the linearized Navier-Stokes equations are solved from $t = 0$ to T. Since several evaluations of the objective functional are involved during the optimization process, it is crucial to devise an efficient simulation algorithm to keep computational costs reasonably low.

Obrist (2000) has adapted a well-documented spectral simulation code developed at KTH by Lundbladh et al. (1992) to assess the temporal evolution of three-dimensional perturbations in swept Hiemenz flow. This numerical scheme can be used in conjunction with the optimization algorithm derived in chapter 2 to determine optimal temporal disturbances in swept Hiemenz flow.

In section 3.2 the Direct Numerical Simulation code is described. Perturbation equations are presented in a velocity-vorticity form which is particularly well suited for numerical treatment. The temporal discretization scheme and the spatial discretization are briefly described; the reader is referred to Obrist (2000) for further detail. The use of the fringe region technique in the context of adjoint-based flow optimization is discussed in section 3.3. Optimal temporal perturbations are computed and analyzed in section 3.4.

3.2 Direct numerical simulation

3.2.1 Direct perturbation equations

The perturbation equations for u, v, w, p are not solved in their 'primitive variable' form, with three momentum equations and the continuity equation. Instead, a velocity-vorticity $\nabla^2 v, \omega$ formulation is derived in which only two time-dependent equations have to be marched in time.

In non-dimensional form the Navier Stokes equations read

$$\partial_t u_i = -\partial_{x_i} p + H_i - \partial_{x_i}(\frac{1}{2} u_j u_j) + \frac{1}{Re}\nabla^2 u_i \ , \tag{3.1a}$$

$$\partial_{x_i} u_i = 0 \tag{3.1b}$$

with

$$H_i = \varepsilon_{ijk} u_j \omega_k \ , \tag{3.2a}$$

$$\nabla^2 = \partial_{xx} + \partial_{yy} + \partial_{zz} \ . \tag{3.2b}$$

Spatial coordinates $x_i = (x_1, x_2, x_3)$ refer to the x, y, z coordinates sketched in Figure 3.1. The corresponding velocity and vorticity u_i- and ω_i-vectors are denoted u, v, w and ψ, ω, θ, respectively.

By applying the Laplace operator to momentum equation (3.1a) for $u_2 = v$, and taking advantage of the continuity equation to simplify the resulting equation, one gets an equation for the Laplacian of v,

$$\partial_t \phi = (\partial_{xx} + \partial_{zz}) H_2 - \partial_y(\partial_x H_1 + \partial_z H_3) + \frac{1}{Re}\nabla^2 \phi \ , \tag{3.3}$$

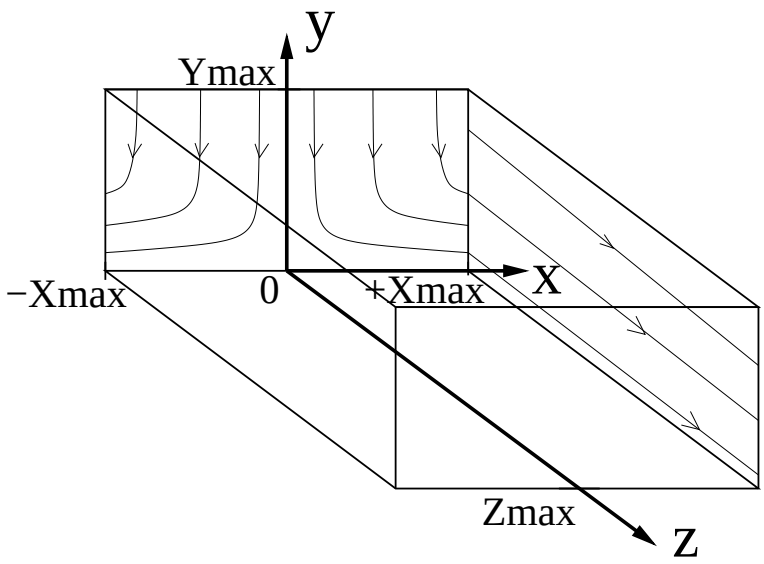

Figure 3.1: Sketch of the computational domain with streamlines of the base flow in the (x, y) and (y, z) planes.

with

$$\phi = \nabla^2 v \ . \tag{3.4}$$

Taking the curl of equation (3.1a) yields an equation for the wall-normal vorticity ω:

$$\partial_t \omega = \partial_z H_1 - \partial_x H_3 + \frac{1}{Re}\nabla^2 \omega \ . \tag{3.5}$$

Equations (3.3), (3.4) and (3.5) make up the velocity-vorticity formulation of the Navier Stokes equations.

Swept Hiemenz flow U, V, W is an exact solution of the Navier Stokes equations. It can be subtracted from the velocity components u, v, w to get the perturbation velocities

$$(u', v', w') = (u - U, v - V, w - W) \ . \tag{3.6}$$

Similarly, the perturbation vorticity is obtained by subtracting the vorticity field Ψ, Ω, Θ associated with swept Hiemenz flow from the vorticity field ψ, ω, θ ,

$$(\psi'\omega', \theta') = (\psi - \Psi, \omega - \Omega, \theta - \Theta) \ . \tag{3.7}$$

In terms of perturbation variables ϕ', ω' the velocity-vorticity formulation reads

$$\begin{aligned}
\partial_t \phi' &= (\partial_{xx} + \partial_{zz}) H_2' - \partial_y (\partial_x H_1' + \partial_z H_3') + \frac{1}{Re} \nabla^2 \phi' \ , && \text{(3.8a)} \\
\partial_t \omega' &= \partial_z H_1' - \partial_x H_3' + \frac{1}{Re} \nabla^2 \omega' \ , && \text{(3.8b)} \\
\nabla^2 v' &= \phi' \ , && \text{(3.8c)}
\end{aligned}$$

with

$$\begin{aligned}
H_1' &= H_1 - V\Theta + W\Omega \ , && \text{(3.9a)} \\
H_2' &= H_2 - W\Psi + U\Theta \ , && \text{(3.9b)} \\
H_3' &= H_3 - U\Omega + V\Psi \ . && \text{(3.9c)}
\end{aligned}$$

Upon gathering the advective and non-linear terms in $h_{\phi'}$ and $h_{\omega'}$ defined as

$$\begin{aligned}
h_{\phi'} &= (\partial_{xx} + \partial_{zz}) H_2' - \partial_y (\partial_x H_1' + \partial_z H_3') \ , && \text{(3.10a)} \\
h_{\omega'} &= \partial_z H_1' - \partial_x H_3' \ , && \text{(3.10b)} \\
& && \text{(3.10c)}
\end{aligned}$$

the Navier-Stokes equations take the symmetrical and compact form

$$\begin{aligned}
\partial_t \phi' &= h_{\phi'} + \frac{1}{Re} \nabla^2 \phi' \ , && \text{(3.11a)} \\
\partial_t \omega' &= h_{\omega'} + \frac{1}{Re} \nabla^2 \omega' \ , && \text{(3.11b)} \\
\nabla^2 v' &= \phi' \ . && \text{(3.11c)}
\end{aligned}$$

The Direct Numerical Simulation algorithm that will be described in sections 3.2.3 and 3.2.4 aims at solving equations (3.11a,b,c). Since no further reference will be made to the unperturbed non-dimensional variables $u, v, w,\ \phi, \omega, \theta,\ \phi$, the primes denoting perturbation fields are subsequently dropped. In particular the velocity-vorticity variables ϕ', ω', v' are now denoted ϕ, ω, v.

3.2.2 Adjoint perturbation equations

Numerically speaking, solving both time-dependent equations (3.11a) and (3.11b) in the reduced ϕ, ω setting is more efficient than solving the four equations in the primitive variable u, v, w, p setting. As for the adjoint equations, one can either derive the adjoint problem for $\tilde{\phi}, \tilde{\omega}$ directly from the reduced setting, or derive the adjoint problem $\tilde{u}, \tilde{v}, \tilde{w}, \tilde{p}$ from the primitive variable setting and then find an analogous reduced setting from the four adjoint equations.

In chapter 2 the Görtler-Hämmerlin equations could be reduced to a set of two equations that involved only the chordwise $u-$ and wall-normal $v-$velocities. Adjoint equations for $\tilde{u}, \tilde{v}$ could be derived directly from the u, v setting. By contrast, equations in the reduced setting ϕ, ω involve not only ϕ and ω but also velocity and vorticity fields u, v, w, ψ, θ; these variables are required to compute the h_ϕ, h_ω right-hand-side terms. It is impossible to derive a reduced set of equations that involve ϕ, ω only, from which one could derive adjoint equations for $\tilde{\phi}, \tilde{\omega}$. If the adjoint problem were to be derived from equations (3.11a,b,c) it would involve not only the adjoint $\tilde{u}, \tilde{v}, \tilde{w}$ velocity fields but also the adjoint $\tilde{\psi}, \tilde{\omega}, \tilde{\theta}$ vorticity fields.

By contrast, it is a fairly straightforward task to derive the adjoint problem in primitive variables first, and then derive a reduced set of adjoint equations through algebraic manipulations similar to those that yielded the ϕ, ω setting for the direct problem. Adjoint equations derived in the primitive variable setting read:

$$
\begin{aligned}
\left(\partial_t + U\partial_x + V\partial_y + W\partial_z + Re^{-1}\nabla^2\right)\tilde{u} & \\
-\partial_x U\tilde{u} - \partial_x\tilde{p} &= 0\ , \qquad (3.12a)\\
\left(\partial_t + U\partial_x + V\partial_y + W\partial_z + Re^{-1}\nabla^2\right)\tilde{v} & \\
-V'\tilde{v} - U'\tilde{u} - W'\tilde{w} - \partial_y\tilde{p} &= 0\ , \qquad (3.12b)\\
\left(\partial_t + U\partial_x + V\partial_y + W\partial_z + Re^{-1}\nabla^2\right)\tilde{w} - \partial_z\tilde{p} &= 0\ , \qquad (3.12c)\\
\partial_x\tilde{u} + \partial_y\tilde{v} + \partial_z\tilde{w} &= 0\ . \qquad (3.12d)
\end{aligned}
$$

The adjoint equations (3.12) can be recast into a reduced set of equations similar to the vorticity-velocity formulation of the Navier-Stokes equations, by introducing the Laplacian $\tilde{\phi}$ of the wall-normal velocity $\tilde{v}$ and the adjoint vorticity $\tilde{\omega}$,

$$
\begin{aligned}
\tilde{\phi} &= \nabla^2\tilde{v}\ , \qquad (3.13a)\\
\tilde{\omega} &= \partial_z\tilde{u} - \partial_x\tilde{w}\ . \qquad (3.13b)
\end{aligned}
$$

The adjoint velocity-vorticity equations read:

$$
\begin{aligned}
&\left(\partial t + U\partial_x + V\partial_y + W\partial_z + Re^{-1}\nabla^2\right)\tilde{\phi} \\
&\quad -3V'\partial_{xx}\tilde{v} + 2V''\partial_x\tilde{u} - U'(2\partial_{xx}\tilde{u} + \partial_{zz}\tilde{u} + \partial_{xz}\tilde{w}) \\
&\quad\quad -V'(\partial_{zz}\tilde{v} + \partial_{xy}\tilde{u} + \partial_{zy}\tilde{w}) - W'(\partial_{xx}\tilde{w} + \partial_{xz}\tilde{u}) &= 0\ , \quad (3.14a)\\
&\left(\partial t + U\partial_x + V\partial_y + W\partial_z + Re^{-1}\nabla^2\right)\tilde{\omega} + V'(\partial_z\tilde{u} + \partial_x\tilde{w}) &= 0\ , \quad (3.14b)
\end{aligned}
$$

which can be cast in the general form of equations (3.11a,b,c), i.e.

$$
\begin{aligned}
\partial_t\tilde{\phi} &= \tilde{h}_\phi + \frac{1}{Re}\nabla^2\tilde{\phi}\ , &(3.15a)\\
\partial_t\tilde{\omega} &= \tilde{h}_\omega + \frac{1}{Re}\nabla^2\tilde{\omega}\ , &(3.15b)\\
\nabla^2\tilde{v} &= \phi\ , &(3.15c)
\end{aligned}
$$

with

$$
\begin{aligned}
\tilde{h}_\phi &= -\left(U\partial_x + V\partial_y + W\partial_z\right)\tilde{\phi} \\
&\quad - 3V'\partial_{xx}\tilde{v} + 2V''\partial_x\tilde{u} - U'(2\partial_{xx}\tilde{u} + \partial_{zz}\tilde{u} + \partial_{xz}\tilde{w}) \\
&\quad - V'(\partial_{zz}\tilde{v} + \partial_{xy}\tilde{u} + \partial_{zy}\tilde{w}) - W'(\partial_{xx}\tilde{w} + \partial_{xz}\tilde{u})\ , \quad (3.16a)\\
\tilde{h}_\omega &= \left(U\partial_x + V\partial_y + W\partial_z + Re^{-1}\nabla^2\right)\tilde{\omega} + V'(\partial_z\tilde{u} + \partial_x\tilde{w})\ . \quad (3.16b)
\end{aligned}
$$

Equations (3.15) are identical to direct equations 3.11 and can be solved using the same numerical scheme. Programming efforts are substantially reduced by resorting to the counterpart $\tilde{\phi}, \tilde{\omega}$ of the velocity-vorticity formulation ϕ, ω.

3.2.3 Temporal scheme

Equations (3.11a,b) are solved with a combined implicit-explicit time integration scheme. The advective and non-linear terms h_ϕ, h_ω are integrated explicitly using the three-stage, third-order Runge-Kutta scheme by Williamson (1980). The viscous terms are solved implicitly using a Crank-Nicolson scheme. The solution ϕ^{n+1}, ω^{n+1} to equations (3.11a,b) at timestep $n+1$ is computed from fields $\phi, \omega, h_\phi, h_\omega$ at timesteps n and $n-1$ according to

$$
\begin{aligned}
\phi^{n+1} &= \phi^n + a_n h_\phi^n + b_n h_\phi^{n-1} + \frac{a_n + b_n}{2Re}(\nabla^2\phi^{n+1} + \nabla^2\phi^n)\ , &(3.17a)\\
\omega^{n+1} &= \omega^n + a_n h_\omega^n + b_n h_\omega^{n-1} + \frac{a_n + b_n}{2Re}(\nabla^2\omega^{n+1} + \nabla^2\omega^n)\ . &(3.17b)
\end{aligned}
$$

Coefficients a_n, b_n are given in Table 3.1.

Stage number	a_n	b_n
0	$\frac{8}{15}\ \delta t$	0
1	$\frac{5}{12}\ \delta t$	$\frac{-17}{60}\ \delta t$
2	$\frac{3}{4}\ \delta t$	$\frac{-5}{12}\ \delta t$

Table 3.1: Coefficients for the three-stage time integration scheme

Following Obrist (2000) the step size δt is determined by the CFL condition

$$\delta t = \frac{\pi}{\mu}\left(\frac{|u_{max}|}{\delta x} + \frac{|w_{max}|}{\delta z} + \left|\frac{v}{\delta y}\right|_{max}\right) \ , \tag{3.18}$$

with $\mu = 0.8$.

Using the time-integration scheme (3.17a,b), marching the solution forward in time amounts to solving a set of spatial Helmholtz equations

$$\left(1 - \frac{a_n + b_n}{2Re}\nabla^2\right)\phi^{n+1} = \left(1 + \frac{a_n + b_n}{2Re}\nabla^2\right)\phi^n + a_n h_\phi^n + b_n h_\phi^{n-1} \ , \tag{3.19a}$$

$$\left(1 - \frac{a_n + b_n}{2Re}\nabla^2\right)\omega^{n+1} = \left(1 + \frac{a_n + b_n}{2Re}\nabla^2\right)\omega^n + a_n h_\omega^n + b_n h_\omega^{n-1} \ , \tag{3.19b}$$

$$\nabla^2 v^{n+1} = \phi^{n+1} \ . \tag{3.19c}$$

Although only ϕ, ω, v are explicitly solved for, the computation of the advective and non-linear terms h_ϕ, h_ω defined in equations (3.10) requires the additional knowledge of u, w, ψ, θ. These quantities are computed a posteriori from ϕ^{n+1}, ω^{n+1}, v^{n+1}, by solving

$$(\partial_x x + \partial_{zz})u^{n+1} = -\partial_x\partial_y v^{n+1} + \partial_z\omega^{n+1} \ , \tag{3.20a}$$

$$(\partial_x x + \partial_{zz})w^{n+1} = -\partial_z\partial_y v^{n+1} - \partial_x\omega^{n+1} \ , \tag{3.20b}$$

$$(\partial_x x + \partial_{zz})\psi^{n+1} = -\partial_x\partial_y\omega^{n+1} - \partial_z\phi^{n+1} \ , \tag{3.20c}$$

$$(\partial_x x + \partial_{zz})\theta^{n+1} = -\partial_z\partial_y\omega^{n+1} + \partial_x\phi^{n+1} \ . \tag{3.20d}$$

3.2.4 Spatial discretization

It is not our intention to provide a thorough description of the spatial discretization techniques employed here since they have been extensively used in the past. For a detailed description of the spatial discretization, the reader is referred to Obrist (2000) and Lundbladh et al. (1992).

The DNS algorithm is based on pseudo-spectral methods; spatial differentiation is achieved in spectral space and the advective and nonlinear terms are computed in physical space. Converting variables from spectral to physical space is very efficient in terms of computational cost; differentiation, which is more efficient in Fourier space, is achieved in spectral space whereas physical fields are multiplied in physical space to yield advective and non-linear terms.

Computational domain

Swept Hiemenz flow is defined over the semi-infinite domain $y \geq 0$ but the computational domain sketched in Figure 3.1 is of finite extent. In the wall-normal $y-$direction the Navier-Stokes equations are solved between $y = 0$ and y_{max}, where the farthest wall-normal point y_{max} is set at about 30 times the boundary-layer thickness to prevent any influence on the inner solution. In the chordwise direction, the domain stretches from $-x_{max}$ to $+x_{max}$. Since the basic flow is homogeneous in z, the disturbances may be Fourier transformed in the spanwise direction with periodic boundary conditions in the spanwise $z-$direction.

Since Fourier modes decouple in the spanwise $z-$direction, linear temporal perturbations of spanwise wavenumber k may be computed separately; each simulation then involves a single Fourier mode k in the spanwise $z-$direction.

The full, non-linear Navier-Stokes equations are solved in the DNS code. To achieve linearity in practice, very-low-energy disturbances are computed; non-linear terms are virtually zero and the disturbance evolution is driven by the linear terms only.

Spatial discretization techniques

Chordwise $x-$direction Since we want to use Fourier transforms in the chordwise $x-$direction, periodic boundary conditions are required at $\pm x_{max}$. In order to enforce periodicity a damping term $-\lambda_x(x)(\phi, \omega)$ is added to equations (3.11a,b) to drive perturbations to zero as they approach the chordwise boundary $\pm x_{max}$. The modified equations read

$$\partial_t \phi = h_\phi + \frac{1}{Re}\nabla^2\phi - \lambda_x(x)\phi \ , \tag{3.21a}$$

$$\partial_t \omega = h_\omega + \frac{1}{Re}\nabla^2\omega - \lambda_x(x)\omega \ , \tag{3.21b}$$

$$\nabla^2 v = \phi \ , \tag{3.21c}$$

where the damping parameter is taken to be

$$\lambda_x(x) = \lambda_{x\ max}\left(1 - S\left(\frac{x + x_{max}}{d_x}\right) + S\left(\frac{x - x_{max}}{d_x}\right)\right) \ , \tag{3.22}$$

with $\lambda_{x\ max}$ as the amplitude of the damping and d_x as the width of the fringe. The smooth step function S is defined as

$$S(x) = \left\{ \begin{array}{cc} 0 \ , & \text{if } x \leq 0 \\ (1 + \exp(\frac{1}{x-1} + \frac{1}{x}))^{-1} \ , & \text{if } 0 < x < 1 \\ 1 \ , & \text{if } x \geq 1 \end{array} \right\} \ . \tag{3.23}$$

The so-called 'fringe region technique' was first introduced by Spalart and Yang (1987) to study transition in the Blasius boundary layer; it was theoretically studied by Nordström et al. (1999). In the context of swept Hiemenz flow, Obrist (2000) has shown that the Navier-Stokes equations are solved exactly outside the fringe, in the region $-x_{max} + d_x < x < x_{max} - d_x$, with the perturbations vanishing at $x = \pm x_{max}$.

Introducing a linear damping term at the outer boundaries is an efficient way to ensure periodicity of the disturbances in x. For that purpose, the physical equations have been modified; the adjoint equations will also be affected by the procedure. The application of the fringe region technique in adjoint-based optimization schemes is discussed in section 3.3.

Spanwise $z-$direction In the temporal framework the disturbances are periodic along the spanwise direction. Perturbations are Fourier-transformed in the spanwise $z-$direction with periodic boundary conditions in z.

Wall-normal $y-$direction The presence of a wall at $y = 0$ suggests the use of Chebyshev polynomials associated with an algebraic coordinate mapping to cluster the discretization points near $y = 0$. A total of n_y points are distributed in the wall-normal $y-$direction according to

$$y_j = A\frac{1+\eta_j}{B-\eta_j} \ , \tag{3.24}$$

where η_j represents the j^{th} Gauss-Lobatto point defined by

$$\eta_j = \cos\left(\frac{j-1}{n_y-1}\pi\right) \ . \tag{3.25}$$

The mapping is defined by the two parameters A, B which set the location y_{max} of the point farthest from the wall and the location y_{half} below which half of the Gauss-Lobatto points are mapped according to

$$y_{max} = \frac{2A}{B-1} \ , \tag{3.26a}$$

$$y_{half} = \frac{A}{B} \ . \tag{3.26b}$$

$$\tag{3.26c}$$

3.3 Optimization techniques in swept Hiemenz flow

The perturbation equations and the temporal and spatial discretizations have been described. Before computing optimal disturbances a few comments should be made on the definition of the energy and the use of the fringe region technique together with adjoint-based optimization algorithms.

3.3.1 Definition of the energy

The kinetic energy is commonly defined as

$$E = \frac{1}{2}\int_{y\geq 0}\left(u^2+v^2+w^2\right)\ dx\ dy\ dz \ . \tag{3.27}$$

The evolution of the kinetic energy E with time should give a reasonable picture of perturbation amplification.

In swept Hiemenz flow the chordwise $u-$velocity and the associated shear increase indefinitely along the chordwise direction as x tends to infinity: this flow model is an accurate representation of the leading-edge boundary layer close to the

attachment-line only; it fails, however, as x tends to infinity. As a consequence, only disturbances located at moderate values of x should be investigated.

As was the case in previously investigated flows, the strongest energy amplification is expected at locations where the shear is highest. Therefore, optimal perturbations in swept Hiemenz flow should be located at $x = \pm\infty$, which contradicts the small-x requirement.

In order to check this hypothesis the optimization algorithm was initialized with random disturbances q_0^0 located close to the attachment line, and the location of the iterates of the optimization algorithm was monitored. After the first two steps of the optimization the 'optimal guess' initial disturbance q_0^k was located strictly inside the boundary layer at nearly the same $x-$location as the initial guess q_0^0, and it started to take on the vorticity-sheet shape of the optimal disturbances described in section 3.4: the optimal modification of q_0^0, or the steepest slope at that stage of the gradient algorithm, consisted in concentrating the initial perturbation inside the boundary-layer where the shear is considerably stronger than outside and putting it into the vorticity-sheet-like shape.

Once the first optimization steps had been taken, the optimal modification to the initial disturbance was to move it into regions where stronger shear could be used to grow the disturbances. Indeed, as the optimization continued, the successive iterates q_0^k drifted away from the attachment-line towards regions of stronger chordwise shear. Accordingly, the energy amplification $(E(T)/E(0))^k$ grew without bounds as the initial disturbance reached regions of ever stronger shear.

To avoid optimal perturbations drifting away indefinitely from the attachment line the degeneracy of the swept Hiemenz flow model has to be taken into account in the definition of the energy. For instance, Obrist and Schmid (2003a) considered the weighted energy

$$E = \frac{1}{2}\int_{y>0} \lambda_E(x)\left(u^2 + v^2 + w^2\right)\, dx\, dy\, dz \tag{3.28}$$

where $\lambda_E(x)$ is a Gaussian weight. Perturbations located at $x = 0$ contribute fully to the kinetic energy; the contribution of disturbances located far away from the attachment line tends to zero. This energy norm arises naturally in the definition of the scalar product for Hermite polynomials which represent the best-suited basis to describe disturbances in swept Hiemenz flow (see, e.g., Obrist and Schmid (2003a)). Besides its mathematical justification, this norm has the advantage of deemphasizing perturbations located far away from the attachment line.

The chordwise extent of the weighing function has to be chosen judiciously; we took λ_E to be ten times the boundary-layer thickness to allow a rich physical behav-

ior and, at the same time, constrain disturbances to the vicinity of the symmetry plane $x = 0$.

3.3.2 Adjoint-based optimization and the fringe region technique

The damping term $-\lambda_x(\phi, \omega)$ was introduced in equations (3.21) after the direct equations had been reduced to the velocity-vorticity ϕ, ω form. Since the reduced variables are derivatives of the primitive variables u, v, w, p and the damping weight λ_x itself depends on the chordwise coordinate x, there is no straightforward way to express the modified equations (3.21a,b,c) in a primitive variable form similar to equations (3.1a,b). In particular, equations (3.21a,b,c) are not a reduced form of, say,

$$\partial_t u_i = -\partial_{x_i} p + H_i - \partial_{x_i}(\frac{1}{2} u_j u_j) + \frac{1}{Re}\nabla^2 u_i - \lambda_x u_i \ , \tag{3.29a}$$

$$\partial_{x_i} u_i = 0 \ . \tag{3.29b}$$

There is no *a priori* justification for introducing linear damping in the reduced rather than in the primitive variable equations. It is a natural choice since the temporal equations solved in the numerical simulation are those for ϕ and ω. In practice, if the linear damping terms $\lambda_x(u, v, w)$ are introduced in the primitive variable setting, derivatives of λ_x appear in the reduced set of equations (3.11) and the numerical scheme becomes unstable.

The adjoint equations have been derived in the primitive variable form (see section 3.2.2). Since one does not know *a priori* the primitive-variable form of the modified perturbation equations (3.21a,b,c), the adjoint problem may not be derived directly from the modified problem with damping in x.

However, as long as perturbations are far from the fringe region, their evolution is governed by the original undamped Navier-Stokes equations. Introducing a linear damping term $-\lambda_x(\phi, \omega)$ should leave perturbations far from the outer chordwise $x-$boundary unaltered. In the end, the fringe region is merely a method to enforce boundary conditions and should not be taken into account when deriving the adjoint formulation.

The correct way to derive an optimization algorithm is, first, to derive the adjoint equations and the entire optimization scheme with the original direct equations without damping and, second, introduce damping terms independently in the direct and adjoint problems to solve both sets of equations numerically. The equations may

then be recast into the reduced velocity-vorticity setting or left in primitive variable form; the crucial point is that perturbations are localized far from the fringe region, so that the artificial linear damping does not alter the results. Such a scheme can be found in, e.g., Högberg and Henningson (2002). The direct and adjoint equations in reduced form, with the fringe region, read

$$\partial_t \phi = h_\phi + \frac{1}{Re}\nabla^2\phi - \lambda_x \phi \ , \tag{3.30a}$$

$$\partial_t \omega = h_\omega + \frac{1}{Re}\nabla^2\omega - \lambda_x \omega \ , \tag{3.30b}$$

$$\nabla^2 v = \phi \ , \tag{3.30c}$$

$$\partial_t \tilde{\phi} = \tilde{h}_\phi + \frac{1}{Re}\nabla^2\tilde{\phi} - \lambda_x \tilde{\phi} \ , \tag{3.31a}$$

$$\partial_t \tilde{\omega} = \tilde{h}_\omega + \frac{1}{Re}\nabla^2\tilde{\omega} - \lambda_x \tilde{\omega} \ , \tag{3.31b}$$

$$\nabla^2 \tilde{v} = \phi \ . \tag{3.31c}$$

3.4 Optimal disturbances in swept Hiemenz flow

Alan Guégan, Patrick Huerre and Peter J. Schmid
Laboratoire d'Hydrodynamique (LadHyX), CNRS – École Polytechnique, F-91128 Palaiseau, France

Published in the *Journal of Fluid Mechanics*.

Abstract

The initial perturbation with the largest transient energy growth is computed in the context of the swept leading edge boundary layer. The highest energy amplification is found for perturbations which are homogeneous in the spanwise z direction although on shorter time scales the most amplified disturbances have a finite spanwise wavenumber. In both cases the production term associated with the shear of the spanwise velocity is responsible for the energy amplification in the perturbation energy equation. A connection is made with the amplification mechanism exhibited

by optimal perturbations in streaky boundary layers (Hoepffner et al. (2005)) and the results are compared to the optimal Görtler-Hämmerlin disturbances computed by Guégan et al. (2006).

3.4.1 Introduction

Linear stability analysis falls short of explaining the mechanisms that lead to turbulence because it focuses only on the long-term behaviour of infinitesimal disturbances, whereas short-term phenomena may be crucial to transition. The interest in transient growth has been boosted by the possibility to compute the initial perturbation of a given shear flow that is most amplified over a finite time span, referred to as the optimal perturbation. It has been shown in several prototypical flows that the energy of initially infinitesimal disturbances may be amplified by several orders of magnitude, reaching levels at which nonlinear effects become significant.

The boundary layer at the leading edge of swept wings sketched in Figure 3.2 is one among many examples of shear flows that can sustain transient energy amplification, such as Couette, Poiseuille and Blasius velocity profiles (Butler and Farrell (1992)). Guégan *et al* (2006) have demonstrated that the energy of a particular class of perturbations with a spatial structure that satisfies the so-called Görtler-Hämmerlin assumption may be amplified by up to three orders of magnitude over finite time.

The strength of the sweep velocity W in the spanwise $z-$direction is a crucial parameter for perturbation growth. In commercial airplanes with a sweep angle close to 30°, the vicinity of the attachment-line is characterized by strong advection in the spanwise direction, which may therefore be referred to as the streamwise direction. The associated Reynolds number based on the sweep velocity lies around $Re = 10^3$. In two-dimensional (Butler and Farrell (1992)) and three-dimensional (Corbett and Bottaro (2001a)) boundary layers the optimal perturbations take the shape of vortical structures aligned with the mean streamwise advection and periodically distributed along the wall, perpendicular to the main stream. The so-called lift-up mechanism (Landahl (1980)) is responsible for the energy amplification of such disturbances. The restrictive Görtler-Hämmerlin assumption, however, cannot describe streamwise vortices periodically distributed in the chordwise $x-$direction, since this assumption requires the chordwise $u-$velocity component of the perturbations to grow linearly away from the attachment-line. It can be suspected that relaxing the Görtler-Hämmerlin hypothesis one may expect stronger energy growth than has been found by Guégan *et al* (2006).

In the present study, direct numerical simulations have been used in conjunction with a gradient optimization algorithm in order to determine the *general* three-

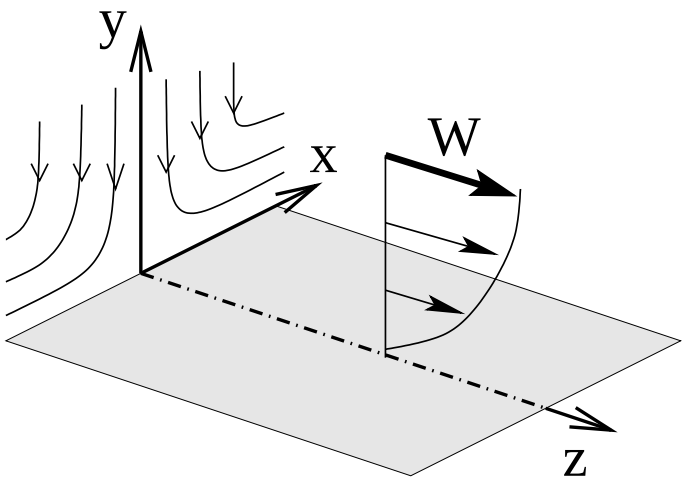

Figure 3.2: Sketch of swept Hiemenz flow showing the dividing streamlines in the chordwise x direction and the sweep velocity W in the spanwise z direction.

dimensional optimal perturbation in swept Hiemenz flow. The dependence of the energy growth on the Reynolds number and the spanwise wavenumber has been investigated and the spatial structure of the optimal perturbation has been determined. The results are discussed in light of the previous studies of Hoepffner *et al* (2005) on optimal perturbations of nonlinearly saturated streamwise streaks and of Guégan *et al* (2006) on optimal perturbations within the Görtler-Hämmerlin framework.

3.4.2 Flow configuration and numerical techniques

Linear perturbations in swept Hiemenz flow

Swept Hiemenz flow is an exact solution of the Navier-Stokes equations. It models the flow near the leading edge of a swept wing in the neighborhood of the attachment-line, on each side of which the impinging flow divides symmetrically (Figure 3.2). The stretching chordwise velocity $U(x, y)$ is assumed to increase linearly with the chordwise $x-$direction, whereas the wall-normal velocity $V(y)$ and the spanwise sweep velocity $W(y)$ are assumed to be homogeneous in x. The only flow parameter is the Reynolds number

$$Re = \frac{W_\infty (\nu/S)^{\frac{1}{2}}}{\nu} \tag{3.32}$$

based on the stretching rate $S = (dU/dx)_{y\to\infty}$, the sweep velocity at infinity W_∞ and the kinematic viscosity ν. The Reynolds number quantifies the sweep angle and vanishes when the leading edge is perpendicular to the impinging flow.

Infinitesimal perturbations (u, v, w, p) periodic in the spanwise $z-$direction with a spanwise wavenumber k are superimposed on this steady base flow. The perturbation energy is taken to be

$$E = \frac{1}{2}\int_{y>0} \lambda_E(x)(u^2 + v^2 + w^2)\ dxdydz \tag{3.33}$$

where $\lambda_E(x)$ is a weighing function. The reason for introducing λ_E is that swept Hiemenz flow is a degenerate model that does not take into account the leading-edge curvature. In particular the chordwise velocity U increases linearly away from the attachment-line. The proper way to avoid this singularity is to include a Gaussian energy weight in x as in Obrist and Schmid (2003a). In addition to focusing on the perturbations of most interest which are located close to the attachment-line, a Gaussian weight function finds its mathematical justification in that it defines a proper scalar product for Hermite polynomial decompositions in x, thereby allowing the comprehensive analysis of the stability equations (Obrist & Schmid 2003a). Here, the width of the Gaussian weight is ten times the boundary-layer thickness. It allows for a very rich dynamical behaviour while ruling out disturbances that develop too far away from the attachment-line, where the relevance of the swept Hiemenz flow model becomes questionable.

A spectral numerical scheme closely inspired from the one used by Obrist & Schmid (2003b) to study the receptivity of the boundary layer has been implemented to solve the perturbation equations. It involves Chebyshev polynomials in the wall-normal direction and two Fourier transforms of the disturbances in the spanwise and chordwise directions. The latter requires periodic boundary conditions that are obtained by introducing a fringe region which smoothly drives disturbances to zero at $\pm x_{max}$.

Optimization

The initial perturbation with an energy which is the most amplified over a finite time span $0 < t < T$ is called the optimal perturbation. It maximizes the objective functional

$$\mathcal{I} = \frac{E(T)}{E(0)}\ . \tag{3.34}$$

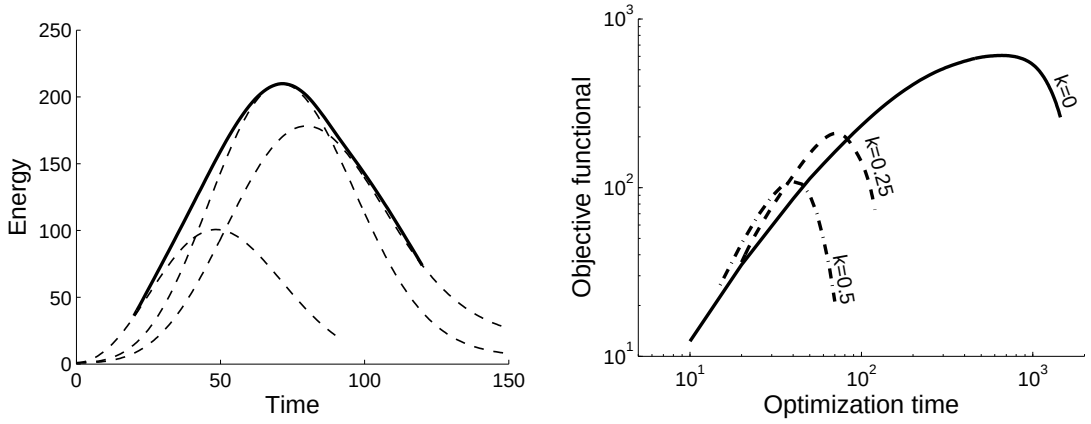

(a) (b)

Figure 3.3: (a) Time evolution of the perturbation energy for $k = 0.25$ optimal disturbances at times $T = 20,\ 70,\ 120$ (dashed), at a Reynolds number $Re = 550$. The envelope (solid) represents the maximum energy amplification that can be reached by $k = 0.25$ disturbances in the time interval $20 < t < 120$. (b) Maximum energy amplification in the time interval $15 < t < 1500$ for perturbations at $k = 0$ (solid), $k = 0.25$ (dashed), $k = 0.5$ (dash-dotted) and $Re = 550$.

A gradient algorithm described in Guégan *et al* (2006) was used to determine the maxima of $\mathcal{I}$. The energy amplification of an arbitrary initial disturbance is iteratively improved by computing the gradient of the objective functional with respect to the initial disturbance.

In the present study the optimization algorithm is initialized with an initial disturbance in the shape of a random vorticity patch. After less than a dozen iterations, each additional iteration improves the objective functional by less than 10^{-4} times its current value, at which point the algorithm is considered to have converged. It should be mentioned that the algorithm consistently converges to the same solution starting from a variety of initial guess values, which tends to show that a global maximum is reached independently from the initial guess disturbance.

3.4.3 Three-dimensional optimal disturbances

Transient energy growth

Figure 3.3a displays the energy growth of the $k = 0.25$ perturbations which yield optimal amplification at times $T = 20,\ 70,\ 120$, for a Reynolds number $Re = 550$.

The envelope of all energy curves represents the maximum energy amplification that $k = 0.25$ disturbances may experience at time T at this Reynolds number. The growth is seen to be maximum at $T_{max} = 72$ where the energy of the optimal perturbations experiences a total gain of $G_{max} = 210$.

The envelopes of the energy curves for spanwise wavenumbers $k = 0$, $k = 0.25$ and $k = 0.5$ are displayed in Figure 3.3b. The maximum energy growth G_{max} and the associated time T_{max} both decrease with wavenumber k. The maximum amplification is observed for homogeneous perturbations in the spanwise $z-$direction in which case the energy growth is $G_{max} = 600$ at $T_{max} = 675$. It should be emphasized that perturbations at non-zero wavenumbers must not be discarded since they are more amplified than homogeneous ones on shorter time scales.

Optimal perturbations structure

The optimal homogeneous perturbation consists of spanwise vortices identified with the Q-criterion (Hunt et al. (1988)) and displayed in Figure 3.4a. The initial disturbance almost exclusively consists of spanwise vorticity, as shown in Figure 3.5a. Through a mechanism similar to the lift-up mechanism (Landahl (1980)) high-spanwise momentum fluid is pushed toward the wall, and low-spanwise momentum fluid is pulled away from the wall as shown in Figure 3.6. Positive spanwise perturbation velocity w is created where the jet between two spanwise vortices is directed toward the wall; outward jets generate negative w. As a consequence wall-normal ω_y- and chordwise ω_x-vorticity components are amplified and dominate over the spanwise ω_z-vorticity component at the time when the energy is maximum (Figure 3.5b). Due to the stretching induced by the base flow the disturbances initially localized about the flow-dividing plane $x = 0$ spread in the chordwise $x-$direction. This phenomenon is not observed in the paradigmatic lift-up configuration in a two-dimensional boundary layer, where the perturbation takes the shape of streamwise vortices periodically spaced in the transverse direction.

At finite k the optimal disturbances take the shape of spanwise vortices meandering in the wall-normal direction as displayed in Figure 3.4c. At the maximum amplification time $T = 72$ the vortices are wider and more intense (Figure 3.4d). Isosurfaces of the vorticity components displayed in Figure 3.7a reveal elongated structures initially bent against the spanwise shear W' as in Hoepffner *et al* (2005). The structures are initially bent in the direction of the weaker chordwise shear, which also seems to be the case in Hoepffner *et al*, but no explanation could be found as for why this leads to optimal energy growth.

When the perturbation energy is maximal (Figure 3.7b) the structures have flipped over and are bent in the same direction as the spanwise shear but in the

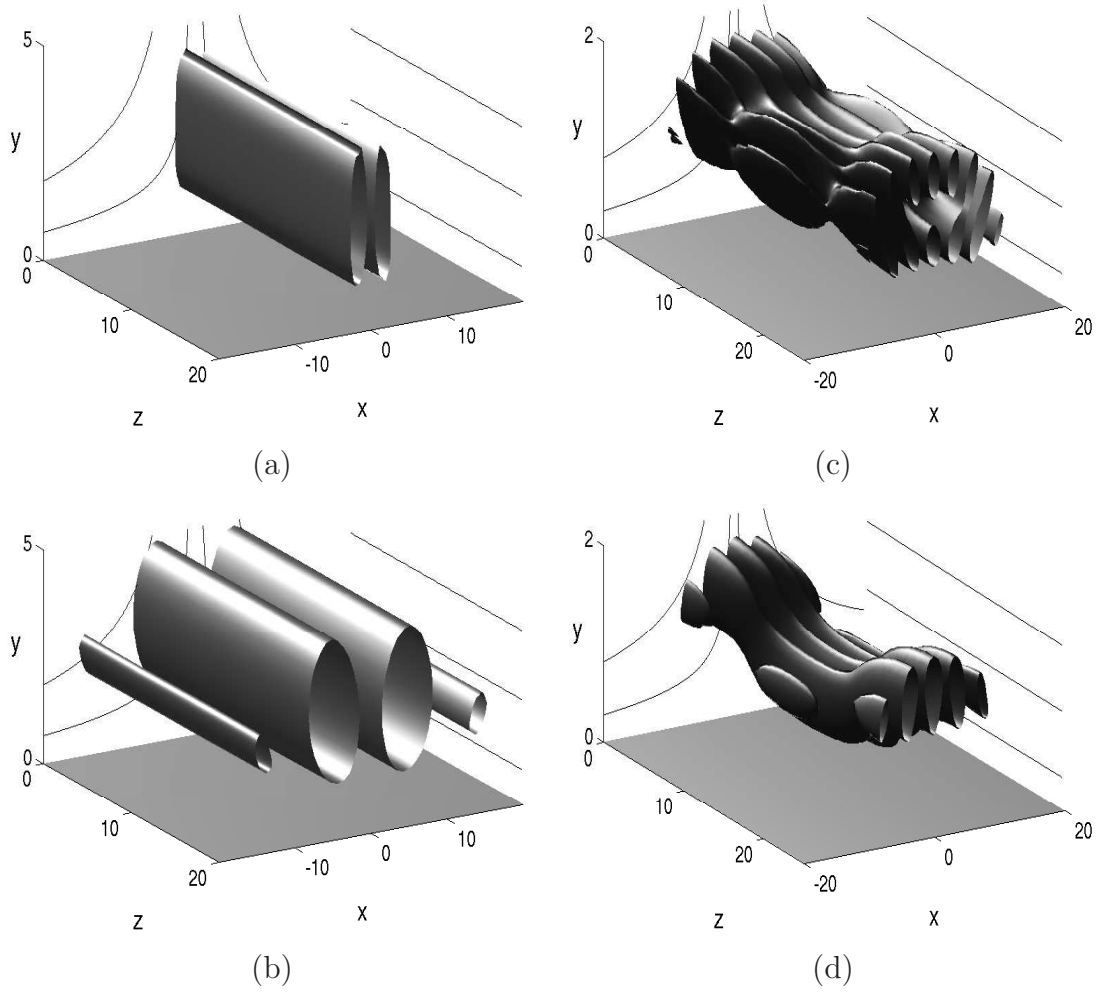

Figure 3.4: Homogeneous $k = 0$ optimal perturbations at $t = 0$ (a) and at maximum amplification time $T = 675$ (b) and periodic $k = 0.25$ optimal perturbations at $t = 0$ (c) and at maximum amplification time $T = 72$ (d), identified with the Q-criterion method. The isosurfaces are located at 20% of the maximum of $Q = \frac{1}{2}(\Omega_{ij}\Omega_{ij} - S_{ij}S_{ij})$ where Ω_{ij} and S_{ij} are the components of the vorticity and rate of strain tensor respectively. The Reynolds number is $Re = 550$.

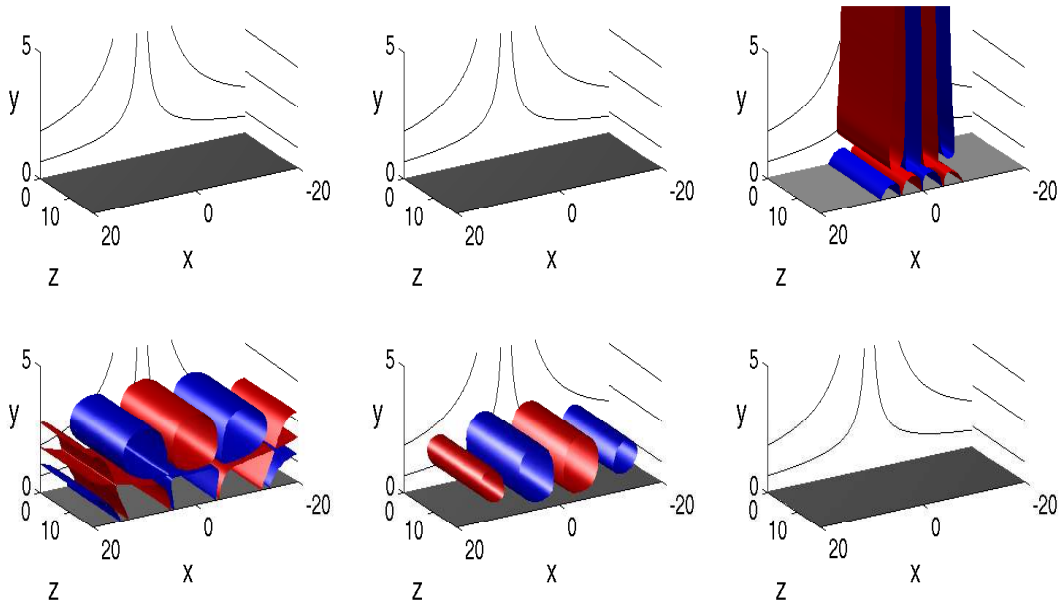

Figure 3.5: From left to right, chordwise, wall-normal and spanwise vorticity components of homogeneous $k = 0$ optimal perturbations at $t = 0$ (a) and at maximum amplification time $T = 675$ (b). The isosurfaces correspond to 0.1 (red) and -0.1 (blue) times the maximum of the strongest vorticity component. At $t = 0$ the vorticity maxima are $\omega_{x0} = 0$, $\omega_{y0} = 0.01$, $\omega_{z0} = 1$, and at $t = T$, $\omega_{xT} = 23.8$, $\omega_{yT} = 6.5$, $\omega_{zT} = 0.7$. The Reynolds number is $Re = 550$.

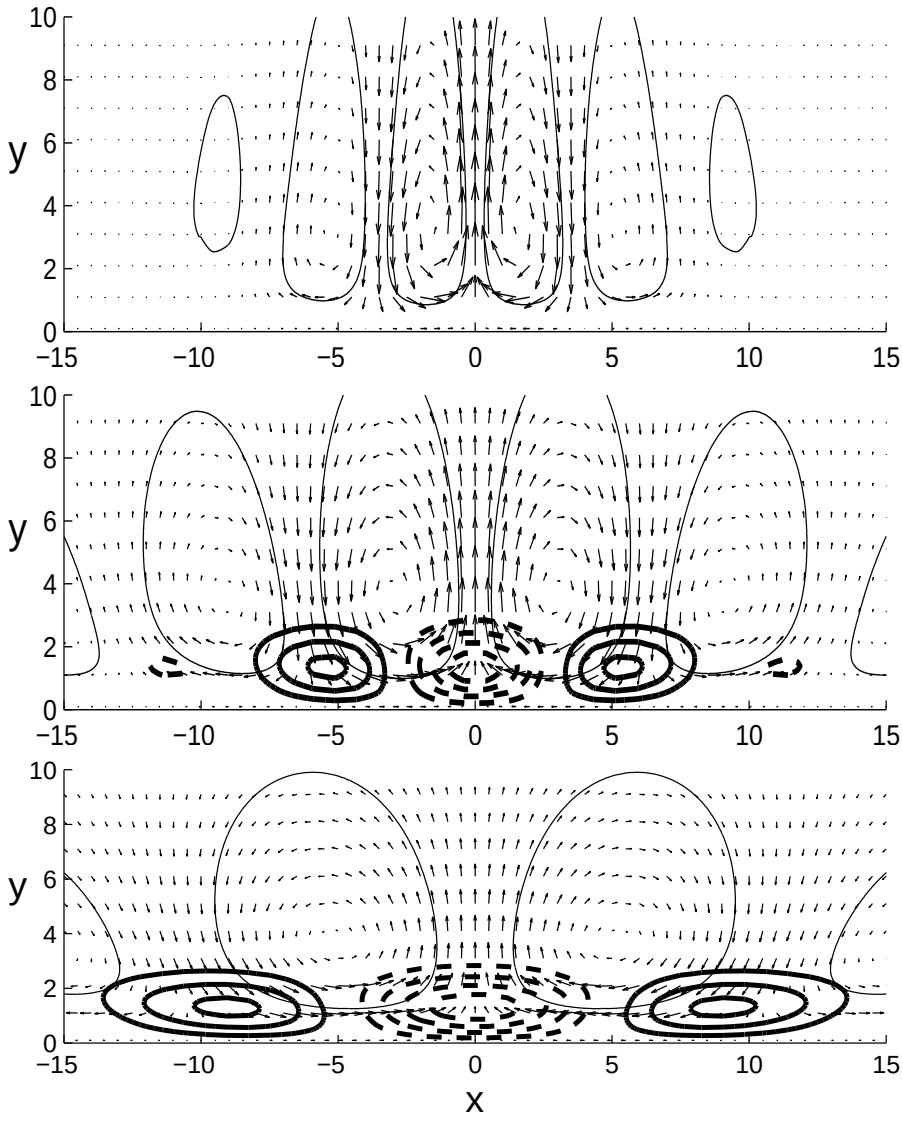

Figure 3.6: Vector plot of the chordwise and wall-normal (u, v) velocity components in the $x-y$ plane and contours of spanwise perturbation velocity w for a homogeneous $k = 0$ optimal perturbation. The snapshots are taken at time $t = 0$ (a), $t = 333$ (b) and at maximum amplification time $T = 675$ (c). Positive (negative) values of w are displayed in thick solid (dashed) lines, and the contour levels and vector scale are the same in all three plots. To guide the eye, one streamline of each spanwise vortex is displayed as a thin solid line. The Reynolds number is $Re = 550$.

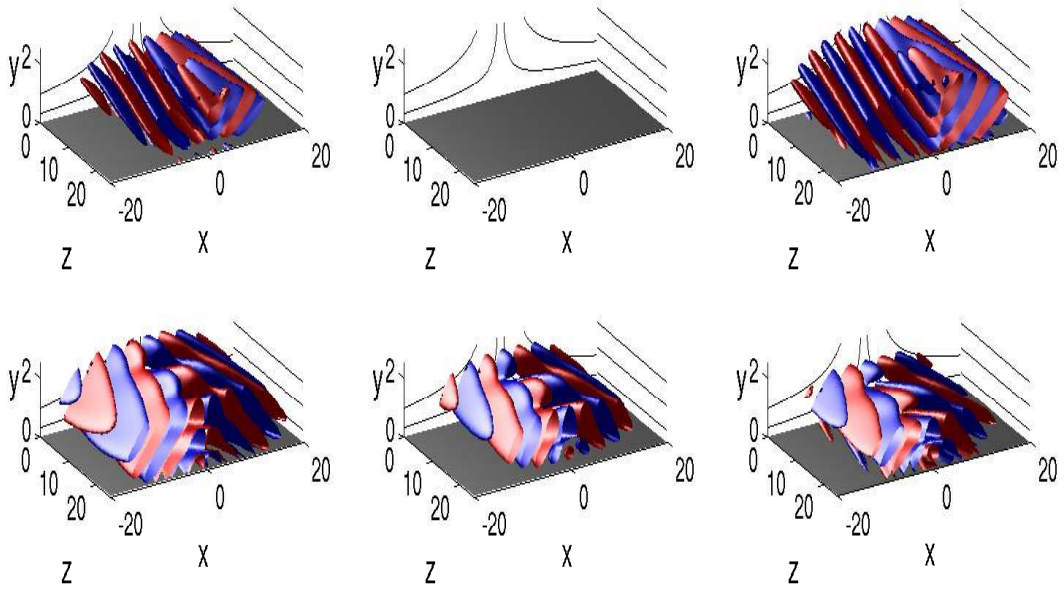

Figure 3.7: From left to right, chordwise, wall-normal and spanwise vorticity components of $k = 0.25$ optimal perturbations at $t = 0$ (a) and at maximum amplification time $T = 72$ (b). The isosurfaces correspond to 0.1 (red) and -0.1 (blue) times the maximum of the strongest vorticity component. At $t = 0$ the vorticity maxima are $\omega_{x0} = 0.31$, $\omega_{y0} = 0.01$, $\omega_{z0} = 1$, and at $t = T$, $\omega_{xT} = 9.4$, $\omega_{yT} = 3.9$, $\omega_{zT} = 3.3$. The Reynolds number is $Re = 550$.

direction opposite to the chordwise shear. The chordwise vorticity component ω_x is the most amplified in the process.

3.4.4 Discussion

Perturbation energy equation

To further analyse the amplification mechanism one may extract the production and the dissipation terms from the energy equation. The time derivative of the total perturbation energy reads

$$\partial_t E = \int_{y>0} \lambda_E(-wv\partial_y W - uv\partial_y U + Re^{-1}\mathbf{u}.\Delta\mathbf{u} - \mathbf{u}.\mathbf{U}\nabla\mathbf{u} - \partial_x U u^2 - \partial_y V v^2)\; dxdydz\;. \tag{3.35}$$

The stretching direction x and the sweep direction z are associated with the production terms $-uv\partial_y U$ and $-wv\partial_y W$ displayed in Figure 3.8a along with the dissipation term $Re^{-1}\mathbf{u}\Delta\mathbf{u}$ and the time derivative of the energy $\partial_t E$. The energy amplification may be mainly attributed to the spanwise production term $-wv\partial_y W$ balanced by the dissipation term $Re^{-1}\mathbf{u}\Delta\mathbf{u}$ while the chordwise production term $-uv\partial_y U$ and the other remaining terms are negligible.

A parallel can be drawn between the present analysis and the study of Hoepffner *et al* (2005), who computed optimal perturbations of boundary-layer streaks. In both configurations the advection is stronger in a particular direction, respectively the direction of the streaks (referred to as the "x" direction) or the direction of the sweep (denoted by z throughout the present study), which thus defines a preferential downstream direction. As in the present case, Hoepffner *et al* (2005) observe that the optimal perturbation with a finite streamwise wavenumber is initially tilted against the main shear and points downstream when its energy is maximum. The main contributor to the energy amplification in their study is the term "$-uw\partial_z U$". The equivalent term here would read $-wu\partial_x W$ but since the sweep W is homogeneous in the chordwise x direction, it is equal to zero. The other production term "$-uv\partial_y U$" in the streaky base flow contributes moderately to the energy growth but its counterpart $-wv\partial_y W$ is responsible for most of the amplification in swept Hiemenz flow. The chordwise production term $-uv\partial_y U$ has a counterpart "$-wv\partial_y W$" which is zero in the boundary layer with streaks. Here it is negligible.

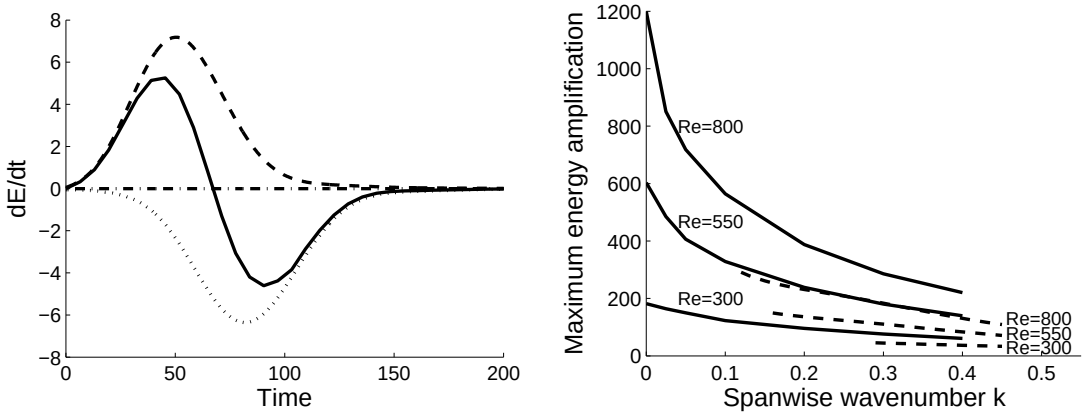

(a) (b)

Figure 3.8: (a) Temporal evolution of the time derivative of the energy ($\partial_t E$, solid), of the viscous dissipation ($Re^{-1}\mathbf{u}\Delta\mathbf{u}$, dotted line) and of the two production terms $-uv\partial_y U$ (dash-dotted line) and $-wv\partial_y W$ (dashed line), for the optimal disturbance at $Re = 550$, $k = 0.25$, $T = 70$. (b) Maximum energy growth of Görtler-Hämmerlin (dashed lines) and general optimal perturbations (solid lines) as a function of spanwise wavenumber k, for different Reynolds numbers.

Transient growth mechanisms

Two distinct mechanisms are classically held responsible for energy amplification in shear flows, namely the Orr mechanism (Orr (1907)) and the lift-up mechanism (Landahl (1980)). In the Orr mechanism counter-rotating vortices parallel to the main stream vorticity and tilted against the mean shear are amplified by the basic shear; this mechanism is efficient at high streamwise wavenumbers, on short time scales as demonstrated by Butler & Farrell (1992). In the so-called lift-up mechanism streamwise vortices interact with the basic shear to generate streamwise perturbation velocity; this mechanism operates at smaller wavenumbers, on larger time scales (Butler and Farrell (1992)). At medium wavenumbers both mechanisms work in conjunction and the optimal perturbation is a combination of streamwise and transverse vorticity.

Figure 3.9a displays the ratio of the initial chordwise enstrophy $\int_{XYZ} \omega_x^2(t = 0)\, dxdydz$ over the initial spanwise enstrophy $\int_{XYZ} \omega_z^2(t = 0)\, dxdydz$ for optimal disturbances at different spanwise wavenumbers k, and $Re = 550$. This ratio gives a complete picture of the balance between vorticity components in the initial disturbance since the wall-normal vorticity component accounts for less than 1% of the total enstrophy at all wavenumbers investigated. At zero spanwise wavenumber the

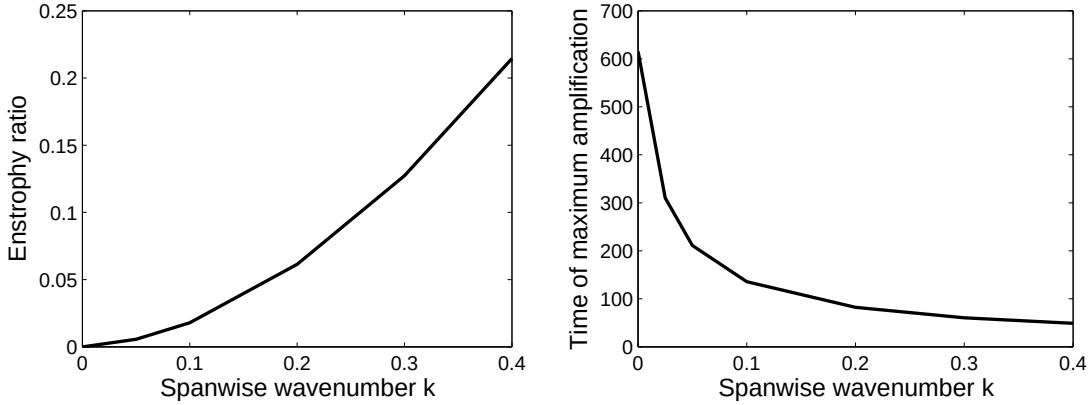

(a) (b)

Figure 3.9: (a) Ratio of the initial enstrophy $\int_{XYZ} \omega_x^2(t=0)\, dxdydz$ associated with vorticity in the chordwise x direction, divided by initial enstrophy $\int_{XYZ} \omega_z^2(t=0)\, dxdydz$ associated with vorticity in the spanwise z direction, versus spanwise wavenumber k. The chordwise vorticity component of the optimal perturbation increases with k compared to the spanwise component and the maximum amplification time decreases with k. (b) Optimal perturbation amplification time versus k. It is maximum at $k = 0$. The Reynolds number is $Re = 550$.

chordwise $x-$enstrophy is negligible compared to the spanwise $z-$enstrophy, and the optimal perturbation consists of spanwise vortices, in line with the results of Butler & Farrell (1992). As the spanwise wavenumber k is increased the chordwise ω_x-component accounts for an increasing fraction of the initial enstrophy; at $k = 0.4$ the chordwise $x-$enstrophy is a fifth of the spanwise $z-$enstrophy.

Chordwise vorticity amplification via an Orr-like mechanism clearly gains ground on lift-up as k is increased. Consistently (Butler & Farrell 1992), the maximum amplification time dramatically decreases as k is increased from $k = 0$ to $k = 0.4$ (Figure 3.9b).

Comparison with Görtler-Hämmerlin disturbances

Optimal Görtler-Hämmerlin perturbations consist of chordwise vortices amplified by a two-dimensional mechanism reminiscent of the Orr mechanism (Guégan *et al* 2006). At high spanwise wavenumbers k general optimal disturbances are amplified by the same type of mechanism. The amplification levels displayed in Figure 3.8b are of the same order of magnitude as those of Görtler-Hämmerlin optimal perturbations for $k > 0.1$, and the optimal energy amplification has a similar k-dependence. Note

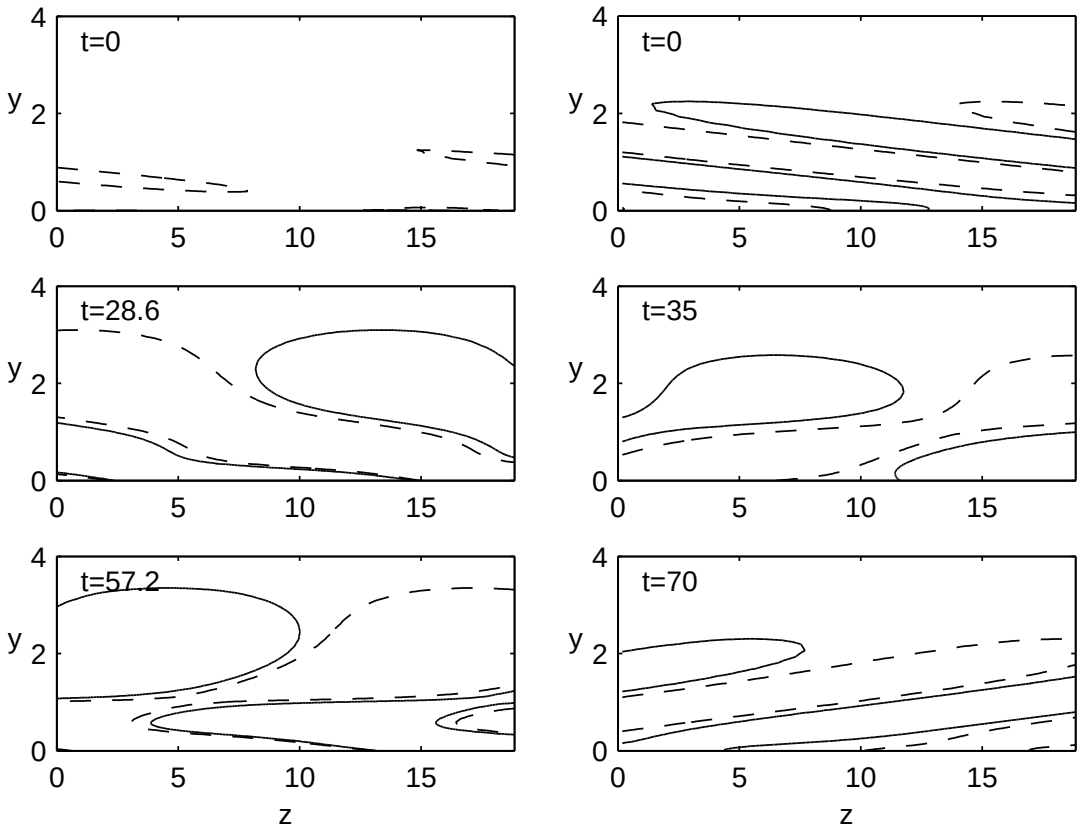

(a) (b)

Figure 3.10: Chordwise vorticity contours in $z-y$ plane of (a) an optimal Görtler-Hämmerlin perturbation and (b) a general optimal perturbation at $k = 0.25$ and $Re = 550$. The successive snapshots have been taken (from top to bottom) at times $t = 0$, $t = T/2$ and $t = T$. For visualization convenience the levels have been set at 2% and 20% of the maximum chordwise vorticity in (a) and (b) respectively.

that a strict quantitative comparison cannot be made since amplification in the Görtler-Hämmerlin case is defined with a top-hat weight function in the chordwise direction (Guégan *et al* 2006).

Chordwise vorticity contours in $z - y$ planes (Figure 3.10b) display similar features as optimal Görtler-Hämmerlin disturbances (Figure 3.10a), although on shorter time scales. In the latter case an array of counter-rotating chordwise vortices initially bent against the spanwise shear eventually tilts in the direction of the shear. Similarly in the general case, optimal perturbations are initially bent against the spanwise shear (Figure 3.10b, $t = 0$ snapshot) and tilt in the direction of the shear (Figure 3.10b, $t = 70$ snapshot). For intermediate times (Figure 3.10b, $t = 35$ snapshot) the occasional vortex splitting observed by Guégan *et al* (2006) is recovered as well.

The Görtler-Hämmerlin assumption has been extensively used in the past, and it is here demonstrated to yield realistic energy amplification levels for spanwise wavenumbers $k > 0.1$ and short time scales. The optimal mechanism at finite k consists partly in amplification of the chordwise vorticity by the main shear W' in a similar way as optimal Görtler-Hämmerlin perturbations. However, in order to obtain the true shape of the optimal perturbations, it is necessary to relax the Görtler-Hämmerlin assumption: the optimal perturbations take the shape of spanwise vortices (Figure 3.4a) whereas their Görtler-Hämmerlin counterparts consist of chordwise vortices. For similar reasons, the lift-up mechanism and the high amplification levels at $k = 0$ can only be observed if the Görtler-Hämmerlin assumption has been relaxed.

Acknowledgments

The authors would like to thank C. Cossu for discussions on transient growth mechanisms. Alan Guégan holds a PhD fellowship from CNRS and the French "Délégation Générale pour l'Armement"; this study has also been supported by Airbus.

Chapter 4

Optimal spatial perturbations

4.1 Introduction

From a theoretical point of view, temporally evolving disturbances are usually easier to investigate than spatially developing perturbations. Unfortunately, physical configurations that can be described in a temporal framework are seldom found, whereas spatially developing flows are ubiquitous (see, e.g. a nice example of spatially developing disturbances in hot jets in Lesshafft (2006)).

In the spatial framework a base flow dominated by advection in the streamwise $x-$direction is submitted to upstream excitations at, say, $x = 0$. Disturbances develop downstream of the forcing location. In the spatial context optimal disturbances are the perturbations whose energy is amplified most between the location of the periodic forcing $x = 0$ and a given output location $x_{max} > 0$. Our objective in this chapter is to compute optimal spatial disturbances in swept Hiemenz flow.

Performing spatial computations is not as straightforward as computing the temporal evolution of an initial disturbance. In the temporal context, causality ensures that a given initial condition u_0, v_0, w_0, p_0 will result in a unique disturbance at later times. In the spatial framework, a localized forcing in a plane orthogonal to the main advection direction will give rise to both upstream- and downstream-travelling waves. This is due to the elliptic part $\frac{1}{Re}\partial_{xx}(u, v, w)$ in the linearized Navier-Stokes equations; the second streamwise derivative allows information travelling upstream of the forcing location. In order for the objective functional $\mathcal{I} = \frac{E(Z)}{E(0)}$ to be uniquely defined one has to be able to compute the unique downstream-travelling wave associated to a given velocity input u_0, v_0, w_0. Otherwise, an infinite number of combinations between upstream- and downstream-travelling disturbances may be associated

to the same velocity input u_0, v_0, w_0, with distinct spatial energy amplifications.

One possibility is to force disturbances u_0, v_0, w_0 upstream of the computational domain and let them free to evolve in time and to develop downwstream of the forcing location. The perturbations eventually reach a steady state in the domain of interest $0 < x < L$. Besides the fact that forcing arbitrary disturbances in the DNS code described in chapter 3 is itself problematic (see Appendix), the procedure would be extremely expensive in terms of computer time since the three-dimensional perturbation equations would have to be solved several times over long time intervals.

Another way to achieve downstream-travelling disturbances is to use parabolized equations (see e.g. Andersson et al. (1999), Luchini (2000)). Parabolization of the linearized Navier-Stokes equations is justified when optimal perturbations are sought in the shape of streamwise elongated structures that vary slowly in the streamwise direction; a major advantage of parabolic equations is that upstream-travelling waves are discarded and downstream disturbances are uniquely defined by the upstream forcing. Furthermore, disturbances can be computed by a one-shot marching scheme starting from the upstream velocity input (u_0, v_0, w_0). The computational cost is dramatically reduced compared to, e.g., solving the entire three-dimensional Navier-Stokes equations over a time interval large enough so that perturbations have had time to settle.

At reasonably high Reynolds numbers and close to the attachment line, swept Hiemenz flow is dominated by spanwise advection. Consequently, optimal temporal disturbances are highly elongated in the spanwise direction (see section 3.4.3). By extension, optimal spatial perturbations developing in the spanwise $z-$direction are also expected to be elongated in the spanwise direction and optimal disturbances will be computed with perturbation equations parabolized in the spanwise $z-$direction.

In this chapter we first demonstrate in section 4.2 that parabolization does not significantly alter results on optimal disturbances for a model system based on the Ginzburg-Landau equation. In section 4.3 the parabolized perturbation equations for swept Hiemenz flow are derived; the adjoint system and the numerical scheme are described in detail. To validate the code and the optimization procedure swept Hiemenz flow is replaced in section 4.4 by the parallel Blasius velocity profile. Optimal perturbations are computed for the Blasius velocity profile and compared with the results of Andersson et al. (1999), Luchini (2000) and Tumin and Reshotko (2001). Optimal energy growth and optimal spatial disturbances for swept Hiemenz flow are computed in section 4.5.

4.2 Spatial energy amplification and the Ginzburg-Landau equation

Many features of the linear stability of open shear flows (see, e.g., Huerre (2000)) are captured by the one-dimensional linear Ginzburg-Landau equation

$$\partial_t \phi + U \partial_x \phi - \mu \phi - \frac{1}{Re} \partial_{xx} \phi = 0 \ . \tag{4.1}$$

For instance, the steady spatial Ginzburg-Landau equation

$$U \partial_x \phi - \mu \phi - \frac{1}{Re} \partial_{xx} \phi = 0 \tag{4.2}$$

may be used to investigate the spatial stability of steady, spatially-developing disturbances. Transient spatial growth phenomena cannot be observed with equation (4.2). Depending on parameters U, μ, Re, the energy of steady disturbances

$$E(x) = \phi^*(x)\phi(x) \tag{4.3}$$

increases or decreases exponentially from $x = 0$ to infinity as shown in Figure 4.1a.

We would like to study optimal energy amplification in the spatial framework; the Ginzburg-Landau equation needs to be modified in order to display transient growth. For this purpose, one may introduce the new variable ψ coupled with ϕ through the additional equation

$$U \partial_x \psi + \psi = \phi \ . \tag{4.4}$$

The new variable ψ is governed by the stable spatial equation $U\partial_x\psi + \psi = 0$ forced by ϕ. For simplicity, ψ is set equal to zero at $x = 0$. The two-equation model problem

$$U \partial_x \phi - \mu \phi - \frac{1}{Re} \partial_{xx} \phi = 0 \ , \tag{4.5a}$$

$$U \partial_x \psi + \psi - \phi = 0 \ , \tag{4.5b}$$

is non-normal due to the coupling term ϕ in equation (4.5b). As shown in Figure 4.1b, the total energy

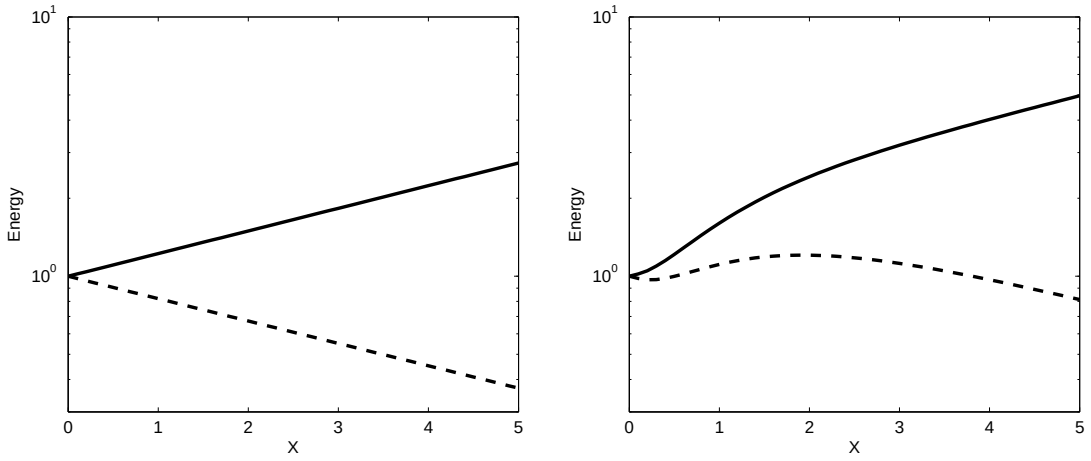

(a) (b)

Figure 4.1: Total energy versus streamwise $x-$coordinate for the one-dimensional, steady Ginzburg-Landau equation (left) and the model problem (4.5) (right). The latter displays transient growth whereas the Ginzburg-Landau equation does not. The parameters are : $U = 1$, $Re = 100$, $\mu = 0.1$ (solid lines) and $\mu = -0.1$ (dashed lines).

$$E(x) = \phi^*(x)\phi(x) + \psi^*(x)\psi(x) \tag{4.6}$$

grows transiently in space when the damping parameter μ is negative.

Since equations (4.5a,b) are linear the solution $\phi(x)$ is defined by the value ϕ_0 up to a muliplicative factor which is divided out in the objective functional

$$\mathcal{I} = \frac{E(L)}{E(0)} \ . \tag{4.7}$$

As a consequence, energy amplification $\mathcal{I}$ depends only on the parameters U, μ and Re.

Optimization is made non-trivial by introducing a spanwise $z-$coordinate. Variables ϕ and ψ are taken to be functions of z and the advection velocity U is set equal to:

$$U(z) = U_{max}\left(1 + \frac{1}{2}\,\sin(\frac{2\pi z}{z_{max}})\right) \tag{4.8}$$

with z_{max} as a spanwise reference length. The two-dimensional model system takes the form

$$U(z)\partial_x\phi - \mu\phi - \frac{1}{Re}(\partial_{xx} + \partial_{zz})\phi = 0 \ , \tag{4.9a}$$

$$U(z)\partial_x\psi + \psi - \phi = 0 \ , \tag{4.9b}$$

and energy is redefined as

$$E(x) = \int_z (\phi^*(x,z)\phi(x,z) + \psi^*(x,z)\psi(x,z)) \ dz \ . \tag{4.10}$$

The optimization problem now consists in maximizing the energy amplification

$$\mathcal{I} = \frac{\int_z (\phi^*(L,z)\phi(L,z) + \psi^*(L,z)\psi(L,z))dz}{\int_z (\phi_0(z)^*\phi_0(z))dz} = \frac{E_L}{E_0} \tag{4.11}$$

with respect to the condition at the entrance

$$\phi(x=0,z) = \phi_0(z) \ . \tag{4.12}$$

The objective functional $\mathcal{I}(\phi_0)$ is evaluated by computing the steady disturbance ϕ, ψ that satisfies equations (4.9a,b) with initial condition $\phi(x=0,z) = \phi_0, \ \psi(x=0,z) = 0$. Transient growth phenomena are preserved and the optimization is still non-trivial under the assumptions that the coupled variable ψ is zero at $x = 0$ and that all variables are periodic in z.

In order to select only the downstream-travelling waves the objective functional is evaluated by computing long-term solutions of the signalling problem

$$\partial_t\phi + U(z)\partial_x\phi - \mu\phi - \frac{1}{Re}(\partial_{xx} + \partial_{zz})\phi = 0 \ , \tag{4.13a}$$

$$\partial_t\psi + U(z)\partial_x\psi + \psi - \phi = 0 \tag{4.13b}$$

with initial and boundary conditions

$$\phi(x=0,z,t) = H(t)\phi_0(z) \ , \tag{4.14a}$$

$$\psi(x=0,z,t) = 0 \ , \tag{4.14b}$$

$$\partial_x\phi(x\to\infty,z,t) = 0 \ . \tag{4.14c}$$

The resulting optimal spatial perturbations can be compared to the optimal spatial perturbations for the parabolized problem

$$U(z)\partial_x\phi - \mu\phi - \frac{1}{Re}\partial_{zz}\phi = 0 \ , \tag{4.15a}$$

$$U(z)\partial_x\psi + \psi - \phi = 0 \tag{4.15b}$$

where the second streamwise derivative has been dropped. The initial and boundary conditions for the parabolized problem read:

$$\phi(x = 0, z) = \phi_0(z) \ , \tag{4.16a}$$

$$\psi(x = 0, z) = 0 \ . \tag{4.16b}$$

4.2.1 Parabolized versus non-parabolized spatially developing perturbations

Setting up the spatial optimization problem

Let us consider the following objective functional

$$\mathcal{I} = \frac{\int_z (\phi^*(L)\phi(L) + \psi^*(L)\psi(L))dz}{\int_z \phi_0^*\phi_0 dz} = \frac{E_L}{E_0} \tag{4.17}$$

which represents the energy amplification between streamwise locations $x = 0$ and $x = L$. Let us assume that the variables ϕ, ψ are solutions to the parabolized (respectively, genuine steady perturbation) equations (4.15a,b) (resp. (4.9a,b) with initial condition $\phi(x = 0, z) = \phi_0(z)$, $\psi(x = 0, z) = 0$. Similar to the temporal optimization performed in chapters 2 and 3 the optimal condition ϕ_0^{opt} is determined iteratively from an initial guess value ϕ_0^0 using a steepest descent algorithm. Each iterate of the optimization loop reads

$$\phi_0^{k+1} = \phi_0^k + \alpha_{opt}^{k+1}\nabla\mathcal{I} \ . \tag{4.18a}$$

The optimal descent parameter α_{opt}^{k+1} is found by a line search algorithm. Our model (4.9) has few degrees of freedom and the gradient $\nabla\mathcal{I}$ can either be derived analytically, as in Andersson et al. (1999), or evaluated numerically as in Cossu et al. (2000).

Gradient evaluation for the parabolized case

For the parabolized case, the gradient can be derived analytically and evaluated from the computation of an adjoint problem. Equations (4.15) are re-written as

$$F(\Phi) = \left\{ \begin{array}{c} U(z)\partial_x\phi - \mu\phi - \frac{1}{Re}\partial_{zz}\phi \\ U(z)\partial_x\psi + \psi - \phi \end{array} \right\}, \tag{4.19a}$$

$$G(\Phi, \phi_0) = \phi(x = 0, z) - \phi_0(z) \ , \tag{4.19b}$$

with $\Phi = (\phi, \psi)$. The Lagrangian

$$\mathcal{L} = \mathcal{I} - \left(F(\Phi), \tilde{\Phi}\right) - \left[G(\Phi, \phi_0), \tilde{\phi}_0\right] \tag{4.20}$$

is introduced, using the scalar products

$$\left(F(\Phi), \tilde{\Phi}\right) = \int_z \int_0^L F(\Phi)^* \tilde{\Phi} dx dz \ , \tag{4.21a}$$

$$\left[G(\Phi, \phi_0), \tilde{\phi}_0\right] = \int_z G(\Phi, \phi_0)^* \tilde{\phi}_0 dz \ . \tag{4.21b}$$

Differentiating the Lagrangian with respect to ϕ_0 yields

$$\partial_{\phi_0}\mathcal{L}\delta\phi_0 = -2\frac{E_L}{E_0^2}\int_z \delta\phi_0^*\phi_0 dz + \int_z \delta\phi_0^*\tilde{\phi}_0 dz \ , \tag{4.22a}$$

from which one obtains the gradient of the objective functional with respect to the initial condition

$$\nabla_{\phi_0}\mathcal{I} = -2\frac{E_L}{E_0^2}\phi_0 + \tilde{\phi}_0 \ . \tag{4.23a}$$

Differentiating the Lagrangian with respect to Φ yields

$$
\begin{aligned}
\partial_\Phi \mathcal{L}\delta\Phi &= \frac{2}{E_0}\int_z \begin{pmatrix} \delta\phi^*(L)\phi(L) \\ \delta\psi^*(L)\psi(L) \end{pmatrix} dz - \int_z \delta\phi^*(x=0)\tilde{\phi}_0 dz \\
&\quad - \int_z \Big[\begin{matrix} U\delta\phi^*\tilde{\phi} \\ U\delta\psi^*\tilde{\psi} \end{matrix} \Big]_0^L dz \\
&\quad + \int_z \int_0^L \begin{pmatrix} \delta\phi^* \\ \delta\psi^* \end{pmatrix} \begin{pmatrix} U(z)\partial_x\tilde{\phi} + \mu\tilde{\phi} + \frac{1}{Re}\partial_{zz}\tilde{\phi} + \psi \\ U(z)\partial_x\psi - \psi \end{pmatrix} dx\ dz\ . \qquad (4.24a)
\end{aligned}
$$

The adjoint equations arising from the last integral reads:

$$
\begin{aligned}
U(z)\partial_x\tilde{\phi} + \mu\tilde{\phi} + \frac{1}{Re}\partial_{zz}\tilde{\phi} + \psi &= 0\ , \qquad (4.25a) \\
U(z)\partial_x\psi - \psi &= 0\ . \qquad (4.25b)
\end{aligned}
$$

The boundary terms that involve $\delta\phi(x=0)$ yield an equation for $\tilde{\phi}_0$,

$$
\tilde{\phi}_0 = U\tilde{\phi}(x=0)\ . \qquad (4.26a)
$$

The boundary terms that involve $\delta\phi(L),\ \delta\psi(L)$ yield the adjoint conditions at $x=L$:

$$
\begin{aligned}
U\tilde{\phi}(L) &= \frac{2}{E_0}\phi(L)\ , \qquad (4.27a) \\
U\tilde{\psi}(L) &= \frac{2}{E_0}\psi(L)\ . \qquad (4.27b)
\end{aligned}
$$

Finally, the gradient of the objective functional (4.17) with respect to the initial condition ϕ_0 reads

$$
\nabla_{\phi_0}\mathcal{I} = -2\frac{E_L}{E_0^2}\phi_0 + U\tilde{\phi}(x=0)\ , \qquad (4.28)
$$

where the adjoint variable $\tilde{\phi}(x=0)$ satisfies the adjoint equations

$$
\begin{aligned}
U(z)\partial_x\tilde{\phi} + \mu\tilde{\phi} + \frac{1}{Re}\partial_{zz}\tilde{\phi} + \psi &= 0\ , \qquad (4.29a) \\
U(z)\partial_x\psi - \psi &= 0\ , \qquad (4.29b)
\end{aligned}
$$

with downstream conditions

$$U\tilde{\phi}(L) = \frac{2}{E_0}\phi(L) \ , \tag{4.30a}$$

$$U\tilde{\psi}(L) = \frac{2}{E_0}\psi(L) \ . \tag{4.30b}$$

Gradient evaluation in the non-parabolized case

It has been argued in section 4.1 that in the non-parabolized case perturbations to develop from the upstream forcing location $x = 0$ to a downstream $x-$location until a steady state has been reached between $x = 0$ and $x = L$.

In order to prevent any contamination of the flow between $x = 0$ and $x = L$ by the downstream boundary condition the computational domain should extend some distance downstream of $x = L$. In this case, it is difficult to match the output measure of the energy at $x = L$ with an explicit boundary condition at $x = L$.

As an alternative, it should be possible to prescribe more complex boundary conditions at $x = L$ that select outgoing waves only. Deriving an adjoint problem under such conditions is not straightforward, since the treatment of boundary terms at $x = L$ is considerably more involved than in the parabolized case.

Taking a different approach, the gradient can be evaluated numerically. The value of the gradient at each discretization point z_n can be evaluated by changing slightly each component of the guess value ϕ_0^k separately, computing ϕ and ψ, and tracing the subsequent changes in the objective functional. For instance, if the k^{th} guess value ϕ_0^k is increased by $\delta\phi_{0,n} \ll 1$ at spanwise discretization point n, the n^{th} component of the gradient at optimization loop k is equal to

$$\nabla^k_{\phi_0,n}\mathcal{I} = \frac{\mathcal{I}(\phi_0^k) - \mathcal{I}(\phi_0^k + \delta\phi_{0,n})}{\delta\phi_{0,n}} \ . \tag{4.31a}$$

The model equations (4.9) are two-dimensional and the upstream condition ϕ_0 is one-dimensional in space; evaluating ϕ, ψ between $x = 0$ and $x = L$ takes a fraction of a second on a standard PC for reasonable resolutions ($n_x = 100$ points in the streamwise $x-$direction and $n_z = 50$ in the spanwise $z-$direction). Evaluating the objective functional n_z times is affordable and an excellent numerical evaluation of the gradient can be obtained this way.

This method is very attractive since the adjoint problem is completely bypassed. It also yields excellent results in terms of convergence of the optimization algorithm since the error made computing the gradient is on the order of the PDE solver's error when small enough test variations $\delta\phi_{0,n}$ are considered.

The method has been used previously by Cossu et al. (2000) to compute optimal Görtler vortices periodically spaced in the transverse direction; however, it becomes impracticable as the dimension of the upstream forcing condition increases. For a two-dimensional upstream condition such as the one we are planning to investigate in swept Hiemenz flow, discretized on a 100×100 mesh, the gradient computation would require 10^4 evaluations of the objective functional, versus two evaluations for the adjoint-based technique.

Still, the low-dimensional parabolized and non-parabolized versions of the model (4.9a,b) can be compared using this technique. The parabolization assumption will be shown to have a negligible influence on the optimal spatial energy growth and the shape of the optimal spatial perturbations.

Results

The original model (4.9a,b) and its parabolized counterpart (4.15) are solved using a finite-difference scheme. For both models the objective functional is maximized with respect to the initial condition $\phi_0(z)$. The gradient of the objective functional is derived analytically from the parabolized equations and evaluated numerically in the non-parabolized case.

At all steps of the optimization procedure the non-parabolized equations should be solved as a signalling problem by forcing ϕ at $x = 0$ and letting it evolve in time until perturbations are steady between $x = 0$ and $x = L$. In order to speed up the procedure we take advantage of the fact that the streamwise derivatives of ϕ, ψ are expected to be small. We make a 'local parabolic assumption' by assuming zero derivatives at the inlet of the domain. Therefore, the non-parabolic equations can be solved at each time step by marching the equations in space from $x = 0$ to $x = L$, starting with $\phi(x = 0) = \phi_0$ and $\partial_x\phi(x = 0) = 0$, $\partial_x\psi(x = 0) = 0$. In order to check that this assumption does not significantly alter the solution we compare ϕ, ψ with the true signalling problem computed *a posteriori* with the optimal ϕ_0.

The objective functional displayed in Figure 4.2a increases with the number of optimization iterations from less than 0.2 to more than 1 in both the parabolized and the non-parabolized case, for parameters $U = 1$, $Re = 100$, $\mu = -0.05$, $L = 9$. When the optimization algorithm has converged both, energy amplifications differ by as little as one percent.

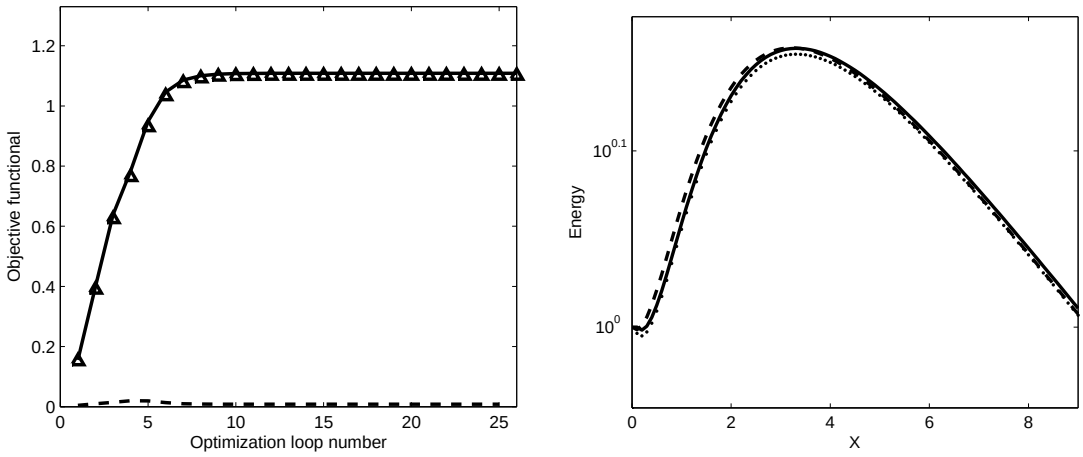

(a) (b)

Figure 4.2: (a) Objective functional versus the optimization iteration number for the parabolized (triangles) and the non-parabolized problem (solid line). The difference (dashed line) is on the order of one percent after the optimization has converged. (b) Energy evolution versus the streamwise $x-$coordinate for optimal disturbances of the parabolized (dashed line) and the non-parabolized problem (solid line). The energy amplification is almost identical in both cases and closely matches the signalling problem computed for comparison (dots). The parameters are : $U_{max} = 1$, $Re = 100$, $\mu = -0.05$, $L = 9$.

As shown in Figure 4.2b the energy of the optimal spatial perturbation increases transiently from $x = 0$ to $x = 4$; it eventually decays, consistent with the negative damping parameter $\mu = -0.05$. The signalling problem and the spatial equation solved with the assumption of a zero slope at the inlet yield almost identical energy evolutions, which confirms the validity of assuming zero-slope at $x = 0$. The energy of optimal perturbations in the parabolized system follows closely the energy of the full spatial problem from $x = 0$ to $x = 9$, which provides a strong argument in favor of the parabolic assumption.

Figures 4.3a,b confirm that the parabolization assumption has little influence on the optimal spatial perturbations. To the eye, it is difficult to detect a difference in the contours of $\phi(x, z)$ between the parabolized and non-parabolized cases. Both cases differ by less than 0.1%.

The condition at the inlet $\phi_0(z)$ and the perturbation at the exit $\phi(L, z)$ are displayed in Figure 4.4a,b for all three computations. The optimal forcing $\phi_0(z)$ has the same spanwise period as the mean flow $U(z)$ and the maxima of $\phi_0(z)$ coincide with the maxima of the advection velocity $U(z)$. This result matches our physical

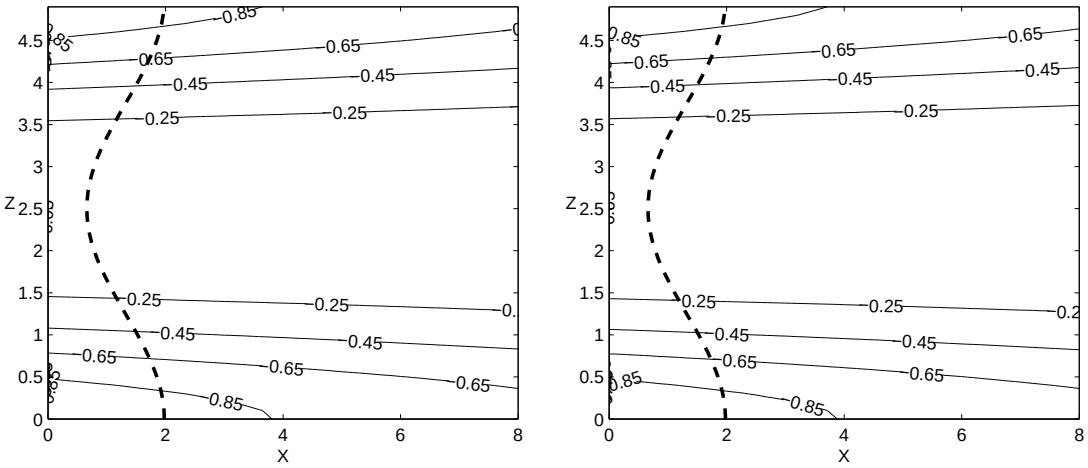

(a) (b)

Figure 4.3: Contour plot of ϕ in the (x, z) plane for (a) the parabolized problem, (b) the non-parabolized case. The velocity profile U is displayed as a thick dashed line, and the parameters are : $U_{max} = 1$, $Re = 100$, $\mu = -0.05$, $L = 9$.

intuition, since in regions of stronger advection disturbances are more rapidly advected downstream and are not subjected to the damping $\mu < 0$ for as long a time as in regions of weaker advection where disturbances experience stronger damping.

4.2.2 Conclusion

A low-dimensional model problem based on the Ginzburg-Landau equation has been derived in order to quantify the error on optimal perturbations induced by parabolization. Gradient-based optimization has been implemented based on the computation of an adjoint problem in a parabolized version of the model and on the numerical evaluation of the gradient in the original non-parabolized case.

Parameters typical of strongly advective flows, $U \sim 1$, $Re \sim 10^2$, $\mu \sim 10^{-1}$ respectively, have been used. Results show that parabolizing the equations by omitting the second streamwise derivative $\frac{1}{Re}\partial_{xx}\phi$ has little influence on the optimal spatial disturbances and their energy amplification. Both the optimal inlet condition ϕ_0 and the energy amplification differ by less than 1% between both cases.

At Reynolds numbers above approximatively 10^2 swept Hiemenz flow is strongly advective in the spanwise direction. Similar to the Ginzburg-Landau model, parabolizing the perturbation equations is expected to induce negligible errors in the shape of the optimal disturbances and their spatial amplification. Once the equations have

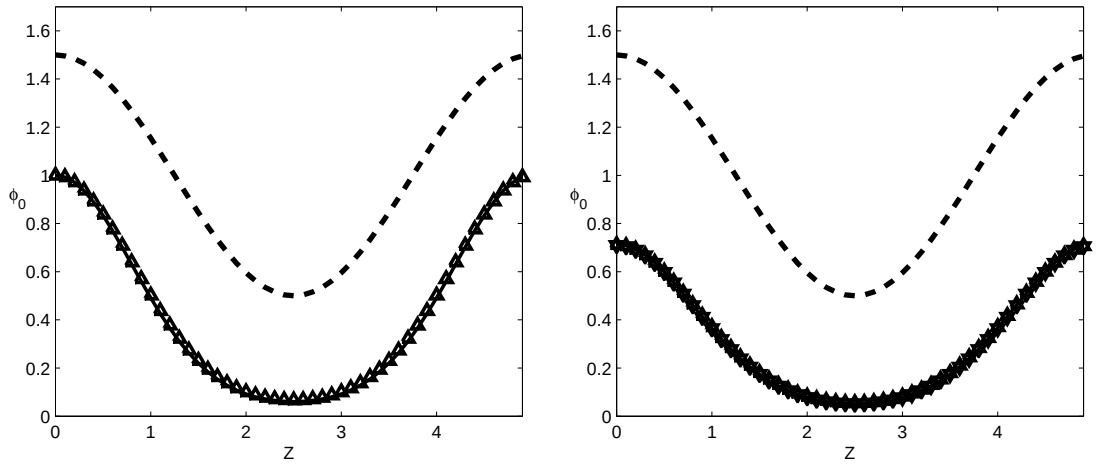

(a) (b)

Figure 4.4: (a) Inlet condition $\phi_0(z)$ and (b) disturbance at the exit $\phi(x = L, z)$ for the parabolized problem (upper triangles), the non-parabolized equations (solid line) and the signalling problem (lower triangles). The velocity profile U is displayed as a thick dashed line, and the parameters are : $U_{max} = 1$, $Re = 100$, $\mu = -0.05$, $L = 9$.

been parabolized, the gradient of the objective functional can be derived analytically and computed by solving an adjoint problem.

4.3 Parabolized spatial equations and numerical techniques

4.3.1 Direct and adjoint parabolized equations in swept Hiemenz flow

In swept Hiemenz flow the spanwise sweep W_∞ as y tends to ∞ may be taken as the reference velocity. After renormalization by W_∞ the chordwise velocity component xU scales like x/Re whereas the spanwise $W-$component is of order unity. As a consequence, at Reynolds numbers higher than about 10^2 and chordwise $x-$distances from the attachment-line of the order of the boundary-layer thickness $\delta = 3$, the sweep velocity W is more than a hundred times higher than the chordwise $xU-$velocity. The flow is thus strongly advective in the spanwise direction, and optimal disturbances are expected to be highly elongated in the streamwise

direction.

Inside the boundary layer of thickness δ and close to the attachment-line the typical length scales are

$$x \sim \delta \,, \tag{4.32a}$$
$$y \sim \delta \,, \tag{4.32b}$$
$$z \sim 1 \,. \tag{4.32c}$$

The continuity equation

$$\partial_x u + \partial_y v + \partial_z w = 0 \tag{4.33}$$

implies that the velocity fields u, v, w scale like

$$u \sim \delta \,, \tag{4.34a}$$
$$v \sim \delta \,, \tag{4.34b}$$
$$w \sim 1 \,. \tag{4.34c}$$

Keeping these scalings in mind and discarding second-order terms of the linearized Navier-Stokes equations in the spanwise $z-$direction, as well as the spanwise pressure gradient, one obtains the parabolized perturbation equations for swept Hiemenz flow,

$$\left(\partial_t + xU\partial_x + V\partial_y + W\partial_z - \frac{1}{Re}(\partial_{xx} + \partial_{yy})\right) u + Uu + xU'v + \partial_x p = 0 \,, \tag{4.35a}$$
$$\left(\partial_t + xU\partial_x + V\partial_y + W\partial_z - \frac{1}{Re}(\partial_{xx} + \partial_{yy})\right) v + V'v + \partial_y p = 0 \,, \tag{4.35b}$$
$$\left(\partial_t + xU\partial_x + V\partial_y + W\partial_z - \frac{1}{Re}(\partial_{xx} + \partial_{yy})\right) w + V'w = 0 \,, \tag{4.35c}$$
$$\partial_x u + \partial_y v + \partial_z w = 0 \,. \tag{4.35d}$$

In the spatial framework disturbances are assumed to be time-harmonic and the temporal derivative ∂_t can be replaced by the imaginary frequency term $-i\omega$ in equations (4.35a,b,c). The spatial development of harmonic disturbances in the spanwise direction is computed from the parabolic set of equations

$$
\begin{aligned}
W\partial_z u &= \left(i\omega - xU\partial_x - V\partial_y + \frac{1}{Re}(\partial_{xx}+\partial_{yy})\right)u - Uu - xU'v - \partial_x p \ , && \text{(4.36a)}\\
W\partial_z v &= \left(i\omega - xU\partial_x - V\partial_y + \frac{1}{Re}(\partial_{xx}+\partial_{yy})\right)v - V'v - \partial_y p \ , && \text{(4.36b)}\\
W\partial_z w &= \left(i\omega - xU\partial_x - V\partial_y + \frac{1}{Re}(\partial_{xx}+\partial_{yy})\right)w - V'w \ , && \text{(4.36c)}\\
0 &= \partial_x u + \partial_y v + \partial_z w \ . && \text{(4.36d)}
\end{aligned}
$$

Optimal energy amplification between the streamwise locations $z = 0$ and $z = z_{max}$ is investigated. The objective functional reads

$$
\mathcal{I} = \frac{E(z_{max})}{E(z=0)} \ , \tag{4.37}
$$

with

$$
E(z) = \frac{1}{2}\int_{y\geq 0} \lambda_E(x)\left(u(z)^2 + v(z)^2 + Re^2 w(z)^2\right)\ dxdydz. \tag{4.38}
$$

The Re^2 factor in front of the w component has been introduced to account for the scaling of u, v, w, respectively. Cossu et al. (2000) qualified as 'physical' a similar definition of the energy of Görtler vortices over a concave wall.

The Gaussian weight function λ_E has been introduced in the temporal framework (see section 3.3.1) in order to remove the unboundedness of the base flow as $x \to \pm\infty$. The reason for introducing an energy weight function, namely, that shear is infinite in the limit of infinite chordwise $x-$coordinates, is also valid in the spatial framework; again, the divergence of the energy integral is efficiently removed by introducing λ_E.

The adjoint problem is derived by applying a procedure similar to the one used in the temporal framework in chapters 2 and 3 or with the parabolized Ginzburg-Landau model (4.15a,b) in section 4.2. The adjoint equations read

$$
\begin{aligned}
W\partial_z\tilde{u} &= \left(-i\omega - xU\partial_x - V\partial_y - U - V' - \frac{1}{Re}(\partial_{xx}+\partial_{yy})\right)\tilde{u} \\
&\qquad + U\tilde{u} - \partial_x\tilde{p}\ , \quad (4.39a)\\
W\partial_z\tilde{v} &= \left(-i\omega - xU\partial_x - V\partial_y - U - V' - \frac{1}{Re}(\partial_{xx}+\partial_{yy})\right)\tilde{v} \\
&\qquad + xU'\tilde{u} + V'\tilde{v} + W'\tilde{w} - \partial_y\tilde{p}\ , \quad (4.39b)\\
W\partial_z\tilde{w} &= \left(-i\omega - xU\partial_x - V\partial_y - U - V' - \frac{1}{Re}(\partial_{xx}+\partial_{yy})\right)\tilde{w} - \partial_z\tilde{p}\ , \quad (4.39c)\\
0 &= \partial_x\tilde{u} + \partial_y\tilde{v}\ . \quad (4.39d)
\end{aligned}
$$

The terminal condition for the adjoint problem reads

$$
\begin{aligned}
W\tilde{u}(z_{max}) &= \frac{2}{E_0}\lambda_E u(z_{max})\ , \quad (4.40a)\\
W\tilde{v}(z_{max}) &= \frac{2}{E_0}\lambda_E v(z_{max})\ , \quad (4.40b)\\
W\tilde{w}(z_{max}) + \tilde{p}(z_{max}) &= \frac{2}{E_0}Re^2\lambda_E w(z_{max})\ , \quad (4.40c)
\end{aligned}
$$

and the gradient of the objective functional is obtained from

$$
\begin{aligned}
\nabla_{u0}\mathcal{I} &= -2\frac{E(z_{max})}{E_0^2}\lambda_E u_0 + W\tilde{u}(z=0)\ , \quad (4.41a)\\
\nabla_{v0}\mathcal{I} &= -2\frac{E(z_{max})}{E_0^2}\lambda_E v_0 + W\tilde{v}(z=0)\ , \quad (4.41b)\\
\nabla_{w0}\mathcal{I} &= -2\frac{E(z_{max})}{E_0^2}Re^2\lambda_E w_0 + W\tilde{w}(z=0) + \tilde{p}(z=0)\ . \quad (4.41c)
\end{aligned}
$$

It is important to note that, in the parabolized framework, the direct and adjoint equations show marked differences. Most significantly, in the adjoint problem mass is conserved in $(x,y)-$planes only and continuity equation (4.39d) is reduced to the intrinsically two-dimensional equation $\partial_x u + \partial_y v = 0$. Also, in contrast to the direct equation (4.36c) the third adjoint momentum equation includes the spanwise derivative of the adjoint pressure $\tilde{p}$.

In the process of deriving the adjoint problem one finds that the adjoint continuity equation lacks the spanwise velocity term since the third direct momentum

equation is void of the $\partial_z p$ term. In a symmetric fashion, the three-term direct continuity equation causes a $\partial_z \tilde{p}$ pressure term to appear in the adjoint equations.

The λ_E energy weight has been introduced in order to confine disturbances close to the attachment-line. Although disturbances should be equal to zero at $\pm x_{max}$, the same fringe region damping $\lambda(x)$ as in chapter 3 has been introduced in order to avoid error accumulation at outermost chordwise locations.

4.3.2 Numerical techniques

For both the direct and adjoint problems the numerical domain $(-x_{max}, x_{max}) \times (0, y_{max}) \times (0, z_{max})$ is discretized using an equispaced grid in the x, z directions, with cells of size $\delta x, \delta z$. Chebyshev polynomials are used in the wall-normal $y-$direction.

Direct equations (4.36a,b,c,d) and adjoint equations (4.39a,b,c,d) are similar to the boundary-layer equations used by Andersson et al. (1999), Luchini (2000) and Tumin and Reshotko (2001) to compute optimal spatial disturbances in a Blasius boundary layer. From a numerical point of view, the present study is most closely related to Andersson et al. (1999) where the optimization is performed using an adjoint-based algorithm. In addition to parabolization Andersson et al. (1999) made the assumption that perturbations were periodic in the transverse direction, which in the present study would amount to considering periodic perturbations in x. By doing so, Andersson et al. (1999) ended up with a system of four one-dimensional equations in the wall-normal $y-$direction that could be marched in the streamwise direction, in our case z, using a fully implicit scheme.

In swept Hiemenz flow the chordwise basic velocity field depends on the chordwise $x-$coordinate. Chordwise Fourier modes are coupled in equations (4.36a,b,c) and one cannot divide the problem into a set of n_x one-dimensional equations in y. Instead, marching equations (4.36a,b,c,d) involves solving a two-dimensional elliptic problem in x and y at each step. The fully implicit scheme developed by Andersson et al. (1999) that was well suited for one-dimensional parabolic equations has thus to be modified to accommodate the chordwise coupling.

In the direct problem, the momentum equations (4.36a,b,c) may be advanced using a mixed Adams-Bashforth/Crank-Nicolson scheme. The velocity fields u_i^{n+1} at the spanwise discretization point $(n+1)$ are computed according to

$$\left(W - \frac{\delta z}{2Re}\nabla^2_{x,y}\right) u_i^{n+1} = \left(W + \frac{\delta z}{2Re}\nabla^2_{x,y}\right) u_i^n + \delta z \left(\frac{3}{2} f_{u_i^n} - \frac{1}{2} f_{u_i^{n-1}}\right) \ , \qquad (4.42)$$

with

$$
\begin{aligned}
f_u^n &= (i\omega - xU\partial_x - V\partial_y)u^n - Uu^n - xU'v^n - \partial_x p^n \ , && \text{(4.43a)}\\
f_v^n &= (i\omega - xU\partial_x - V\partial_y)v^n - V'v^n - \partial_y p^n \ , && \text{(4.43b)}\\
f_w^n &= (i\omega - xU\partial_x - V\partial_y)w^n - W'w^n \ . && \text{(4.43c)}\\
& && \text{(4.43d)}
\end{aligned}
$$

Marching the momentum equations according to (4.42) does not ensure mass conservation at step $n+1$, which can be achieved by solving simultaneously the continuity equation

$$\partial_x u^{n+1} + \partial_y v^{n+1} + \partial_z w^{n+1} = 0 \ . \tag{4.44}$$

The four variables u, v, w, p can be computed simultaneously at step $n+1$ by treating pressure implicitly according to

$$
\begin{aligned}
\left(W - \frac{\delta z}{2Re}\nabla^2_{x,y}\right) u^{n+1} + \partial_x p^{n+1} &= \left(W + \frac{\delta z}{2Re}\nabla^2_{x,y}\right) u^n + \delta z \left(\frac{3}{2}g_{u^n} - \frac{1}{2}g_{u^{n-1}}\right), && \text{(4.45a)}\\
\left(W - \frac{\delta z}{2Re}\nabla^2_{x,y}\right) v^{n+1} + \partial_y p^{n+1} &= \left(W + \frac{\delta z}{2Re}\nabla^2_{x,y}\right) v^n + \delta z \left(\frac{3}{2}g_{v^n} - \frac{1}{2}g_{v^{n-1}}\right), && \text{(4.45b)}\\
\left(W - \frac{\delta z}{2Re}\nabla^2_{x,y}\right) w^{n+1} &= \left(W + \frac{\delta z}{2Re}\nabla^2_{x,y}\right) w^n + \delta z \left(\frac{3}{2}g_{w^n} - \frac{1}{2}g_{w^{n-1}}\right), && \text{(4.45c)}\\
\partial_x u^{n+1} + \partial_y v^{n+1} + \partial_z w^{n+1} &= 0, && \text{(4.45d)}
\end{aligned}
$$

with

$$
\begin{aligned}
g_u^n &= (i\omega - xU\partial_x - V\partial_y)u^n - Uu^n - xU'v^n \ , && \text{(4.46a)}\\
g_v^n &= (i\omega - xU\partial_x - V\partial_y)v^n - V'v^n \ , && \text{(4.46b)}\\
g_w^n &= (i\omega - xU\partial_x - V\partial_y)w^n - W'w^n \ . && \text{(4.46c)}\\
& && \text{(4.46d)}
\end{aligned}
$$

No chordwise coupling terms appear on the left-hand side of system (4.45a,b,c,d). The solution of the set of equations can be found by solving the set of one-dimensional equations (4.47) at each k_x Fourier mode separately:

$$\left(W - \frac{\delta z}{2Re}(\partial_y y - k_x^2)\right)\hat{u}^{n+1} + ik_x\delta z p^{n+1} = \hat{\mathcal{G}}_u^{n,n-1} , \quad (4.47a)$$

$$\left(W - \frac{\delta z}{2Re}(\partial_y y - k_x^2)\right)\hat{v}^{n+1} + \delta z\partial_y p^{n+1} = \hat{\mathcal{G}}_v^{n,n-1} , \quad (4.47b)$$

$$\left(W - \frac{\delta z}{2Re}(\partial_y y - k_x^2)\right)\hat{w}^{n+1} = \hat{\mathcal{G}}_w^{n,n-1} , \quad (4.47c)$$

$$ik_x\hat{u}^{n+1} + \partial_y\hat{v}^{n+1} + \partial_z\hat{w}^{n+1} = 0 , \quad (4.47d)$$

with

$$\mathcal{G}_{u_i}^{n,n-1} = \left(W + \frac{\delta z}{2Re}\nabla_{x,y}^2\right)u_i^n + \delta z\left(\frac{3}{2}g_{u_i^n} - \frac{1}{2}g_{u_i^{n-1}}\right) . \quad (4.48)$$

Equations (4.47) are solved as in Andersson et al. (1999) by discretizing the n_x one-dimensional left-hand-side operators in equations (4.47a,b,c,d) into n_x matrices of size $(4n_y)^2$ and then inverting these matrices. It should be mentioned that, for the first spatial step, the equations are solved using a first-order scheme by setting $g_{u_i}^{n-1} = g_{u_i}^n$.

The mixed implicit-explicit scheme described above has good stability properties and will be compared with previously published optimal disturbance results by Andersson et al. (1999), Luchini (2000) and Tumin and Reshotko (2001) in section 4.4.

The adjoint equation is similar to the direct equation and is solved using the same marching scheme in the reverse spanwise direction. The adjoint pressure term $\partial_z\tilde{p}$ is discretized using first-order upwind finite differences, and each adjoint Fourier mode $\check{u}, \check{v}, \check{w}, \check{p}$ is solved according to

$$\left(W - \frac{\delta z}{2Re}(\partial_y y - k_x^2)\right)\check{u}^{n-1} + ik_x\delta z p^{n-1} = \check{\mathcal{G}}_u^{n,n+1} , \quad (4.49a)$$

$$\left(W - \frac{\delta z}{2Re}(\partial_y y - k_x^2)\right)\check{v}^{n-1} + \delta z\partial_y p^{n-1} = \check{\mathcal{G}}_v^{n,n+1} , \quad (4.49b)$$

$$\left(W - \frac{\delta z}{2Re}(\partial_y y - k_x^2)\right)\check{w}^{n-1} + \check{p}^{n-1} = \check{p}^n + \check{\mathcal{G}}_w^{n,n+1} , \quad (4.49c)$$

$$ik_x\check{u}^{n-1} + \partial_y\check{v}^{n-1} + \partial_z\check{w}^{n-1} = 0 . \quad (4.49d)$$

It remains to compute the adjoint terminal condition. The adjoint variables $\tilde{u}, \tilde{v}, \tilde{w}, \tilde{p}$ at z_{max} should satisfy

$$W\tilde{u}(z_{max}) = \frac{2}{E_0}\lambda_E u(z_{max}) \ , \tag{4.50a}$$

$$W\tilde{v}(z_{max}) = \frac{2}{E_0}\lambda_E v(z_{max}) \ , \tag{4.50b}$$

$$W\tilde{w}(z_{max}) + \tilde{p}(z_{max}) = \frac{2}{E_0}Re^2\lambda_E w(z_{max}) \ . \tag{4.50c}$$

In the fully-implicit scheme used by Andersson et al. (1999) the terminal condition (4.50a,b,c) is exactly the right-hand side of equations (4.49). In the mixed implicit-explicit scheme used in the present study the right-hand-side of equations (4.49) remains undetermined because the condition (4.50a,b,c) is given in the form of an underdetermined linear system.

The first step of the adjoint computation may be treated implicitely if the coupling terms involving the chordwise stretching are assumed to be negligible. In this case adjoint equations (4.39) are marched from the discretization point n at $z = z_{max}$ to point $n-1$ at $z = z_{max} - \delta z$ by solving the linear system

$$\left(\frac{W}{\delta z} - i\omega - V\partial_y - U - V' - \frac{1}{Re}(\partial_{xx} + \partial_{yy})\right)\tilde{u}^{n-1} + U\tilde{u}^{n-1} - \partial_x\tilde{p}^{n-1} = \frac{\lambda_E}{\delta z}u^n \ , \tag{4.51a}$$

$$\left(\frac{W}{\delta z} - i\omega - V\partial_y - U - V' - \frac{1}{Re}(\partial_{xx} + \partial_{yy})\right)\tilde{v}^{n-1} + V'\tilde{v}^{n-1} + W'\tilde{w}^{n-1} - \partial_y\tilde{p}^{n-1} = \frac{\lambda_E}{\delta z}v^n \ , \tag{4.51b}$$

$$\left(\frac{W}{\delta z} - i\omega - V\partial_y - U - V' - \frac{1}{Re}(\partial_{xx} + \partial_{yy})\right)\tilde{w}^{n-1} - \partial_z\tilde{p}^{n-1} = Re^2\frac{\lambda_E}{\delta z}w^n \ , \tag{4.51c}$$

$$\partial_x\tilde{u}^{n-1} + \partial_y\tilde{v}^{n-1} = 0 \ . \tag{4.51d}$$

This assumption is necessary at the first step only and does not seem to alter the optimal disturbances significantly, since the results of Andersson et al. (1999), Luchini (2000) and Tumin and Reshotko (2001) have been accurately reproduced.

4.4 Validation of the numerical scheme

Optimal spatial disturbances in a parallel Blasius boundary layer have been computed by Tumin and Reshotko (2001). The numerical scheme described in sec-

tion 4.3.2 may be validated by replacing the swept Hiemenz flow base profile by the simpler two-dimensional Blasius velocity profile and then reproduce the results of Tumin and Reshotko (2001). Some qualitative results can also be compared to Andersson et al. (1999) and Luchini (2000) although they used a developing Blasius boundary layer as a base flow. In the latter case, their objective functional differs from ours but qualitative results are mostly unaffected.

In all three investigations (Andersson et al. (1999), Luchini (2000) and Tumin and Reshotko (2001)) the optimization distance between x_0 and x_{max} is the streamwise reference length. In terms of scaled coordinates, the inlet is located at $x = 0$ and the exit is at $x_{max} = 1$. The boundary-layer equations used by Tumin and Reshotko (2001) are exactly recovered by setting $U = 0$, $V = 0$, $W = U_{BL}$ and $Re = 1$ in equations (4.36), with U_{BL} denoting the Blasius velocity profile. To avoid confusing the coordinate systems, the spanwise wavenumber β of Andersson et al. (1999) will be called the transverse wavenumber.

The energy amplification is displayed as a function of the transverse wavenumber β in Figure 4.5a. Several optimizations have been performed with x_{max} varying from $x_{max} = 0.2$ to $x_{max} = 1$. For $x_{max} = 1$, the maximum energy amplification is obtained for $\beta = 0.43$ which is within 5% of Andersson et al. (1999), Luchini (2000) and Tumin and Reshotko (2001). The maximum energy amplification increases with x_{max} whereas the optimal wavenumber decreases monotonically as x_{max} increases (see Figure 4.5b). The maximum energy amplification at $x_{max} = 1$, $\beta = 0.45$ is equal to $4.5 \cdot 10^{-3}$ which closely matches the results of Tumin and Reshotko (2001).

As in Andersson et al. (1999), Luchini (2000) and Tumin and Reshotko (2001), the optimal disturbances take the shape of streamwise vortices, displayed in Figure 4.6a. Streamwise streaks, displayed in Figure 4.6b, are generated downstream of the forcing location. Consistently with Luchini (2000) the maximum of the wall-normal velocity profile increases with the transverse wavenumber β and approaches the wall as β increases. In contrast, the maximum of the transverse velocity profile decreases as β increases. Also, the resulting downstream streak is mostly unaffected by changes in the transverse wavenumber β.

The optimal perturbation results of Andersson et al. (1999), Luchini (2000) and Tumin and Reshotko (2001) for a Blasius boundary layer have been recovered with very good agreement. The Blasius velocity profile may now be replaced by the swept Hiemenz base flow to determine the optimal spatial disturbances in the vicinity of the attachment-line.

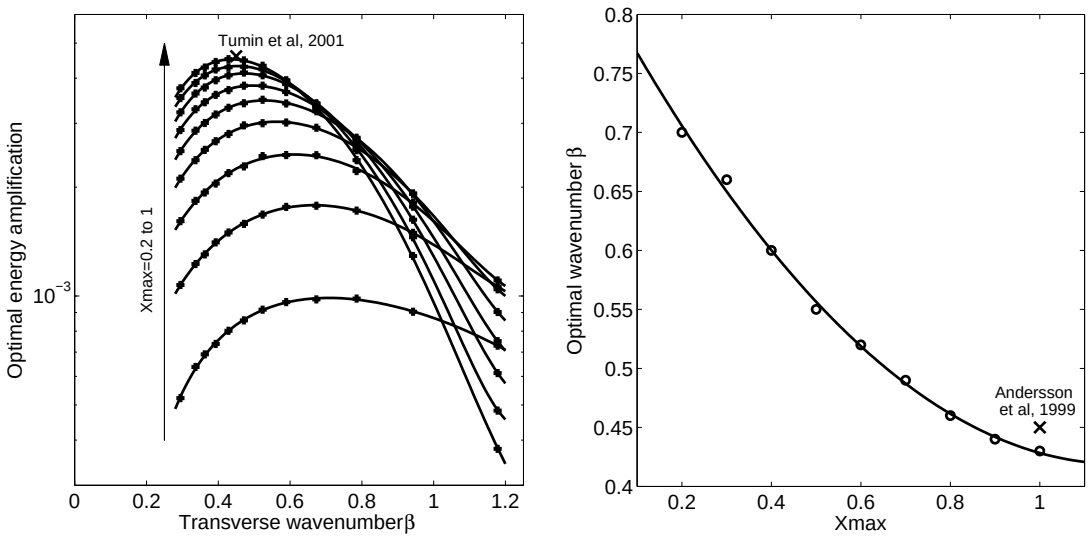

(a) (b)

Figure 4.5: (a) Energy amplification versus the transverse wavenumber for the Blasius velocity profile as a base flow. The maximum energy amplification observed at $\beta = 0.45$ by Tumin *et al.* (2001) is marked with a cross symbol. (b) The optimal wavenumber versus x_{max} (circles). The optimal wavenumber $\beta = 0.45$ found by Andersson *et al.* (1999), Luchini (2000) and Tumin *et al.* (2001) at $x_{max} = 1$ is marked with a cross symbol.

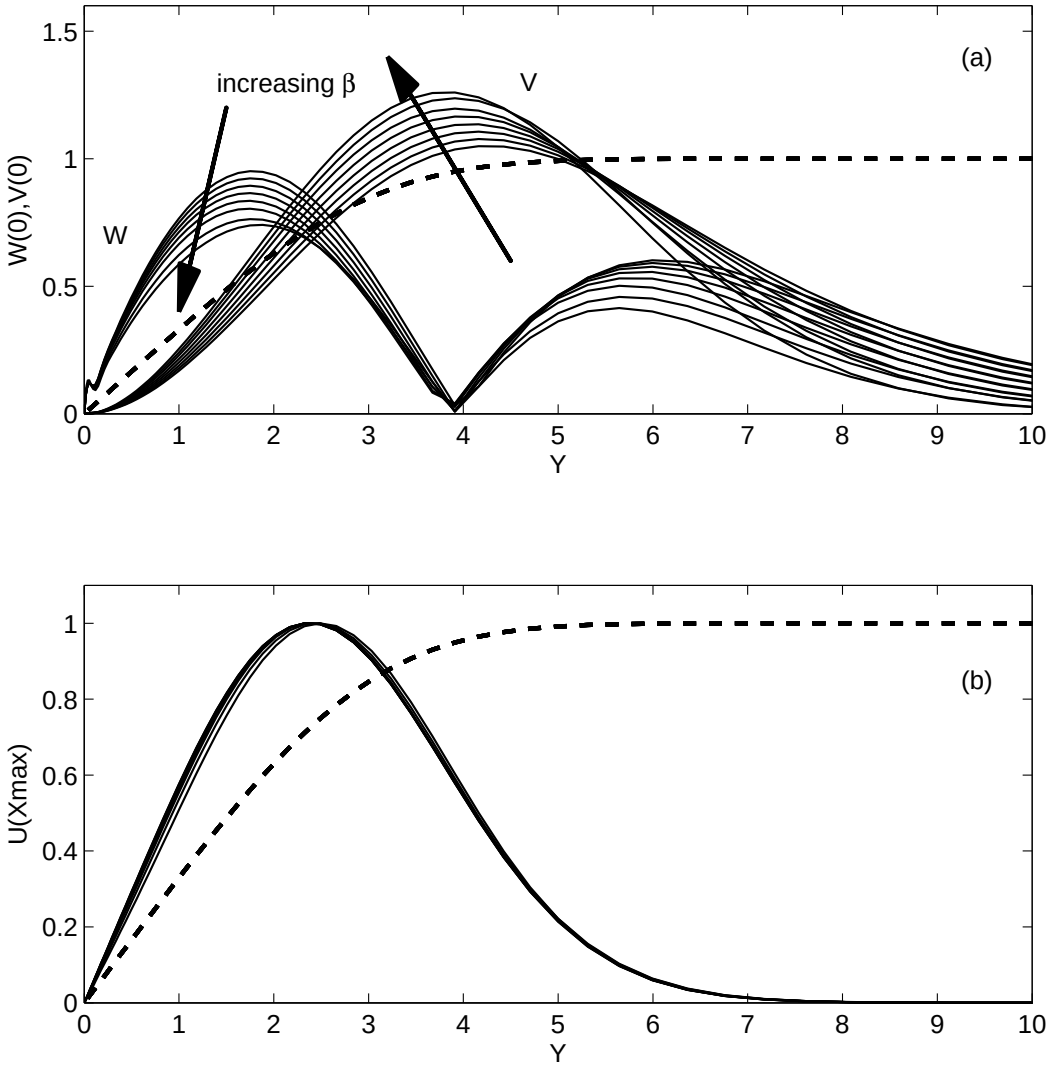

Figure 4.6: (a) $v-, w-$velocity profiles of the optimal inlet perturbation at entrance and (b) the resulting downstream streak for $z_{max} = 1$. The streamwise $u-$velocity component is equal to zero at the inlet $x = 0$ and dominates at the exit $x = x_{max}$. Several profiles are shown for the transverse wavenumber β varying from 0.3 to 0.8 (arrows). The basic Blasius velocity profile is displayed as a dashed line.

4.5 Optimal spatial perturbations in swept Hiemenz flow

4.5.1 Flow parameters in the spatial framework

Swept Hiemenz flow is characterized by a single non-dimensional parameter, the Reynolds number

$$Re = \frac{W_\infty \delta}{\nu} \ . \tag{4.52}$$

For a given flow stretching rate $\partial U/\partial x$ in the chordwise direction, the Reynolds number is proportional to the spanwise sweep W_∞ at infinite y.

Stationary disturbances are characterized by their frequency ω. In the developing Blasius boundary layer, for instance, Luchini (2000) showed that the most amplified disturbances are steady perturbations at $\omega = 0$.

In swept Hiemenz flow chordwise Fourier modes are coupled by the chordwise component xU of the basic velocity field. In contrast with two-dimensional boundary layers, perturbations that are initially periodic along the chordwise $x-$direction do not remain periodic downstream of the inlet. As a consequence, perturbations in swept Hiemenz flow may not be classified based on their chordwise wavenumber as in two-dimensional boundary layers. Depending on the width parameter L of the chordwise energy weight function

$$\lambda_E(x) = e^{-(x/L)^2} \ , \tag{4.53}$$

perturbations are expected to extend over a finite distance in the chordwise direction. In this sense, the width of the energy weight provides the chordwise parameter missing from the two-dimensional case.

Optimal disturbances also depend on the spanwise distance z_{max} over which energy amplification is optimized. In Andersson et al. (1999) and Luchini (2000) the optimization length z_{max} is taken to be the streamwise reference length. There is no streamwise reference length in swept Hiemenz flow and z_{max} is included as an independent parameter in the present study.

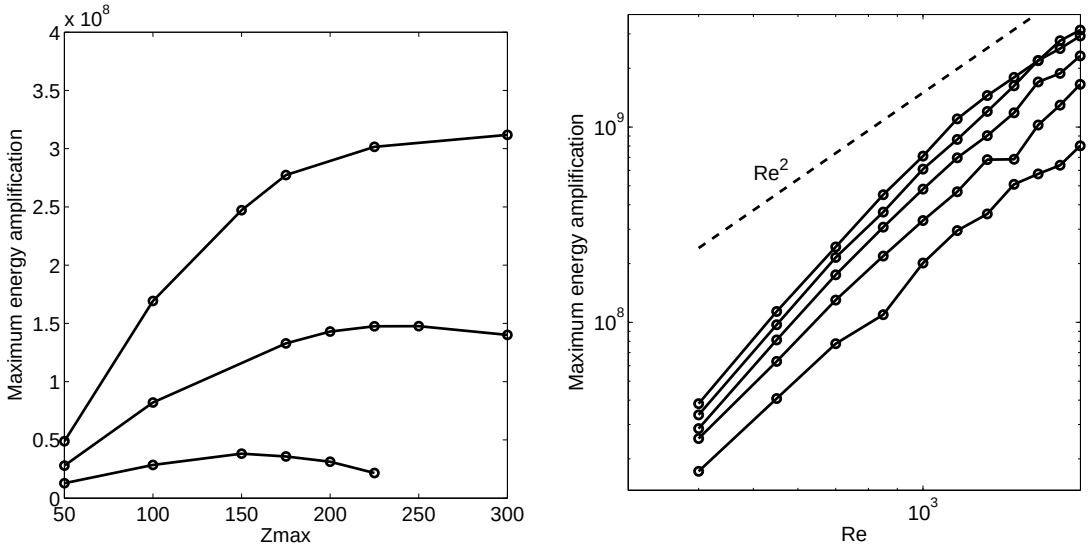

(a) (b)

Figure 4.7: (a) Optimal energy amplification versus spanwise optimization distance z_{max} for Reynolds numbers $Re = 400$ (lower curve), $Re = 550$ and $Re = 700$ (top curve). The other parameters have been set equal to $L = 3$, $\omega = 0$. (b) Optimal energy amplification versus Reynolds number Re for $z_{max} = 60$ (lower curve), $z_{max} = 80$, $z_{max} = 120$ and $z_{max} = 140$ (higher curve), at $L = 3$, $\omega = 0$.

4.5.2 Optimal spatial energy amplification

Let us set the chordwise parameter to$L = 3$; the energy weight function is then twice as wide as the boundary layer thickness. At Reynolds number $Re = 550$ and zero frequency $\omega = 0$ the perturbation energy is amplified up to $E_{max} = 1.48 \cdot 10^8$ at $z_{max} = 240$ as shown in Figure 4.7a. Beyond this critical distance dissipation begins to overcome energy production.

In the boundary-layer approximation the three non-dimensional velocity components u, v, w are of the same order of magnitude, so that when the Reynolds number Re is large, wherever the spanwise velocity component w is not equal to zero the energy

$$E(z) = \frac{1}{2} \int_{y \geq 0} \lambda_E(x) \left(u(z)^2 + v(z)^2 + Re^2 w(z)^2 \right) \, dxdydz \tag{4.54}$$

is equal at leading order to

$$E(z) = Re^2 \frac{1}{2} \int_{y\geq 0} \lambda_E(x) w(z)^2 \; dxdydz \; . \tag{4.55}$$

In particular, w is expected to be different from zero at the downstream end z_{max} of the optimization domain, so that the objective functional is equal at first order to

$$\mathcal{I} = Re^2 \frac{\int_{y\geq 0} \lambda_E(x) w(z_{max})^2 \; dxdydz}{\int_{y\geq 0} \lambda_E(x) \left(u(z=0)^2 + v(z=0)^2 + Re^2 w(z=0)^2\right) \; dxdydz} \; . \tag{4.56}$$

Due to the Re^2 factor in the denominator of the objective functional $\mathcal{I}$, of all possible disturbances, the ones that have zero initial spanwise velocity $w(z=0)$ will be the most amplified at large Reynolds numbers. The objective functional is therefore equal at leading order to

$$\mathcal{I} = Re^2 \frac{\int_{y\geq 0} \lambda_E(x) w(z_{max})^2 \; dxdydz}{\int_{y\geq 0} \lambda_E(x) \left(u(z=0)^2 + v(z=0)^2\right) \; dxdydz} \; . \tag{4.57}$$

According to equation (4.57) the optimal energy amplification at a given spanwise location z_{max} is expected to scale as Re^2 at large Reynolds numbers. With a similar reasoning Luchini (2000) found that the optimal energy amplification in the developing Blasius boundary layer scales linearly with Reynolds number. Energy amplification is displayed as a function of the Reynolds number Re in Figure 4.7b at several spanwise locations z_{max}. The Re^2-scaling appears to be recovered for higher Reynolds numbers.

The optimal energy amplification is plotted against the forcing frequency ω in Figure 4.8a for $L = 3$, $z_{max} = 100$ and $Re = 550$. As in Luchini (2000), steady disturbances are found to be more amplified than perturbations of non-zero ω frequency.

At Reynolds number $Re = 550$ and spanwise optimization distances z_{max} varying from $z_{max} = 75$ to 150 the optimal energy amplification, displayed in Figure 4.8b, increases slightly with the chordwise extent L of the energy weight function λ_E. This is in contrast with the results of Andersson et al. (1999) and Luchini (2000), who found an optimal wavenumber $\beta = 0.45$. A physical interpretation that actually matches spatial optimization results in the Blasius boundary layer, based on the shape of optimal spatial disturbances, is suggested in section 4.5.3.

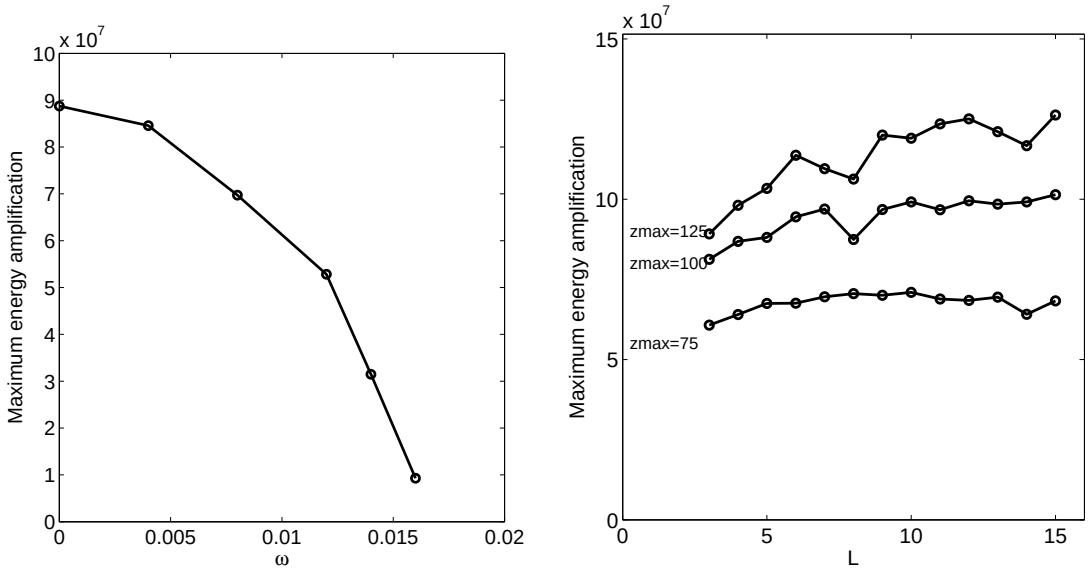

(a) (b)

Figure 4.8: Energy amplification levels versus (a) forcing frequency ω for $L = 3$, $z_{max} = 100$ (b) width L of the chordwise energy weight function at forcing frequency $\omega = 0$ for $z_{max} = 75$, $z_{max} = 100$ and $z_{max} = 125$. The Reynolds number has been set equal to $Re = 550$.

4.5.3 Optimal spatial disturbances

Optimal spatial disturbances take the shape of spanwise counter-rotating vortices as shown in Figure 4.9a. Spanwise streaks, displayed in Figure 4.9b, are generated downstream by the so-called lift-up mechanism.

Isosurfaces of the velocity components, displayed in Figure 4.10, give a striking picture of the production of spanwise $w-$velocity from chordwise $u-$ and wall-normal $v-$initial velocity. The isosurfaces of u and v that represent the inlet optimal spanwise vortices at $y = 2.5$ both end before the outlet z_{max}, showing that both velocity components are damped to less than 20% of their initial value between the inlet $z = 0$ and the outlet $z = z_{max}$. By contrast, the isosurface at 20% of the spanwise $w-$velocity component expand from z slightly superior to $z = 0$ to $z = z_{max}$.

When the chordwise length parameter is set equal to the boundary-layer thickness $L = 3$, three streamwise vortices are formed only (see Figure 4.9a and Figure 4.11, $L = 3$ plot). When L is increased, more streamwise rolls of approximately constant width are observed, as shown in Figure 4.11 for L varying from $L = 3$ to $L = 12$.

The number of streamwise vortices may be estimated by counting the local maxima of the wall-normal $v-$velocity along the chordwise $x-$axis. The maxima that are located further away from the attachment-line are not well-defined since they take very low values, and the number of vortices actually measured is subject to significant error. However, the estimated number of vortices displayed in Figure 4.12a exhibits a clear tendency to increase with L. The chordwise width of optimal streamwise vortices, displayed in Figure 4.12b, increases slightly with L.

4.5.4 Discussion

It has been shown that optimal spatial disturbances in swept Hiemenz flow take the shape of spanwise counter-rotating vortices. Perturbation energy is amplified due to the interaction of spanwise vortices with the basic spanwise shear W', which generates spanwise perturbation velocity w via the lift-up mechanism.

By analogy with the Blasius boundary layer where there exists an optimal transverse wavenumber β, lift-up associated to the spanwise shear W' is expected to exhibit an optimal chordwise wavenumber γ. Since disturbances are not ascribed any particular chordwise wavelength in the present study, optimal perturbations in swept Hiemenz flow are expected to arise at the optimal chordwise wavenumber γ.

Our interpretation of the results of this section is that the Gaussian energy weight

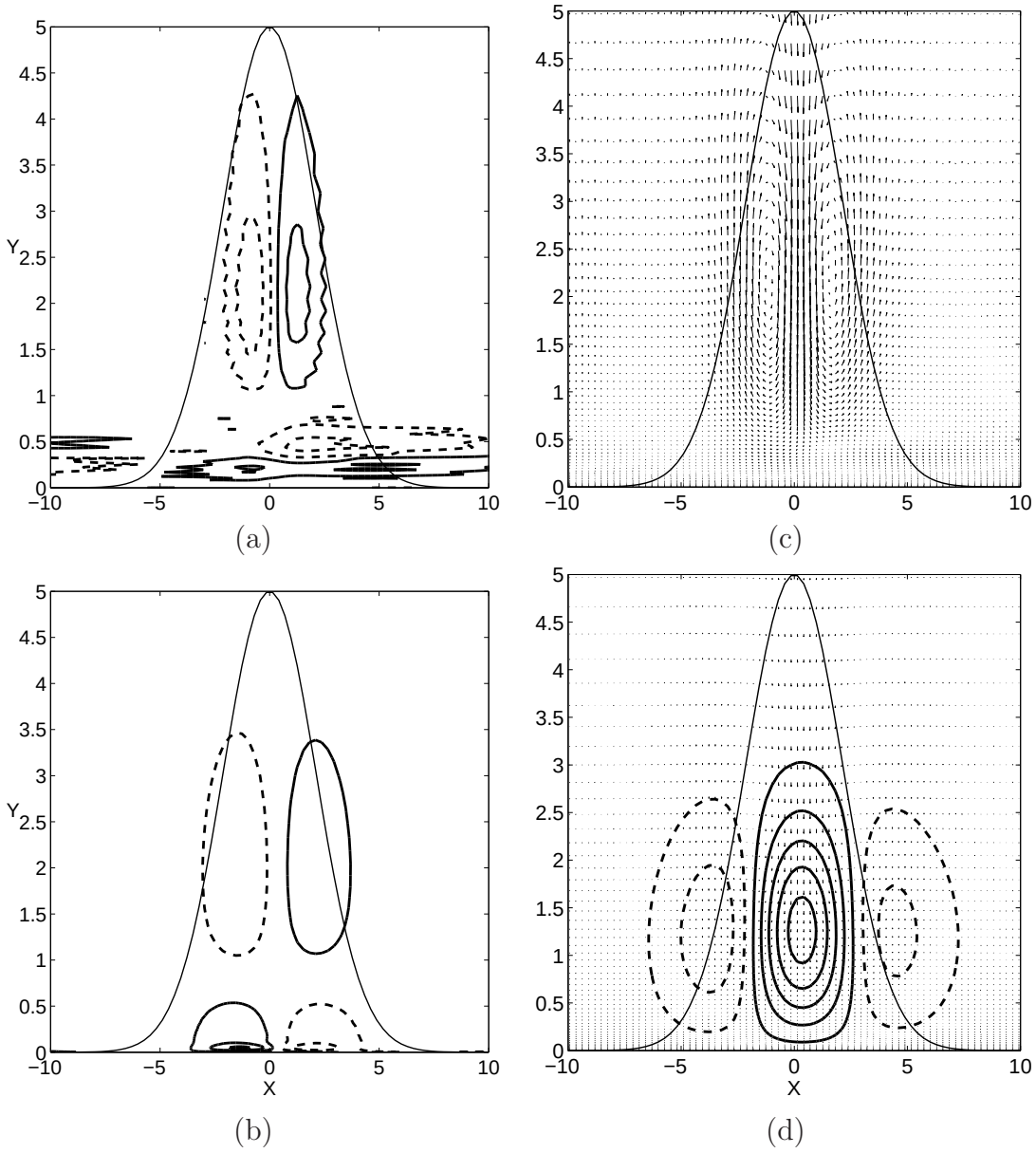

Figure 4.9: Isocontours of spanwise vorticity in an (x, y) plane at (a) $z = 0$, (b) $z = z_{max}$ for an optimal disturbance at $z_{max} = 200$, $Re = 550$, $L = 3$, $\omega = 0$. Velocity field (arrows) and isocontours of spanwise velocity (contours) in an (x, y) plane at (c) $z = 0$, (d) $z = z_{max}$ for the same optimal disturbance at $z_{max} = 200$, $Re = 550$, $L = 3$, $\omega = 0$. Spanwise velocity is equal to zero at $z = 0$. The energy weight function λ_E is sketched as a thin solid line.

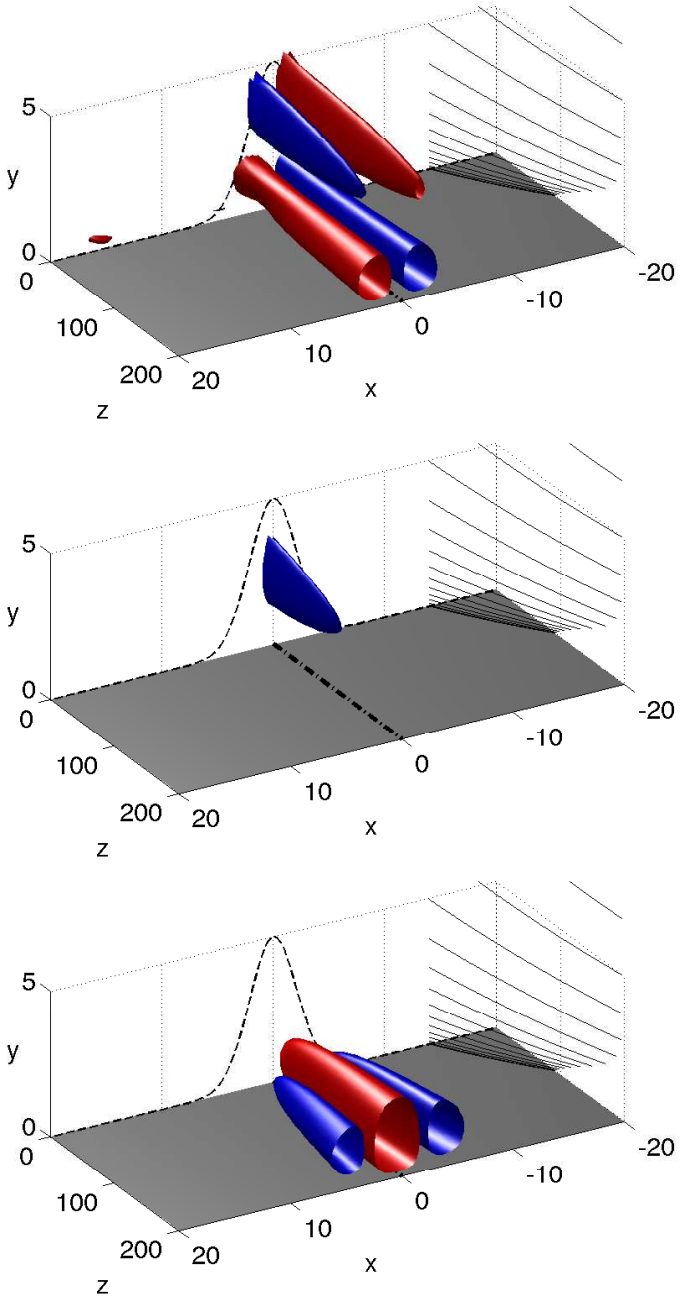

Figure 4.10: Isosurface at 20% of the maximum for (a) the chordwise $u-$velocity, (b) the wall-normal $v-$velocity, (c) the spanwise $w-$velocity components of an optimal disturbance developing from $z = 0$ to $z_{max} = 200$. Blue and red denote negative and positive values, respectively. The remaining parameters are set equal to $Re = 550$, $L = 3$, $\omega = 0$. Energy weight function λ_E is sketched as a thin dashed line and streamlines of the basic flow are displayed as thin lines on the right-hand side of each picture.

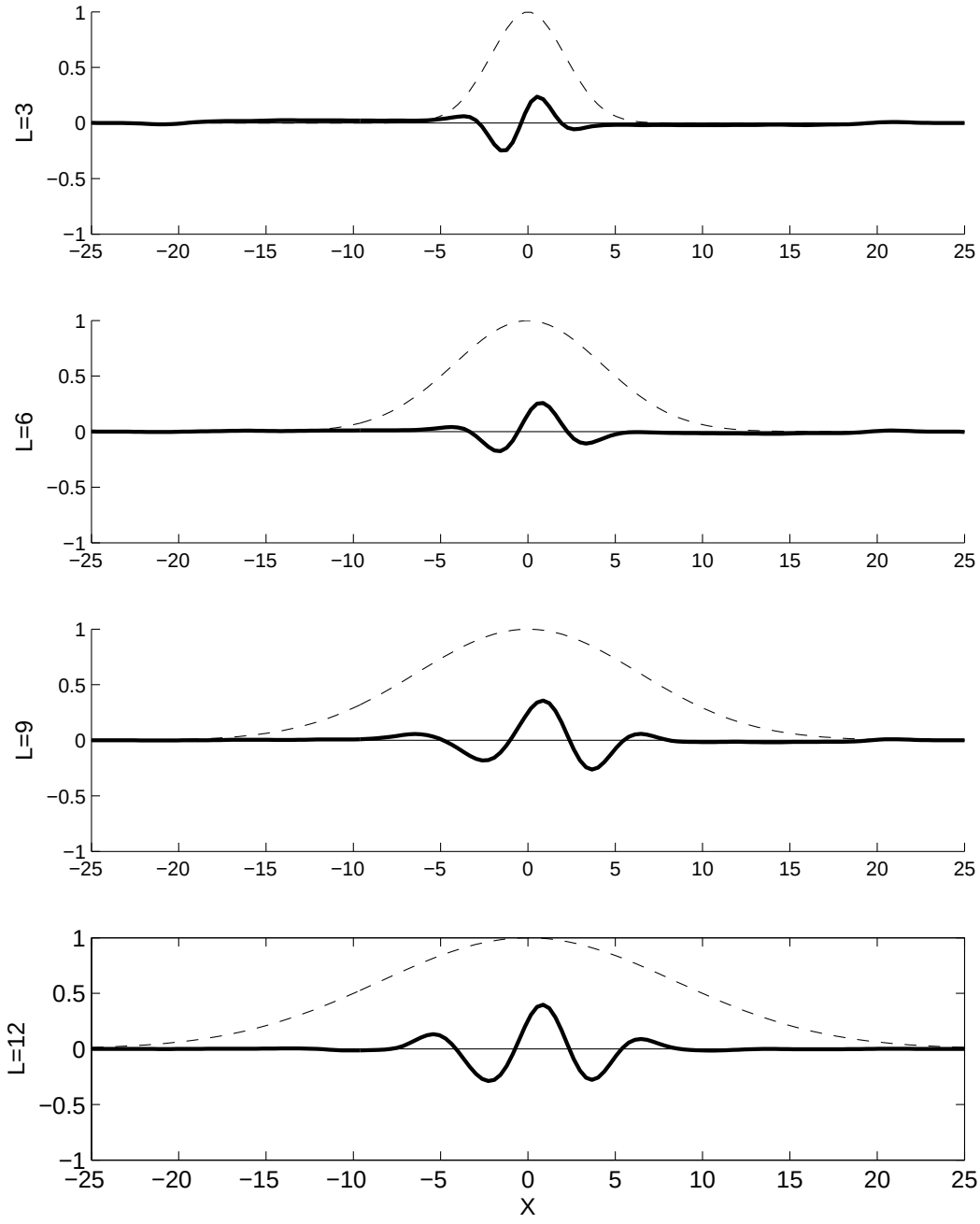

Figure 4.11: Profiles in the chordwise $x-$direction of the wall-normal $v-$velocity for an optimal disturbance taken at $z = 0$, for $L = 3$, $L = 6$, $L = 9$ and $L = 12$ (top to bottom). Flow parameters are set equal to $z_{max} = 125$, $Re = 550$, $\omega = 0$. Energy weight function λ_E is sketched as a thin dashed line.

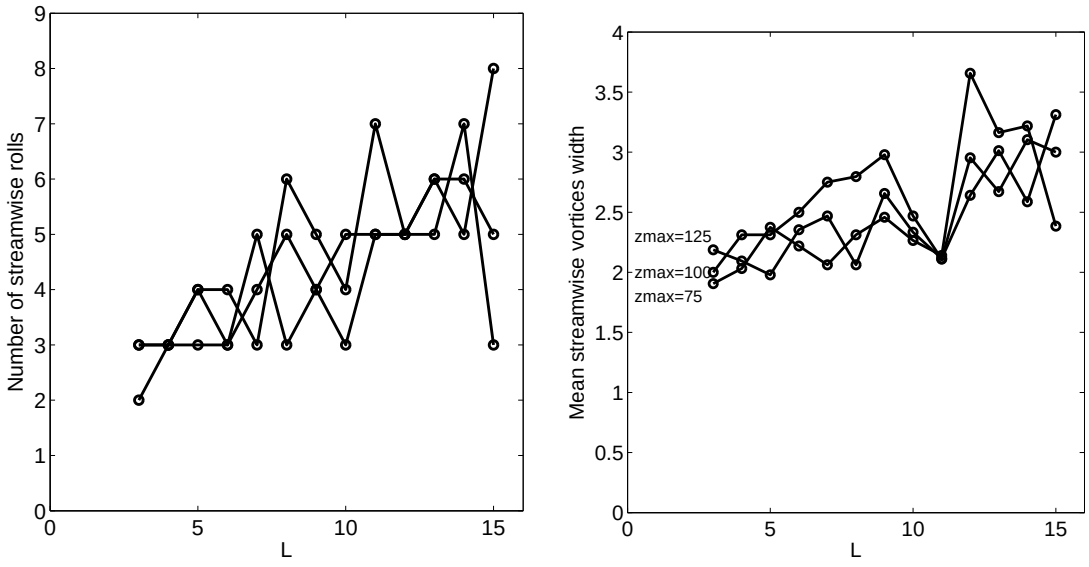

(a) (b)

Figure 4.12: (a) Number of initial spanwise vortices and (b) mean vortex width in the chordwise $x-$direction versus L for optimal disturbances with z_{max} varying for $z_{max} = 75$ (in both plots, bottom curve), $z_{max} = 100$ and $z_{max} = 125$ (top curve). The remaining parameters are $Re = 550$, $\omega = 0$.

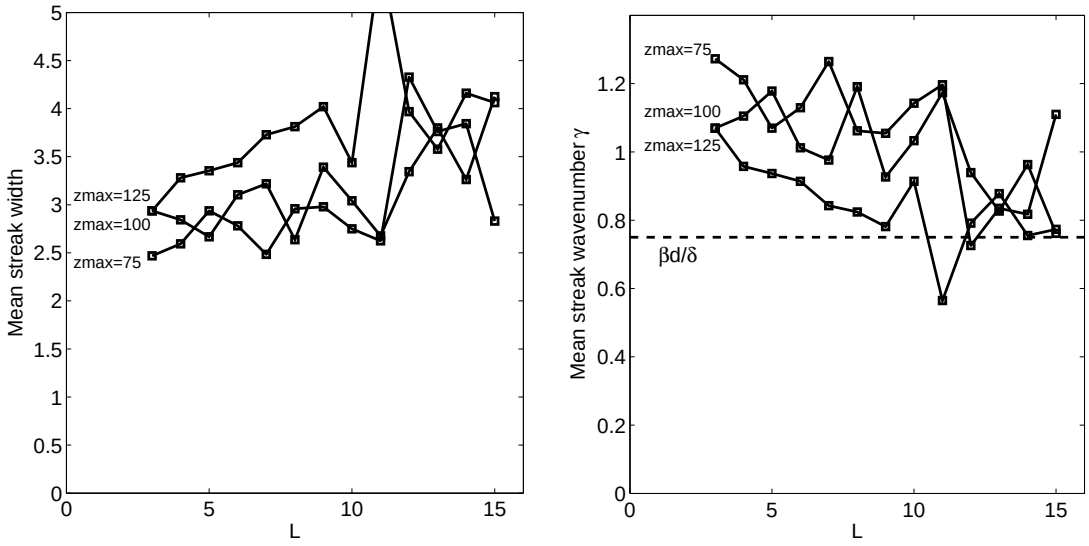

(a) (b)

Figure 4.13: (a) Mean width Λ of optimal streaks at z_{max} and (b) the associated wavenumber $2\pi/\Lambda$ as functions of the chordwise length L for $z_{max} = 75$, $z_{max} = 100$ and $z_{max} = 125$. The remaining parameters are set equal to $Re = 550$ and $\omega = 0$.

function $\lambda_E(x)$ acts as a filter by selecting only part of an 'ideal' optimal disturbance that takes the shape of an infinite array of counter-rotating spanwise vortices with a chordwise wavenumber γ. As the chordwise parameter L increases the Gaussian weight broadens and more spanwise vortices are selected (see Figure 4.12a); since each of these rolls induces the same amount of amplification, the energy amplification is mostly unchanged as L increases (see Figure 4.8b).

The basic spanwise velocity component W in swept Hiemenz flow resembles the Blasius velocity profile, except that the non-dimensional boundary-layer thickness is $\delta = 3$ instead of $\mathrm{d} = 5$ for the Blasius profile. The spanwise sweep W in swept Hiemenz flow is almost exactly recovered by stretching the Blasius velocity profile by $\delta/\mathrm{d} = 3/5$ along the wall-normal direction.

According to Andersson et al. (1999) and Luchini (2000), optimal streaks in the developing Blasius boundary layer experience the largest energy amplification at the optimal transverse wavenumber $\beta = 0.45$. Since the spanwise sweep W, which is responsible for spanwise lift-up phenomena in swept Hiemenz flow, is closely approximated by scaling the Blasius velocity profile by $\delta/\mathrm{d} = 3/5$, the optimal wavenumber γ of spatial disturbances in swept Hiemenz flow may be compared to β scaled by $\mathrm{d}/\delta = 5/3$.

Due to the chordwise stretching and to viscous diffusion, optimal disturbances in swept Hiemenz flow spread in the chordwise direction from the inlet $z = 0$ to the outlet $z = z_{max}$. The chordwise spacing of the downstream streaks displayed in Figure 4.13a differs from the chordwise width of the initial spanwise rolls, displayed in Figure 4.12b. Since terminal streaks at $z = z_{max}$ display significantly larger energy levels than initial spanwise vortices, the wavenumber selection of optimal disturbances should be based on the *downstream wavenumber at* z_{max}. The 'optimal chordwise wavenumber' γ therefore reads

$$\gamma = \frac{2\pi}{\Lambda} \,, \tag{4.58}$$

where Λ is the chordwise spacing, i.e. twice the mean width, of the spanwise streaks generated downstream of an optimal perturbation. Figure 4.13b shows that, as the optimal disturbance comprises a larger number of initial spanwise vortices (or equivalently, spanwise streaks), i.e. as the width L of the Gaussian energy weight increases, the optimal wavenumber γ indeed approaches the optimal wavenumber β for the Blasius boundary layer rescaled by d/δ.

At Reynolds numbers higher than $Re \sim 10^2$, swept Hiemenz flow behaves similarly to the two-dimensional Blasius boundary layer in the vicinity of the attachment-line. Optimal spatial disturbances consist of steady counter-rotating spanwise vortices that generate spanwise streaks via the lift-up mechanism. The chordwise width of the resulting streaks is selected to match the optimal transverse wavenumber found in the Blasius boundary layer, suitably scaled by d/δ, whereas the number of streaks depends on the width of the Gaussian energy weight function $\lambda_E(x)$.

Chapter 5

Conclusion : research on the attachment-line boundary layer in a historical perspective

The attachment-line boundary layer has been known to be linearly unstable to two-dimensional Görtler-Hämmerlin disturbances since Hall et al. (1984). Also, two-dimensional waves travelling in the spanwise direction have been observed experimentally by Pfenninger and Bacon (1969) on smooth leading edges. The attachment-line boundary layer is likely to sustain turbulence originating from the fuselage or when it is excited with a trip wire of sufficient thickness, as demonstrated by Poll (1978).

These long-known features of the attachment-line boundary layer are strikingly similar to what is observed in two-dimensional boundary layers. Squire's theorem states that the most unstable mode in two-dimensional shear flows is two-dimensional itself and, indeed, the developing Blasius boundary-layer is known to support exponentially growing, two-dimensional Tollmien-Schlichting travelling waves. Also, a two-dimensional cross-stream trip wire is efficient as a turbulence generator in two-dimensional boundary layers.

Following the experiments of Poll (1978), it could have been tempting to continue the analogy between attachment-line boundary layers and two-dimensional shear flows. However, the three-dimensional nature of the flow at the leading edge could neither be ignored in experiments nor in linear stability investigations. Experiments focused on contamination of the upper surface by attachment-line disturbances, which is a three-dimensional phenomenon. Linear stability studies demonstrated that the most unstable perturbations are two-dimensional in the chordwise $x-$direction; for sufficiently large x, the chordwise base velocity $xU(y)$ is at least as

large as the spanwise sweep W and three-dimensional effects have to be taken into account.

Over the last fifteen years, advances in the field of shear flow stability came in large measure from the investigation of transient phenomena. In the same spirit, the present study has focused on short-term (temporal) or localized (spatial) energy amplification in the attachment-line boundary layer. In this context, it has been shown in the present work that three-dimensional effects do not play a major role in the vicinity of the attachment-line.

In the framework of the Görtler-Hämmerlin hypothesis, which assumes that perturbations are two-dimensional in the spanwise-wall-normal $(z, y)-$plane, optimal temporal disturbances are transiently amplified by a mechanism that resembles the classical two-dimensional Orr mechanism: two-dimensional *chordwise* vortices are compressed and amplified in the spanwise shear W'.

When the Görtler-Hämmerlin assumption is relaxed, optimal temporal disturbances take the shape of *spanwise* counter-rotating vortices. In the temporal framework, lift-up in the spanwise direction is the optimal energy amplification mechanism.

Spatial optimal disturbances take the shape of steady spanwise vortices. As optimal temporal perturbations, optimal spatial perturbations are amplified by lift-up in the spanwise direction.

Perturbations localized near the attachment line ($x = 0$) are indeed subject to very low strain in the chordwise $x-$direction, since the chordwise base velocity $xU(y)$ is proportional to the distance from the attachment line. Temporal transient energy growth, as investigated in chapter 3, has been shown to reach a maximum on rather short characteristic time scales (in scaled units, $\tau \sim 100$). On such short times perturbations have not moved significantly far away from the attachment-line. Similarly, spatial energy amplification is maximum at moderate downstream distances ($z_{max} \sim 200$). No significant spreading in the chordwise direction takes place before optimal spatial perturbations reach z_{max}.

As a consequence, maximum transient temporal or spatial energy amplification takes place within a region close to the attachment-line, where chordwise stretching is still negligible. The agreement between the present results on optimal energy amplification in swept Hiemenz flow and previously published results pertaining to the two-dimensional Blasius boundary layer is therefore not surprising.

Optimal disturbances have previously been computed in the two-dimensional developing Blasius boundary layer (Andersson et al. (1999)) and the three-dimensional Falkner-Skan-Cooke configuration (Corbett and Bottaro (2001a)). The present the-

sis completes the picture of transient growth phenomena inside the boundary layer that surrounds a swept wing.

In my opinion, a complete understanding of flow stability around swept wings would require, on the one hand, that a connection be made between the attachment-line boundary layer considered in the present thesis and previously published findings on energy amplification in the three-dimensional swept boundary-layer; on the other hand, receptivity of the entire leading-edge – attachment-line plus downstream boundary-layer – to external disturbances should be investigated in light of the physichal mechanisms unveiled in the present study. With a lot of work and a little luck, an answer may be found to the intriguing question: how may the two attachment-line scenarios – chordwise vortices travelling in the spanwise direction or spatially developing, counter-rotating vortices parallel to the leading edge – be connected with stationary, co-rotating crossflow vortices observed on the upper surface of swept wings ?

Appendix

A.1 Enforcing non-trivial boundary conditions with the fringe region technique

One may consider investigating spatially developing disturbances with the spectral DNS code described in chapter 3, although spatially developing disturbances are intrinsically not periodic in the streamwise direction. Perturbations can be made periodic with a damping fringe region at z_{max}. Berlin et al. (1999) further suggested the use of the fringe technique to force outgoing disturbances to non-trivial perturbations at $z = 0$ instead of forcing them to zero. In this case equations (3.21a,b) are replaced by

$$\partial_t \phi = h_\phi + \frac{1}{Re}\nabla^2\phi - \lambda_x(x)\phi - \lambda_z(z)(\phi - \phi_0) \ , \tag{A.1a}$$

$$\partial_t \omega = h_\omega + \frac{1}{Re}\nabla^2\omega - \lambda_x(x)\omega - \lambda_z(z)(\omega - \omega_0) \ , \tag{A.1b}$$

where the damping parameter λ_z iz taken to be

$$\lambda_z(z) = \lambda_{z\ max}\left(1 - S\left(\frac{z + z_{max}}{d_z}\right) + S\left(\frac{z - z_{max}}{d_z}\right)\right) \ , \tag{A.2}$$

with $\lambda_{z\ max}$ as the amplitude of the damping and d_z as the width of the fringe.

Starting from the trivial solution $\phi(x, y, z, t = 0) = 0$, $\omega(x, y, z, t = 0) = 0$, equations (A.1a,b) are marched forward in time. Disturbances propagate from the forcing location $z = 0$ to the damping region located beyond $z = z_{max}$ until a steady state is reached; the temporal computation is then stopped.

Berlin et al. (1999) compared five different techniques designed to generate oblique waves in a two-dimensional boundary layer. Three different types of blowing and suction at the wall, an artificial body force and the fringe region forcing technique have been tested. The simulations compare well with experimental results in all five cases, as measured by the downstream development of u_{rms}, streak amplitude, etc.. All five methods, including the fringe region technique, seem to be reliable. However, it may be argued that oblique-wave-induced transition simulations are not very sensitive to the 'quality' of initial conditions; even if the least-damped Orr-Sommerfeld mode forced via the fringe region technique is poorly rendered at the inflow location, the flow will quickly approach this dominant eigenmode.

Nordström et al. (1999) investigated in detail the efficiency of the fringe region technique by computing the velocity profile of a spatially evolving boundary layer. They present a theoretical analysis of the error the fringe region induces, and they provide numerical results from several pseudo-spectral simulations. The approximated boundary-layer profile u_{BL} computed via the boundary-layer equations is forced in a fairly wide fringe region. The induced velocity profile v is compared to the target u_{BL} throughout both the fringe region and the physical domain. The developing profile u_{BL} is made periodic in the streamwise $x-$direction by smoothly reconnecting $u_{BL}(x = 0)$ with $u_{BL}(x = x_{max})$ over a fraction of the fringe region. The agreement is indeed excellent, and the computed velocity v coincides with the Blasius solution u_{BL} to five significant digits. We will show in the following that this result is not surprising since the Blasius profile itself is a very accurate approximation of the true, physical velocity profile.

Let us analyze the fringe region technique in more detail. Berlin et al. (1999) generated disturbances ϕ_0, ω_0 in the shape of the least stable Orr-Sommerfeld mode by introducing a fringe region with a weight function $\lambda_z(z)$ according to

$$\partial_t \phi = h_\phi + \frac{1}{Re}\nabla^2\phi - \lambda_z(z)(\phi - \phi_0) \ , \tag{A.3a}$$

$$\partial_t \omega = h_\omega + \frac{1}{Re}\nabla^2\omega - \lambda_z(z)(\omega - \omega_0) \ , \tag{A.3b}$$

$$\nabla^2 v = \phi \ . \tag{A.3c}$$

Equations (A.3a,b,c) are marched in time starting from the trivial initial condition $(\phi, \omega) = (0, 0)$. The spatially developing perturbation with upstream condition $(\phi(z = 0), \omega(z = 0)) = (\phi_0, \omega_0)$ is found when a steady state has been reached. Then, the left-hand side of equations (A.3a,b) is zero and (ϕ, ω) satisfy

$$\lambda_z(z)(\phi - \phi_0) = h_\phi + \frac{1}{Re}\nabla^2\phi \ , \tag{A.4a}$$

$$\lambda_z(z)(\omega - \omega_0) = h_\omega + \frac{1}{Re}\nabla^2\omega \ . \tag{A.4b}$$

If (ϕ_0, ω_0) is a solution, or at least a good approximation, of a solution to the steady Navier Stokes equations, equations (A.4) may be reformulated as

$$\lambda_z(z)(\phi-\phi_0) = \left(h_\phi+\frac{1}{Re}\nabla^2\phi\right)-\left(h_{\phi_0}+\frac{1}{Re}\nabla^2\phi_0\right)\ , \qquad \text{(A.5a)}$$

$$\lambda_z(z)(\omega-\omega_0) = \left(h_\omega+\frac{1}{Re}\nabla^2\omega\right)-\left(h_{\omega_0}+\frac{1}{Re}\nabla^2\omega_0\right)\ . \qquad \text{(A.5b)}$$

In this case $(\phi,\omega)=(\phi_0,\omega_0)$ is a solution of equations (A.5), and a steady state may indeed be reached where (ϕ,ω) is equal to the target (ϕ_0,ω_0) at the exit of the fringe region. In particular, if (ϕ_0,ω_0) is the least stable spatial Orr-Sommerfeld mode as in Berlin et al. (1999) then (ϕ,ω) converge smoothly toward (ϕ_0,ω_0) throughout the fringe region due to the action of both the forcing and the natural selection of the least stable eigenmode.

In the case where (ϕ_0,ω_0) is not a solution to the Navier-Stokes equations, the steady disturbance (ϕ,ω) is necessarily distinct from the target (ϕ_0,ω_0) wherever λ_z is not equal to zero. Where (ϕ,ω) is equal to (ϕ_0,ω_0), the right-hand side of equations (A.4a,b) is zero, which contradicts the fact that (ϕ_0,ω_0) is not a solution to the steady Navier-Stokes equations. As a consequence, when the target forcing is not a solution to the Navier-Stokes equations the resulting steady disturbance differs from the target (ϕ_0,ω_0).

A way to ensure that the steady state will be fairly close to the target is to increase the damping weight λ_z. The stronger the damping, the closer the steady-state perturbation will be to the target. Still, equality is difficult to achieve in practice since stronger damping requires smaller numerical time steps and the amplitude of λ_z is increased at the expense of computational speed.

During the optimization process, one has to enforce a variety of initial conditions (ϕ_0, ω_0) at $z=0$. The corresponding steady flow is unknown in the region located upstream of $z=0$. Unless an independent DNS is run upstream of $z=0$, one cannot prescribe a target (ϕ_0,ω_0) that will be a solution of the Navier-Stokes equations throughout the fringe. The fringe region technique is not efficient in practice to enforce a given, arbitrary, initial condition stemming from the optimization process. Adapting the temporal DNS code described in chapter 3 to the spatial problem is more demanding than simply adding a fringe region in the spanwise $z-$direction. The spatial problem may instead be addressed with the parabolized approach described in chapter 4.

Bibliography

Abergel, F. and Témam, R. 1990 On some control problems in fluid mechanics. *Theor. Comp. Fluid Dyn.* **1**, 303–325

Andersson, P., Berggren, M., and Henningson, D. S. 1999 Optimal disturbances and bypass transition in boundary layers. *Phys. Fluids* **11**, 134–150

Arnal, D., Coustols, E., and Juillen, J. C. 1984 Etude expérimentale et théorique de la transition sur une aile en flèche infinie. *La Recherche Aérospatiale* **4**, 275–290

Berlin, S., Wiegel, M., and Henningson, D. S. 1999 Numerical and experimental investigations of oblique boundary layer transition. *J. Fluid Mech.* **393**, 23–57

Bertolotti, F. P. 1999 On the connection between cross-flow vortices and attachment-line instabilities. *Proceedings of the IUTAM Symposium on Laminar-Turbulent Transition*

Bewley, T. R. 2001 Flow control: new challenges for a new Renaissance. *Prog. Aerospace Sci.* **37**, 21–58

Bewley, T. R. and Liu, S. 1998 Optimal and robust control and estimation of linear paths to transition. *J. Fluid Mech.* **365**, 305–349

Bewley, T. R., Moin, P., and Temam, R. 2001 DNS-based predicitive control of turbulence: an optimal benchmark for feedback algorithms. *J. Fluid Mech.* **447**, 179–225

Blasius, H. 1908 Grenzschichten in Flussigkeiten mit kleiner Reibung.. *Z. Math. Phys.* **56**, 1–37

Brattkus, K. and Davis, S. H. 1991 The linear stability of plane stagnation-point flow against general disturbances. *Q. J. Mech. Appl. Math.* **44**, 135–146

Butler, K. M. and Farrell, B. F. 1992 Three-dimensional optimal perturbations in viscous shear flow. *Phys. Fluids A* **4**, 1637–1650

Cathalifaud, P. and Luchini, P. 2000 Algebraic growth in boundary layers: optimal control by blowing and suction at the wall. *Eur. J. Mech. B - Fluids* **19**, 469–490

Corbett, P. and Bottaro, A. 2001a Optimal control of nonmodal disturbances in boundary layers. *Theor. Comp. Fluid Dyn.* **15**, 65–81

Corbett, P. and Bottaro, A. 2001b Optimal linear growth in swept boundary layers.

J. Fluid Mech. **435**, 1–23

Cossu, C., Chomaz, J.-M., Huerre, P., and Costa, M. 2000 Maximum spatial growth of Görtler vortices. *Flow, turbulence and combustion* **65**, 369-392

Cumpsty, N. A. and Head, M. R. 1969 The calculation of the three-dimensional turbulent boundary layer. Part III: Comparison of attachment-line calculations with experiment. *Aero. Q.* **20**, 99–113

Dhanak, M. R. and Stuart, J. T. 1995 Distortion of the stagnation-point flow due to cross-stream vorticity in the external flow. *Phil. Trans. R. Soc. Lond. A* **352**, 443–452

Fransson, J. H. M., Talamelli, A., Brandt, L., and Cossu, C. 2006 Delaying transition to turbulence by a passive mechanism. *Phys. Rev. Lett.* **96**, 064501

Gad-el Hak, M. 2000 *Flow Control: Passive, Active, and Reactive Flow Management* Cambridge University Press, London

Gaster, M. 1965 A simple device for preventing turbulent contamination on swept leading edges. *J. Royal Aero. Soc.* **69**, 788–89

Gaster, M. 1967 On the flow along swept leading edges. *Aero. Q.* **18**, 165–184

Görtler, H. 1955 Dreidimensionale Instabilität der ebenen Staupunktsströmung gegenüber wirbelartigen Störungen. In *50 Jahre Grenzschichtforschung. eds. H. Görtler and W. Tollmien* Vieweg, Braunschweig

Gray, W. E. 1952a The effect of wing sweep on laminar flow. *Roy. Aircraft Est. TM 255* ARC 14,929

Gray, W. E. 1952b The nature of the boundary-layer flow at the nose of a swept wing. *Roy. Aircraft Est. TM 256* ARC 15,021

Greenbaum, A. 1997 *Iterative Methods for Solving Linear Systems* SIAM, Philadelphia

Guégan, A., Huerre, P., and Schmid, P. J. 2007 Optimal disturbances in swept Hiemenz flow. *J. Fluid Mech.* **578**, 223–232

Guégan, A., Schmid, P. J., and Huerre, P. 2006 Optimal energy growth and optimal control in swept Hiemenz flow. *J. Fluid Mech.* **566**, 11–45

Gunzburger, M. D. 1997 *Inverse design and optimization methods* von-Karman Institute for Fluid Dynamics Lecture Series

Gustavsson, L. H. 1991 Energy growth of three-dimensional disturbances in plane Poiseuille flow. *J. Fluid Mech.* **224**, 241–260

Hall, P. and Malik, M. R. 1986 On the instability of a three-dimensional attachment-line boundary layer: weakly nonlinear theory and a numerical approach. *J. Fluid Mech.* **163**, 257–282

Hall, P., Malik, M. R., and Poll, D. I. A. 1984 On the stability of an infinite swept attachment line boundary layer. *Proc. Roy. Soc. Lond. A* **395**, 229–245

Hämmerlin, G. 1955 Zur Instabilitätstheorie der ebenen Staupunktsströmung. In *50 Jahre Grenzschichtforschung. eds. H. Görtler and W. Tollmien* Vieweg, Braunschweig

Haynes, P. H. 1987 On the instability of sheared disturbances. *J. Fluid Mech.* **175**, 463–478

Hiemenz, K. 1911 Die Grenzschicht an einem in den gleichförmigen Flüssigkeitsstrom eingetauchten geraden Kreiszylinder *Ph.D. thesis*. Göttingen

Hoepffner, J., Brandt, L., and Henningson, D. S. 2005 Transient growth on boundary layer streaks. *J. Fluid Mech.* **537**, 91–100

Högberg, M., Bewley, T. R., and Henningson, D. S. 2003 Linear feedback control and estimation of transition in plane channel flow. *J. Fluid Mech.* **481**, 149–175

Högberg, M. and Henningson, D. S. 2002 Linear optimal control applied to instabilities in spatially developing boundary layers. *J. Fluid Mech.* **470**, 151–179

Huerre, P. 2000 Open shear flow instabilities. In *Perspectives in fluid dynamics (ed. Batchelor, G. K., Moffatt, H. K. and Worster, M. G.)* Cambridge University Press

Hunt, J. C. R., Wray, A. A., and Moin, P. 1988 Eddies, streams, and convergence zones in turbulent flows. In *Studying Turbulence Using Numerical Simulation Databases, 2.* Proceedings of the 1988 Summer Program

Joshi, S. S., Speyer, J. L., and Kim, J. 1997 A systems theory approach to the feedback stabilization of infinitesimal and finite-amplitude disturbances in plane Poiseuille flow. *J. Fluid Mech.* **332**, 157–184

Joslin, R. D. 1995 Direct simulation of evolution and control of three-dimensional instabilities in attachment-line boundary layers. *J. Fluid Mech.* **291**, 369–392

Joslin, R. D. 1998 Aircraft laminar flow control. *Annu. Rev. Fluid Mech.* **30**, 1–29

Joslin, R. D., Gunzburger, M. D., Nicolaides, R. A., Erlebacher, G., and Hussaini, M. Y. 1997 Self-contained automated mehodology for optimal flow control. *AIAA J.* **35**, 816–824

Koch, W., Bertolotti, F., Stolte, A., and Hein, S. 2000 Nonlinear equilibrium solutions in a three-dimensional boundary layer and their secondary instability. *J. Fluid Mech.* **406**, 131–174

Landahl, M. 1980 A note on an algebraic instability of inviscid parallel shear flows. *J. Fluid Mech.* **98**, 243–251

Lesshafft, L. 2006 Nonlinear global modes and sound generation in hot jets *Ph.D. thesis*. Ecole Polytechnique

Lin, R.-S. and Malik, M. R. 1996 On the stability of attachment-line boundary layers. Part 1. The incompressible swept Hiemenz flow. *J. Fluid Mech.* **311**, 239–255

Luchini, P. 2000 Reynolds-number-independent instability of the boundary layer over a flat surface: optimal perturbations. *J. Fluid Mech.* **404**, 289–309

Lumley, J. and Blossey, P. 1998 Control of turbulence. *Annu. Rev. Fluid Mech.* **30**, 311–327

Lundbladh, A., Henningson, D. S., and Johansson, A. V. 1992 An efficient spectral integration method for the solution of the Navier-Stokes equations. *NASA*

STI/Recon Technical Report N **93**, 29009-+

Lyell, M. J. and Huerre, P. 1985 Linear and nonlinear stability of plane stagnation flow. *J. Fluid Mech.* **161**, 295–312

Nordström, J., Nordin, N., and Henningson, D. 1999 The fringe region technique and the Fourier method used in the direct numerical simulation of spatially evolving viscous flows. *SIAM* **20**, 1365–1393

Obrist, D. 2000 On the stability of the swept leading-edge boundary layer *Ph.D. thesis*. U. Washington, Seattle

Obrist, D. and Schmid, P. 2003a On the linear stability of swept attachment-line boundary layer flow. Part I: Spectrum and asymptotic behavior. *J. Fluid Mech.* **493**, 1–29

Obrist, D. and Schmid, P. 2003b On the linear stability of swept attachment-line boundary layer flow. Part II: Nonmodal effects and receptivity. *J. Fluid Mech.* **493**, 31–58

Orr, W. 1907 The stability or instability of the steady motions of a liquid. *Proc. R. Irish Acad. A* **27**, 9–69

Pfenninger, W. 1977 Laminar flow control - Laminarization. Special Course on Concepts for Drag Reduction. *AGARD* 654

Pfenninger, W. and Bacon, J. W. 1969 Amplified laminar boundary layer oscillations and transition at the front attachment line of a 45 deg swept flat-nosed wing with and without suction. In *Viscous drag reduction (ed. C. S. Wells)* Plenum Press

Poll, D. I. A. 1978 Some aspects of the flow near a swept attachment line with particular reference to boundary layer transition. *C. of A. Report 7805*

Poll, D. I. A. 1979 Transition in the infinite swept attachment line boundary layer. *Aero. Q.* **30**, 607–629

Pralits, J. O., Hanifi, A., and Henningson, D. S. 2002 Adjoint-based optimization of steady suction for disturbance control in incompressible flows. *J. Fluid Mech.* **467**, 129–161

Press, W. H., Teukolsky, S. A., Vetterling, W. T., and Flannery, B. P. 1992 *Numerical Recipes in Fortran* Cambridge University Press

Reneaux, J. 2004 Overview on drag reduction technologies for civil transport aircraft. *ECCOMAS*

Robitaillié-Montané, C. 2005 Une approche non locale pour l'étude des instabilités linéaires. Application à l'écoulement de couche limite compressible le long d'une ligne de partage. *Ph.D. thesis*. Supaero

Schmid, P. J. and Henningson, D. S. 2001 *Stability and Transition in Shear Flows* Springer, New York

Spalart, P. and Yang, K. 1987 Numerical study of ribbon-induced transition in Blasius flow. *J. Fluid Mech.* **178**, 345–365

Spalart, P. R. 1988 Direct numerical study of leading-edge contamination. *Pro-*

ceedings of the AGARD Symposium on Application of Direct and Large-Eddy Simulation to Transition and Turbulence

Theofilis, V. 1998 On linear and nonlinear instability of the incompressible swept attachment-line boundary layer. *J. Fluid Mech.* **355**, 193–227

Theofilis, V., Fedorov, A., Obrist, D., and Dallmann, U. C. 2003 The extended Görtler-Hämmerlin model for linear instability of three-dimensional incompressible swept attachment-line boundary layer flow. *J. Fluid Mech.* **487**, 271–313

Trefethen, L. N., Trefethen, A. E., Reddy, S. C., and Driscoll, T. A. 1993 Hydrodynamic stability without eigenvalues. *Science* **261**, 578–584

Tumin, A. and Reshotko, E. 2001 Spatial theory of optimal disturbances in boundary layers. *Phys. Fluids* **13**, 2097–2104

Vanneste, J. 1999 A spatial analogue of transient growth in plane Couette flow. *J. Fluid Mech.* **397**, 317–330

Walther, S., Airiau, C., and Bottaro, A. 2001 Optimal control of Tollmien-Schlichting waves in a developing boundary layer. *Phys. Fluids* **13**, 2087–2096

Williamson, J. H. 1980 Low-storage Runge-Kutta schemes. *J. Comp. Phys.* **35**, 48–56

Wilson, S. D. R. and Gladwell, I. 1978 The stability of a two-dimensional stagnation flow to three-dimensional disturbances. *J. Fluid Mech.* **84**, 517–527

Abstract

The flow at the leading edge of a swept wing is accurately modelled by swept Hiemenz flow. At large enough sweep angles swept Hiemenz flow is linearly unstable to Görtler-Hämmerlin (GH) disturbances, which are essentially two-dimensional. Obrist and Schmid (2003) have shown that even at moderate sweep angles at which the flow is linearly stable, GH disturbances may be considerably amplified on short time scales. The goal of the present thesis is to quantify transient growth phenomena in swept Hiemenz flow and study the underlying physical mechanisms. GH perturbations are used as a model problem to set up and validate a very general gradient-based optimization algorithm. Temporal amplification of up to three orders of magnitude has been observed in GH disturbances, which is due to an analogue of the well-known two-dimensional Orr mechanism in two-dimensional shear flows. The optimal amplification of temporal disturbances has been observed for counter-rotating spanwise vortices that do not satisfy the GH assumption; the amplification mechanism could be linked with the classical lift-up mechanism. Transient spatial energy growth in the spanwise direction has also been investigated. The results in terms of optimal spatial disturbances, spatial energy amplification and the underlying mechanism have been successfully linked with lift-up induced spatial growth in two-dimensional Blasius boundary layers.

Keywords : optimal perturbations, transient growth, attachment-line, adjoint techniques, optimal control

Résumé

L'écoulement de Hiemenz balayé latéralement est un modèle fidèle de l'écoulement sur le bord d'attaque d'une aile en flèche. Pour des angles de flèche importants l'écoulement de Hiemenz balayé latéralement est instable pour des perturbations de Görtler-Hämmerlin (GH), qui sont de nature essentiellement bi-dimensionnelle. Obrist et Schmid (2003) ont montré que, même à des angles de flèche modérés auxquels l'écoulement est linéairement stable, des perturbations GH peuvent être amplifiées considérablement sur un intervalle de temps court. Le but de cette thèse est de quantifier les phénomènes de croissance transitoire dans l'écoulement de Hiemenz balayé et d'étudier les mécanismes physiques sous-jacents. Le modèle de perturbations GH est utilisé pour la mise au point et la validation d'un algorithme d'optimisation de type 'gradient'. Des amplifications temporelles de trois ordres de grandeur ont été observées pour des perturbations GH, dont l'origine physique est un analogue du mécanisme bidimensionnel d'Orr, connu pour les écoulements cisaillés bidimensionnels. L'amplification optimale de perturbations temporelles a été observée pour des tourbillons contra-rotatifs parallèles à la ligne d'arrêt, qui ne satisfont pas l'hypothèse de Görtler-Hämmerlin; le mécanisme d'amplification est alors semblable au mécanisme classique de 'lift-up'. La croissance transitoire spatiale le long du bord d'attaque a aussi fait l'objet d'une étude. Il a été montré que les perturbations spatiales optimales, leur taux d'amplification et le mécanisme physique responsable sont étroitement liés aux phénomènes de croissance transitoire induits par le mécanisme de lift-up dans une couche limite bidimensionnelle de Blasius.

Mots-clef : perturbations optimales, croissance transitoire, ligne d'arrêt, méthodes adjointes, contrôle optimal